Piezotronics as an Electromechanical Interfacing Technology for Electronic and Optoelectronic Applications

A Dissertation Presented to the Academic Faculty

By

Xiaonan Wen

Thesis Advisor: Prof. Zhong Lin Wang

School of Materials Science and Engineering

Georgia Institute of Technology

August 2015

Piezotronics as an Electromechanical Interfacing Technology for Electronic and Optoelectronic Applications

Approved by:

Dr. Zhong Lin Wang, Advisor
School of Materials Science and Engineering
Georgia Institute of Technology

Dr. Meilin Liu
School of Materials Science and Engineering
Georgia Institute of Technology

Dr. Gleb Yushin
School of Materials Science and Engineering
Georgia Institute of Technology

Dr. Zhiqun Lin
School of Materials Science and Engineering
Georgia Institute of Technology

Dr. Peter Hesketh
Woodruff School of Mechanical Engineering
Georgia Institute of Technology

Date approved: April 2nd, 2015

Acknowledgement

First and foremost, I would like to express my highest thanks and gratitude to my advisor, Prof. Zhong Lin Wang. Long before joining his group, I was already amazed and deeply attracted by the innovative works done by his group. As an undergraduate student back then, one did not get too many chances to attend presentations delivered by a world famous scientist but I was lucky enough to be one of the excited audience during Prof. Wang’s fascinating presentations. The wish to work under his guidance could not be stronger and the moment I was admitted into his group at Georgia Tech, I told myself, “life has changed”. Prof. Wang has been providing incredible guidance, encouragement and help throughout all these years during my PhD study. From being a new college graduate who barely knew anything about research, I am confident to say that I have become a researcher that can make meaningful contributions to science and technology. Prof. Wang is really special. He never appoints the students to work on specific projects but is always open to any new ideas from us and provides the strongest support for us to test and try. His level of dedication to science and research is so incredible that everyone working with him is deeply inspired and motivated. Most importantly, the field of research he has led me into is extremely fascinating as well as significant and I always work and enjoy at the same time, never feeling tired or lost. Last but not least, not only did he guide me into the wonderful world of scientific research, he also never spares his care and support for my personal life. This kind of

help is especially invaluable for an international student like me and my appreciation is beyond words.

I would also like to express my sincere thanks to my dissertation committee members, Prof. Meilin Liu, Prof. Gleb Yushin, Prof. Zhiqun Lin and Prof. Peter Hesketh for your valuable time and precious advice which is really helpful to improve the quality of my dissertation and presentation. Also sincere thanks to the wonderful lectures you and many other professors in Georgia Tech have delivered and I am lucky to have learnt so much from so many wonderful teachers and scientists.

Special thanks to Dr. Wenzhuo Wu and Dr. Sheng Xu who were my direct mentors during the early years of my PhD study. Without their help, guidance, support and especially the generous sharing of their priceless knowledge, experience and skills, I will never be able to quickly and smoothly adapt to the new work and life style in graduate schools and make timely progress in my research. Collaboration plays a key role in my research projects and I would like to sincerely thank all my collaborators, inclucing Dr. Wenzhuo Wu, Dr. Sheng Xu, Dr. Weiqing Yang, Dr, Yuanjie Su, Dr. Zhaona Wang, Ruomeng Yu, Long Lin, Jun Chen, Ken Pradel, Dr. Yong Ding, Tiejun Zhang, Simiao Niu, Dr. Sihong Wang, Dr. Youfan Hu, Dr. Ya Yang, Dr. Guang Zhu, Dr. Yusheng Zhou, Dr. Zheng Li and many others, for the wonderful collaboration, discussion and help.

Lastly, I would like to thank all my friends and family, especially my dear dad and mom. You have worked so hard to raise me and has provided me a very comfortable environment and anything I ever wanted. Most importantly, you unconditionally support each and every one of my idea and decision, never with questions but full of care and positive advice. It is the incredible openness and freedom I have enjoyed all the way to adulthood that makes me the person I am. Thank you mom and dad!

Table of Contents

Chapters:

List of Figures:

List of abbreviations:

NW	nanowire
FET	field effect transistor
M-S	metal-semiconductor
S-S	semiconductor-semiconductor
EQE	external quantum efficiency
LED	light emitting diode
HMTA	hexamethylenetetramine
SEM	scanning electron microscope
TEM	transmission electron microscope
XRD	x-ray diffraction
PVD	physical vapor deposition
MBE	molecular beam epitaxy
MOCVD	metalorganic chemical vapor deposition
RF	radio frequency
3D	three-dimensional
SGVPT	strain-gated vertical piezotronic transistor
ITO	indium tin oxide
SBH	Schottky barrier height
PET	polyethylene terephthalate
MEMS/NEMS	micro/nano electromechanical systems
PD	photodetector
UV	ultraviolet light
PDMS	polydimethylsiloxane
PVDF	polyvinylidene fluoride
P3HT	poly(3-hexylthiophene-2,5-diyl)
PZT	lead zirconate titanate

Summary:

Innovation on human-machine interfacing technologies is critical for the development of smart, multifunctional and efficient electronic/optoelectronic systems. The effect of piezotronics is a newly started field of study, which utilizes piezoelectric polarization that is mechanically induced inside a piezoelectric semiconductor to regulate electron transport across electronic contact interfaces. With the concept coined in 2006, many efforts have been contributed to studying the underlying physical mechanism of this effect as well as demonstrating various applications based on single nanowire piezotronic devices. This thesis selects ZnO as the material foundation and was started by firstly studying flexible, controllable and scalable synthesis methods for ZnO nanowires array and thin film. By replacing the use of random, individual nanowires with these materials, novel piezotronic and piezophototronic devices were designed, fabricated and tested to achieve the function of strain sensing, tactile imaging, piezo-enhanced photodetection and solar energy harvesting. The adoption of nanowires array and thin film materials over single nanowires leads to significant advantages in terms of scalable fabrication, industrial compatibility and broader functionality. By consistently going down this route, we believe that the field of piezotronics will eventually make revolutionary impact on MEMS, optoelectronics, multifunctional sensor networks, human-machine interfacing and so on.

1. Introduction

The advancement of electronic technology, represented by the invention of computers, has dramatically changed many aspects of our society and daily life. Over the past decades, the roadmap of development for scientists and engineers is to produce more and more powerful electronic systems by increasing the transistor integration density at the speed of the Moore's law. However, it has become clear that we are approaching fundamental limits of lithography and etching technologies and thus face difficulties of making ever smaller features to maintain the Moore's Law. On the other hand, with already abundant computing power in most cases, the bottle neck issue is how to efficiently transform the absolute computing power into smart and multifunctional tasking capabilities. To achieve this, an electronic system needs to be more interactive and integrated with the environment and humans by collecting information from the exterior environment through multiple channels and actively providing feedback to assist with complex problem solving [1-5]. To put it simply, we need innovation on the human-machine interfacing technologies for further advancement of electronic technologies beyond the roadmap of the Moore's Law.

Mechanical stimulation is the most common form of interaction that the environment and a person can engage with an electronic system. Therefore, innovating mechanisms and developing devices that interface mechanical signals with electronics is of vital importance. Three most widely studied and utilized pressure sensing methods are respectively based on the Ohm's law, the piezoresistive effect [6-8] and the piezoelectric effect [9-11]. The first one is universal for all conducting and semiconducting materials which says that the change of materials' geometric shape leads to the change of resistance. The second one is manifest only for semiconductors and its pressure sensing relies on the strain-modulated bandgap, which is reflected as the change of resistance due to the change of carrier concentrations. (The Ohm's law strain sensing effect can also be considered as a generalized piezoresistive effect.) Both methods work in a passive mode. By applying a bias voltage and constantly measuring the current, the resistance can be directly correlated with the application of pressure/strain, which is an advantage of these methods. However, the sensitivity is usually low as limited by the nature of the sensing mechanisms. The third one only exists for piezoelectric materials. These materials show electric polarization under applied strain. When subject to the change of pressure/strain, voltage signals can be generated and thus this method works in an active mode. There is no need to measure the current and the sensitivity is usually very high. However, the output signal is the derivative of the pressure/strain over and the reconstruction of the normal signal requires integration operation.

As we can see, the existing mainstream technologies mentioned above either have low sensitivity or require signal integration. Although engineering solutions can be made to improve these methods, in order to fundamentally solve the problem, a new mechanism that combines simple device structure, simple detection circuit and high sensing performance is highly desired. Driven by this motivation, the piezotronic effect, as an innovative electromechanical interfacing mechanism, is the subject of study for my PhD thesis.

The piezotronic effect is a coupling effect of piezoelectricity and electronics [12-14]. The basic idea is to introduce piezoelectric polarization charges at a metal-semiconductor or a semiconductor-semiconductor interface so that the electron transport across the interface can be modulated by strain. This working mechanism raises two requirements for the functioning material: being piezoelectric and being semiconducting. As such, insulating piezoelectric materials like PZT, PVDF and Quartz are not suitable. Instead, Ⅱ-Ⅵ and Ⅲ-Ⅴ semiconductors such as ZnO, GaN and CdS, which usually have much smaller effective piezoelectric coefficients due to charge screening, become excellent materials for this application. Discovered in 2006 and originally studied for strain sensing [15-17], significant progress has been made on piezotronics, both for deepening the research on strain sensing as well as for extending its applications to many relevant applications. In my PhD research, I mainly focused on developing piezotronics based on ZnO NWs and thin films for strain sensing, tactile imaging and also optoelectronic applications.

This thesis consists of six chapters. Following the introduction, the second chapter will be dedicated to explaining the fundamental physics of the piezotronic effect on both the metal-semiconductor contact interface and the semiconductor-semiconductor contact interface. The third chapter talks about the synthesis of ZnO materials, which serve as the building blocks for all piezotronic devices studied in this thesis. Based on the knowledge and methods of how to synthesis ZnO NWs array and thin films in well-controlled manners, Chapter 4 then focuses on the implementation of the piezotronic effect based on these materials for force/pressure/strain sensing applications. The following chapter 5 studies how the piezotronic effect could be further applied for performance optimization of optoelectronic devices based on ZnO materials. At last, conclusions are drawn in chapter 6.

2. Fundamentals of Piezotronics

As stated in the introduction, the piezotronic effect is an electron transport regulation effect achieved by the introduction of piezoelectric polarization charges at a metal-semiconductor or semiconductor-semiconductor interface. By comparing to FETs, the piezopotential induced by mechanical triggering serves as a ‘gate voltage’ and a piezotronic device can be considered as a strain-gated transistor. In this chapter, fundamentals of piezotronics will be reviewed and discussed to provide a better understanding of the mechanisms [18-21].

2.1 Piezotronic effect on M-S contact interface

When a metal material and a semiconductor material come into contact, the Fermi level of the semiconductor will be aligned with that of the metal material, leading to redistribution of charges at the junction area. Depending on the types of materials, either Ohmic contact (non-rectifying junction) or Schottky contact (rectifying junction) may be formed. The piezotronic effect modulates the interfacial energy at the junction area. The modulation can be directly reflected by the effective resistance of the junction. Accordingly, the strength of this effect is positively related to the ratio of the junction resistance to the bulk resistance. In this regard, the existence of a Schottky barrier is the prerequisite for the piezotronic effect to take place at an M-S interface. By applying strain to the piezoelectric semiconductor, either positive or negative polarization charges are induced at the contact interface. Taking n-type semiconductor as an example, positive polarization charges attract free electrons and decrease the level of depletion, leading to reduced Schottky barrier height as well as its effective resistance; negative charges repel electrons and increase the level of depletion, leading to increased Schottky barrier height as well as its effective resistance. This process is schematically explained in Figure 1, which serves as the qualitative explanation of how the piezotronic effect modulates the electron transport across the M-S contact interface.

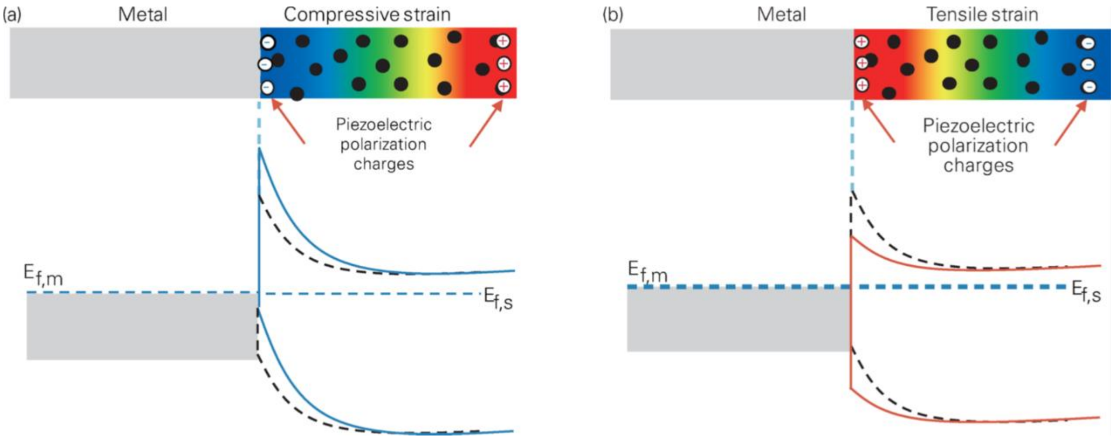

Figure 1: Schematic of the energy band diagram illustrating the piezotronic effect on M-S interface. (a) Negative polarization charges are induced at the interface, increasing the barrier height. (b) Positive polarization charges are induced at the interface, decreasing the barrier height. For the color gradient, red represents positive potential and blue represents negative potential. [22]

According to the diffusion theory, the current flowing through a Schottky barrier can be expressed as [23]:

$$J_n \approx J_D \cdot \left[\exp\left(\frac{qV}{\mathrm{kT}}\right) - 1\right],$$

where the saturation current density J_D can be expressed as:

$$J_D \approx q^2 D_n N_C \cdot (kT)^{-1} \cdot \sqrt{[2qN_D(\Psi_{bi} - V) \cdot \varepsilon_s^{-1}]} \cdot \exp\left[\frac{-\mathrm{q}\Phi_{Bn}}{kT}\right].$$

In this equation, D_n is the electron diffusion coefficient, N_C is the effective density of states in the conduction band, N_D is the donor concentration in the semiconductor, Ψ_{bi}

is the built-in potential, ε_s is the permittivity of the semiconductor and Φ_{Bn} is the Schottky barrier height. As explained earlier, the piezotronic effect is the tuning of the Schottky barrier height via piezoelectric charges. Thus this factor is further derived as:

$$\Phi_{\mathrm{Bn}} = \Phi_{\mathrm{Bn0}} - q^2 \rho_{piezo} W_{piezo}^2 (2\varepsilon_s)^{-1},$$

where ρ_{piezo} is the density of polarization charges and W_{piezo} represents the effective width of the polarization charge distribution. The correlation between the applied strain and the Schottky barrier height could then be established by:

$$P_z = e_{33} s_{33} = q \rho_{piezo} W_{piezo},$$

where e_{33} is the piezoelectric coefficient and s_{33} is the applied strain along the polar axis of the piezoelectric material. Ultimately, the relation between current density across the junction area and the applied strain is expressed as:

$$\mathrm{J}_n \approx J_{D0} \cdot \exp\,[q e_{33} s_{33} W_{piezo} \cdot (2\varepsilon_s kT)^{-1}] \cdot \exp\,[qV \cdot (kT)^{-1} - 1],$$

where J_{D0} is the saturation current density without introducing the piezoelectric polarization.

The above equation is the quantitative explanation of how the applied strain in a piezoelectric semiconductor could modulate the Schottky barrier height at the M-S interface and thus regulate the electron transport.

2.2 Piezotronic effect on S-S contact interface

When two pieces of semiconductor materials are brought into contact, their difference in Fermi levels will give rise to energy barriers at the contact interface. For the same reason, if polarization charges are introduced, the energy barrier height will be modulated accordingly. The piezotronic effect can take place at n-n junctions, p-p junctions as well as p-n junctions. Here we use the model of a homogeneous p-n junction as an example and only consider the piezoelectricity from the n-type material to explain the process.

The most important character of a p-n junction is a wide depletion region due to interdiffusion of holes and electrons. The strong built-in field not only enables significant optoelectronic applications such as LEDs and solar cells, but also greatly reduces the screening effect on the strength of the piezoelectric field due to the lack of free charge carriers within the space charge region [24, 25]. If positive piezoelectric polarization charges are induced at the interface by the n-type semiconductor, some electrons transporting across the junction will be attracted, leading to a downward bending of the band edge profiles at the junction area; if negative piezoelectric polarization charges are induced at the interface by the n-type semiconductor, electrons transporting across the junction will be repelled, leading to an upward bending of the band edge profiles at the junction area. This process is schematically explained in Figure 2.

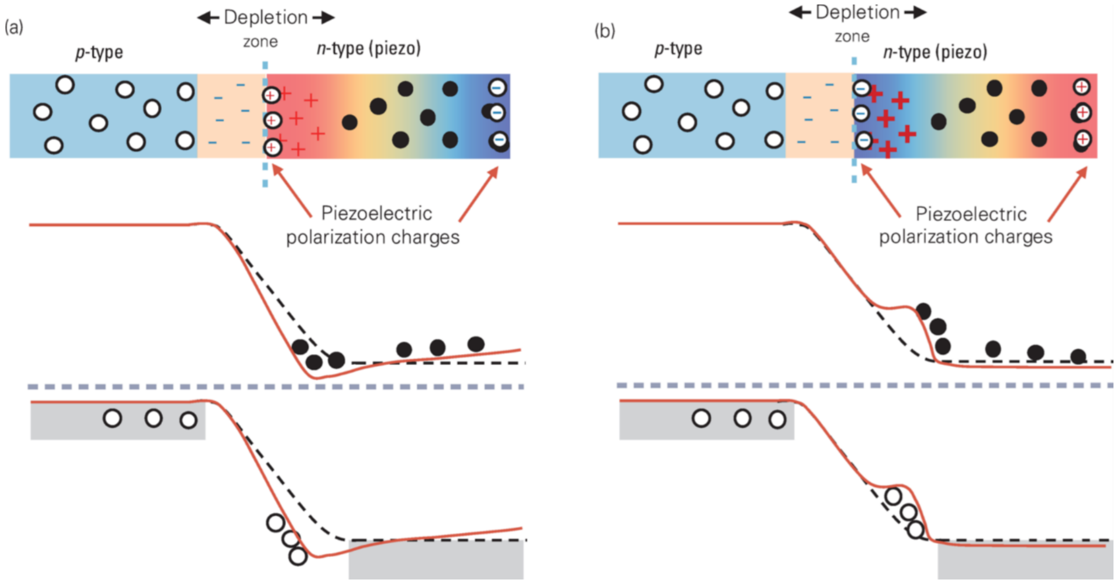

Figure 2: Schematic of the energy band diagram illustrating the piezotronic effect on p-n junction interface. (a) Positive polarization charges are induced at the interface, creating a dip in the band diagram. (b) Negative polarization charges are induced at the interface, creating a bump in the band diagram. For the color gradient, red represents positive potential and blue represents negative potential.[22]

By using the abrupt junction model, the built-in potential could be expressed in a simple form as below [26]:

$$\psi_{\mathrm{bi}} = q \cdot (2\varepsilon_s)^{-1} \cdot (N_A(x)W_{Dp}^2 + \rho_{piezo}W_{piezo}^2 + N_D(x)W_{Dn}^2) .$$

In this equation, $N_A(x)$ is the acceptor concentration, $N_D(x)$ is the donor concentration, ρ_{piezo} is the density of polarization charges, W_{Dp} and W_{Dn} are the widths of depletion layers for the p-type side and n-type side respectively and W_{piezo} is the equivalent distribution width of polarization charges. The built-in potential on one hand is directly related to the piezopotential generated by the piezoelectric semiconductor and on the other hand is the key parameter in optoelectronic applications. This clearly indicates how the piezotronic effect exerts its influence on optoelectronic processes.

Since M-S Schottky junction can be considered as a special p-n junction, we further assume that $p_{n0} \gg n_{p0}$, where p_{n0} is the thermal equilibrium hole concentration in the n-type semiconductor and n_{p0} is the thermal equilibrium electron concentration in the p-type semiconductor. Consequently we could apply the same expression that is used for the M-S contact:

$$\mathrm{J}_n \approx J_{C0} \cdot \exp\,[q e_{33} s_{33} W_{piezo} \cdot (2\varepsilon_s kT)^{-1}] \cdot \exp\,[qV \cdot (kT)^{-1} - 1] \;,$$

where J_{C0} represents the saturation current density without introducing the piezoelectric polarization.

Taking LED as an example [27],

$$P_{optic} = \beta\{J_{c0} \cdot \exp\,[q e_{33} s_{33} W_{piezo} \cdot (2\varepsilon_s kT)^{-1}] \cdot \exp\,[qV \cdot (kT)^{-1} - 1]\}^b \;,$$

where P_{optic} is the optical power output of the LED, β is a constant decided by materials and device structures and b is the power-law parameter. The external quantum efficiency (EQE) is $\eta_{ex} = \alpha\eta_{ex0}$, where η_{ex0} is the EQE without piezopotential. The term α represents the piezo effect which can be expressed as

$$\alpha = \{\exp\,[q^2 \rho_{piezo} W_{piezo}^2 (2\varepsilon_s kT)^{-1}]\}^{b-1} \;,$$

which reflects the modulation from the piezopotential on the carrier transport and the photo emission process.

The above analysis of the piezotronic effect on p-n junctions gives the qualitative and quantitative explanation of the modulation process and the logic could be extended to more complicated scenarios that involve heterogeneous junctions, p-type piezoelectric semiconductors, intrinsic regions etc.

3. ZnO material system for piezotronics

The basic requirement for the channel material of piezotronic transistors is being piezoelectric and semiconducting. Typical materials that meet this requirement are usually binary semiconductors belonging to the II-VI and III-V group, such as ZnO, CdS, GaN, CdSe etc. These materials each have their specific properties that suit the needs of different applications. Up to now, however, the majority of the efforts in the field of piezotronics have been focused on studying the ZnO material, mainly due to the simple and diverse synthesis approaches that is available to ZnO. Methods such as chemical vapor deposition [28-30], metalorganic vapor phase epitaxy [31, 32], electrophoretic deposition [33, 34], pulsed laser deposition [35, 36], sputtering [37, 38], sol-gel synthesis [39, 40] and hydrothermal synthesis [41-44] have all been used to synthesis various forms of ZnO materials under both low and high synthesis temperatures, producing both polycrystalline and monocrystalline materials ranging from thin films to nanowires and to nanoparticles. In this chapter, besides reviewing mainstream approaches, my own work on ZnO material synthesis will also be introduced and discussed.

3.1 ZnO NWs: physical vapor phase deposition

This method is conducted at a temperature high enough to vaporize the source material, in our case, the ZnO powders. Then the vapor is transported either by convection or by inert gase to a cooler location. Ruled by the law of crystallography, thermodynamics and kinetics, with suitable parameters of temperature gradient and environmental pressure, the material in the vapor phase will crystallize into the form of NWs. The vapor-liquid-solid growth process was proposed [45] to explain the one dimensional growth. According to the mechanism, catalyst metal such as gold is pre-deposited onto the substrate and the substrate is placed at a location with proper temperature. Once the vapor source arrives at the relatively cold substrate, liquid eutectic alloy will be formed by mixing the source with the catalyst. When the liquid alloy becomes supersaturated with the source material, the source will nucleate at the solid-liquid interface, resulting in 1-D nanowire growth. This, however, does not explain all vapor phase growth. Catalyst-free growth is also possible under certain conditions which may be explained by the vapor-solid process that skips the liquid phase [9].

Some early works reported successful growth of ZnO nanowires with physical vapor deposition method but the nanowires had random orientations, which greatly constrained its applications beyond single NW devices. Techniques for highly ordered ZnO nanowire arrays have been developed and advanced by Dr. ZL Wang, Dr. PD Yang and other researchers [46-48]. Substrates of small lattice mismatch with the c-plane of Wurtzite ZnO were used to ensure that all nanowires grow along the same direction. Patterned gold catalysts were made on top of the substrates to define the nucleation sites. Experimental parameters such as oxygen partial pressure and total pressure inside the synthesis chamber have also been investigated in detail to achieve the optimization of the growth process [30].

ZnO NWs grown by physical vapor deposition have high aspect ratios, usually with diameters less than 50 nm and lengths more than tens or hundreds of micrometers. A clean and dry environment ensures that the as-grown nanowires have few crystal defects, which grants them good mechanical robustness and much less screened piezoelectric effect. On the other hand, however, the high temperature needed for the growth, usually close to 1000 ^{o}C, severely limits the choice of substrates. Direct physical vapor growth on polymer substrates, known for their flexibility and transparency, is impossible.

3.2 ZnO NWs: hydrothermal deposition

This method utilizes chemical reaction in an aqueous solution. Consequently, the growth temperature is less than 100 ^{o}C in most cases. Precursors typically involve a type of zinc salts and a type of mild alkali that can constantly release OH^- over time [49]. Combinations of zinc nitrate hexahydrate and HMTA are proven to be very reliable precursors to produce relatively uniform and well controlled NWs [44, 50]. One of the greatest advantages of this method is that ZnO nanowires array could be obtained on almost any substrate by pre-depositing a ZnO seed layer as long as the substrates have moderate chemical resistance. In addition, the synthesis cost is significantly lower than that of the physical vapor deposition method and not constrained by the high temperature and fixed chamber size. Thus ZnO nanowires could be produced at a very large scale. These advantages greatly expand the potential applications of ZnO nanowires and meet the growing needs for flexible, transparent electronics, photonics, piezoelectricity and their overlapping fields.

However, despite these benefits, nanowires produced through wet chemical solution method usually have lower aspect ratio and more crystal defects. Hence, the quality of the nanowires may be a bottle neck for high requirement applications.

3.2.1 Seedless hydrothermal synthesis of patterned ZnO NW arrays on metal thin films [41]

For most of the hydrothermal approaches reported, a seed layer, normally a pre-deposited ZnO thin film, is indispensable to facilitate the nucleation and subsequent growth [51]. However, under certain circumstances, a seed layer may not be desirable due to the initial growth of a thin layer of ZnO film, in between the as-grown NWs and the substrate, which makes the roots of the NWs fuse together and hence renders indirect contact between the NWs and the substrate.

A novel hydrothermal approach for synthesizing aligned ZnO NW arrays preferentially on patterned surfaces of various commonly used metals without using a ZnO seed layer is developed here. Effects of experimental parameters such as the precursor concentration and the solution/container volume ratio in the chemical synthesis container have been studied. Electrical characterization was subsequently performed to reveal the characteristics of the contacts formed between the ZnO NWs and the metal layers.

In contrast to the commonly reported hydrothermal synthesis that utilizes a combination of zinc nitrate hexahydrate and HMTA and makes use of the slow hydrolyzation of HMTA to provide a weak base environment [52-54], here we use ammonium hydroxide instead, providing a relatively strong base environment. When ammonium hydroxide was firstly introduced into the solution, $Zn(OH)_2$ sediment was formed. By agitating the solution for a few seconds, it became clear again, indicating that the Zn^{2+} ions had combined with NH^{4+} ions to form stable zinc ammine [55]. HMTA hence provides a buffering mechanism for slowly releasing OH^-, while ammonium hydroxide enables a buffering mechanism of slowly releasing Zn^{2+}. Both methods can result in ZnO NW growth, while the method we present here results in unique properties as discussed later.

Some typical chemical reactions involved are listed below to describe the growth process[56]:

$$NH_3 \cdot H_2O \leftrightarrow NH^{4+} + OH^- \tag{1}$$

$$NH_3 \cdot H_2O \leftrightarrow NH_3 \uparrow + H_2O \tag{2}$$

$$Zn^{2+} + 2OH^- \leftrightarrow Zn(OH)_2 \downarrow \tag{3}$$

$$Zn(OH)_2 + 4\,NH_3 \cdot H_2O \leftrightarrow Zn(NH_3)_4{}^{2+} + 4H_2O + 2OH^- \tag{4}$$

$$Zn(OH)_2 \leftrightarrow ZnO + H_2O \tag{5}$$

All of these chemical reactions are in dynamic equilibrium and varying any one of them would affect the synthesis outcome. Factors affecting the reaction equilibrium include growth temperature, growth time, precursor concentration, the amount of ammonia gas dissolved in air in the container, etc. Here, the effects of manipulating reaction (4) and reaction (2) by tuning the concentration of ammonium hydroxide and the solution/container (s/c) volume ratio are investigated in detail.

A. Concentration of ammonium hydroxide

Ammonium hydroxide plays a two-fold role in the growth process. First, it provides OH^{-}, which is the source of O in ZnO; second, it provides NH^{4+}, which can form a complex with zinc ions as a buffering mechanism. In this section, the volume of the solution with 20 mM $Zn(NO_3)_2$ $6H_2O$ was fixed at 350 ml, contained in a 500 ml reaction container while different amounts of ammonium hydroxide (28 wt%) was added into the solution, ranging from 2 ml to 20 ml, with the ammonium hydroxide / $Zn(NO_3)_2$ $6H_2O$ nutrient solution volume ratio (named as the a/n volume ratio for convenience) ranging from 0.57% to 5.71%. In general, the length of the as-grown NWs is determined by the total amount of source material available (namely Zn^{2+} and OH^{-}), the growth time and the release rate of Zn^{2+}. The diameter of the NWs is determined by the total amount of source material and the release rate of Zn^{2+}. In particular, the equilibrium status of reaction (4) has a significant effect in shaping the NW tips. The density of the as-grown NWs is determined by various factors, such as the number of nucleation sites generated on the substrate during the initial stage of growth, the extent of NW fusing and the diameter of the base of NWs, and is thus related to the amount of OH^{-} available, Zn^{2+} released initially, the total amount of source material available, and the growth time.

Figure 3 (a) shows SEM images of NWs grown at a 0.57% a/n volume ratio. NH^{4+} and OH^{-} were both insufficient in this case, especially since there was not enough NH^{4+} to consume all of the $Zn(OH)_2$, leaving the solution in a turbid condition. Thus there was no buffering at the initial stage of growth and the existing $Zn(OH)_2$ would rapidly decompose into ZnO once heated, resulting in a film-like structure deposited on the substrate, with some of the nanorods fused together, while the rest were still separated, as can be seen from Figure 3 (a). The diameters and lengths of the as-grown nanorods were small in this case due to an insufficient supply of source materials. When the a/n volume ratio was increased, the Zn^{2+} was more and more slowly released while the concentration of OH^{-} was increased in the solution. Since Zn^{2+} and OH^{-} are both the source materials for synthesizing ZnO NWs and the increase in OH^{-} concentration is accompanied by the decrease of free Zn^{2+} concentration, we thus expect that with the increase of a/n ratio, the tip diameter, length and density of the NWs will increase to a maximum value first and decrease later. Figure 3 (b) and (c) show the results for NWs grown at 2.86% and 3.43% a/n volume ratios, respectively, which exhibit a good alignment and increase in tip diameter, length and density of NWs. By further increasing the a/n ratio, more source material would be available in the solution. However, not all of the three morphological parameters of the NW array increase. The length of the as-grown NWs increased due to faster vertical growth. The density of the NW array, however, decreased since small nuclei were likely to fuse with each other due to the faster deposition of ZnO occurring in the initial nucleation stage. As for the tip diameters of the NWs, the equilibrium of reaction (4) will shift to the right-hand side and the equilibrium of reaction (5) will shift to the left-hand side at a high a/n volume ratio. This means that there will be a higher etching rate of the formed ZnO crystal by ammonia. However, the etching is anisotropic because the absorption of NH_3 molecules is curvature dependent [57]. Regions of high curvature, such as the NW tips, attract more NH_3 molecules than the NW side walls and consequently such regions will be etched faster, resulting in needle-like NWs, as shown in Figure 3 (d). This phenomenon is named as the shaping effect in this section for convenience. Once the ammonium hydroxide concentration was increased to 5.71%, there was enough NH^{4+} in the solution that formed a complex with almost all of the Zn^{2+} ions and significantly depressed the growth process. As a result, no obvious growth of NWs can be observed, as shown in Figure 3 (e). Finally, a control experiment was performed for comparison, by using 350 ml solution of 20 mM $Zn(NO_3)^2 \cdot 6H_2O$ and 20 mM HMTA mixture, with the results shown in Figure 3 (f). A significant difference can be observed in that the NWs grown with the control recipe have larger dimensions, while the alignment among the NWs is poor. This could be explained by the difference in solution environment. In the control recipe, Zn^{2+} is in abundant existence while in the $Zn(NO_3)_2 \cdot 6H_2O$ + $NH_3 \cdot H_2O$ recipe, there is only a limited amount of free Zn^{2+}, which greatly suppresses homogeneous nucleation and facilitates heterogeneous nucleation, leading to more nucleation sites on seedless substrates [58].

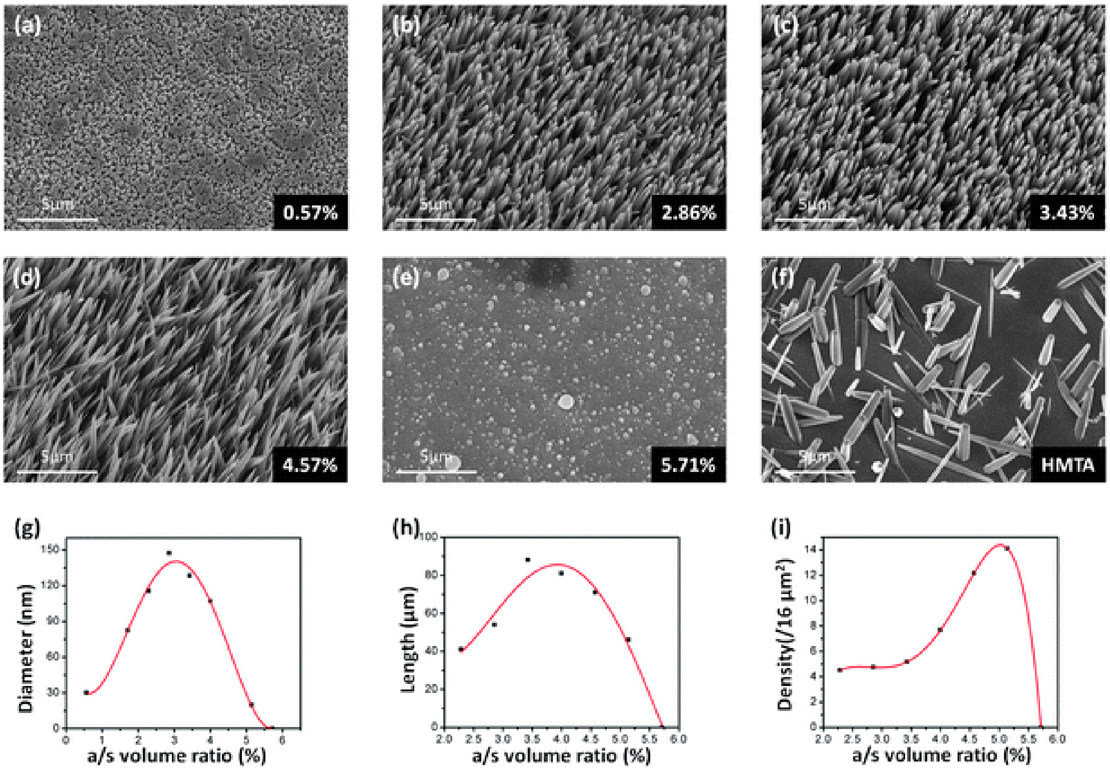

Figure 3: Effects of ammonium hydroxide concentration (a/n volume ratio) on the morphology of ZnO NWs grown on seedless gold layer. (a)-(e) SEM images of NWs grown under a/n volume ratios of 0.57%, 2.86%, 3.43%, 4.57%, and 5.71%, respectively. The scale bar is 5 μm. (f) SEM image of NWs grown with the control recipe of $Zn(NO_3)_2$ $6H_2O$ + HMTA. (g)-(i) Dependence relationship of NW tip diameters, length and density on the a/n volume ratio.

Lastly, a group of experiments were carried out with different a/n volume ratios of 0.57%, 1.71%, 2.29%, 2.86%, 3.43%, 4.00%, 4.57%, 5.14%, and 5.71%. By examining three areas (~16 μm^2) around the center of a substrate with the as-grown NWs, the average diameter, length and density were obtained and plotted in Figure 3 (g), (h) and (i) to show the dependence relationship of these parameters on the ammonium hydroxide concentration. The NW array density reaches its maximum at ~3.43% and the NW length reaches its maximum at ~5.14%. The diameters of the NW tips reach a maximum of ~147 nm at ~2.86% and can be decreased to ~20 nm at ~5.14%. Our results provide a helpful guide of how to use the parameters of the a/n volume ratio or the ammonium hydroxide concentration, to engineer the synthesis process for the desired or optimized morphology of the grown ZnO NW arrays.

B. Solution/container volume ratio

Ammonia hydroxide (28 wt%) is an extremely volatile chemical especially under high temperature. There are three states of ammonia in our reaction system: ammonia ions, ammonia dissolved in the solution and ammonia vapor in the air. A number of factors can affect the equilibrium among these three states. In this section, the concentration of $Zn(NO_3)_2 \cdot 6H_2O$ was kept at 20 mM and the concentration of ammonia hydroxide was kept at 2.5% of the a/n volume ratio. The factor that changes is the volume of the solution, which tunes the equilibrium status of ammonia among the three states. Figure 4 (a) shows the result when the solution volume was kept at a low level of 25 ml in a 500 ml container. A relatively large amount of ammonia would therefore exist as vapor in the free space of the container before an equilibrium partial pressure can be reached, which might lead to a lower level of ammonia concentration (a/n volume ratio) in the solution. However, this does not result in a faster release of Zn^{2+}, since ammonia dissolved in the air will dissolve back into the solution through dynamic equilibrium. This is another buffering mechanism different from the one discussed in section A. Here, the new buffering mechanism helps keep the concentration of both Zn^{2+} and OH^{-} at a relatively low level, further slowing down the reaction rate, resulting in short but better-aligned NWs, as observed. The diameters of the NW tips were large and the shaping effect can be considered negligible, with the absence of a high level of NH^{4+}

concentration. Figure 4 (b) shows the result when the solution volume was increased to 100 ml. The growth of NWs was faster and good alignment was maintained under this condition. The density of NWs decreased, however, due to a shorter nucleation stage and the average length of the NWs was dramatically increased from ~2 μm to~9 μm due to faster growth, while the diameters of the NW tips were slightly decreased due to a weak shaping effect. Figure 4 (c) shows the result when the solution volume was further increased to 300 ml. Following the same trend as discussed above, the density of NWs further decreased while the length of the NWs slightly increased. Needle-like tips occurred for the as-grown NWs due to the significant shaping effect caused by abundant NH^{4+} in the solution.

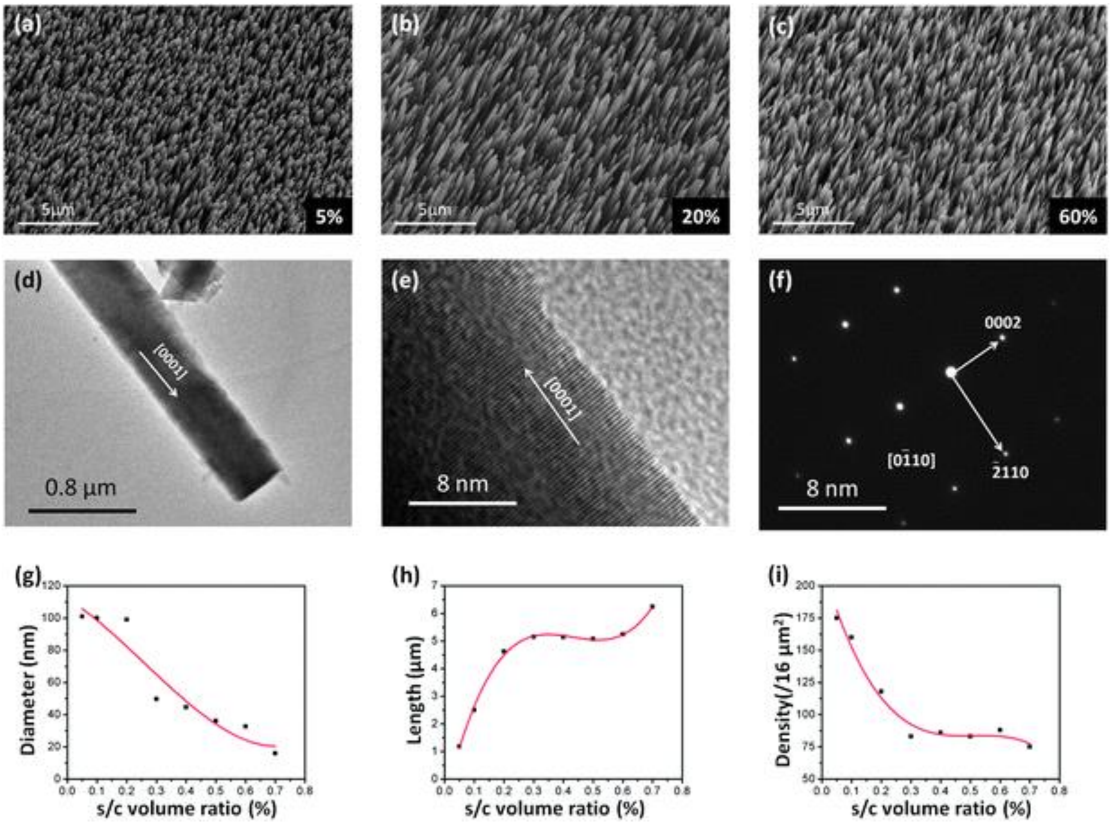

Figure 4: Effects of solution/container volume ratio on the morphology of ZnO NWs grown on a seedless gold layer. (a)–(c) SEM images of NWs grown under different solution/container volume ratios 5%, 20% and 60%. The scale bar is 5 μm. (d) TEM image of a single ZnO NW. The arrow shows its [0001] crystal orientation. The scale bar is 0.8 μm. (e) HRTEM image of a single ZnO NW, indicating its single

crystallinity. The arrow shows its [0001] crystal orientation. The scale bar is 8 nm. (f) Diffraction pattern of a single ZnO NW. The crystal orientation is shown in the image. The scale bar is 8 nm. (g)–(i) Dependence relationship of NW tip diameters, lengths and density on solution/container volume ratio.

Then the as-grown ZnO NWs under several different synthesis conditions were characterized using TEM. The HRTEM images and diffraction pattern obtained show that the ZnO NWs are single crystalline and possess the [0001] orientation along their growth directions regardless of the different synthesis conditions. One set of these images is given in Figure 4 (d), (e) and (f).

Lastly, a group of experiments were carried out with different s/c volume ratios of 0.05, 0.1, 0.2, 0.3, 0.4, 0.5, 0.6 and 0.7. By examining three areas (~16 μm^2) around the center of a substrate with the as-grown NWs, the average diameter, length and density of the as-grown NWs are obtained and plotted in Figure 4 (g), (h) and (i) to show the dependence relationship of these parameters on the s/c volume ratio. The tip diameters and density of NWs increase monotonically with the decrease of the s/c volume ratio. The NW length, although decreasing with the decrease of s/c volume ratio, stays generally stable within the range of 0.2–0.6 s/c volume ratio.

In the above discussion, in addition to the conventionally investigated parameters like temperature, precursor concentration, growth time etc., a new parameter, the partial pressure of ammonia in air has been investigated in detail. The results presented here suggest that by simply manipulating the partial pressure of ammonia gas together with others, the synthesis of ZnO NW arrays of desired morphology can be engineered and optimized in a controlled manner.

C. Patterned growth of ZnO NW arrays on different metal surfaces

Stronger nucleation is one of the advantages of the seedless hydrothermal synthesis method reported here as compared to the control recipe in section A, which was reported previously in other work [44]. To demonstrate the capability of this seedless selective NW growth, ZnO NW arrays were synthesized seedlessly on substrates with pre-patterned metal electrodes. It was found that ZnO would not nucleate on silicon dioxide while significant growth of NWs on areas deposited with suitable metals was observed. Figure 5 (a), (b), (c) and (d) show the SEM images of the as-grown NWs on patterned electrodes of gold, copper, silver and tin, respectively. The insets are the magnified images of the NW array for each case. No post-annealing process was performed for the copper, silver and tin electrodes. The results show that the aligned ZnO NW array can grow selectively and preferentially on these metals, which enables the potential application of this synthesis method for fabricating ZnO NW arrays site-selectively on integrated circuits, which possess a vast amount of, for instance, copper electrodes and interconnects, in a well-controlled manner. This may pave the way for realizing the novel integration of semiconductor NW based piezotronics with state-of-the-art microelectronic technology and strategically coupling the optical, electrical and piezoelectric properties of semiconductor nanomaterials with the high speed computing/processing capability of integrated circuits.

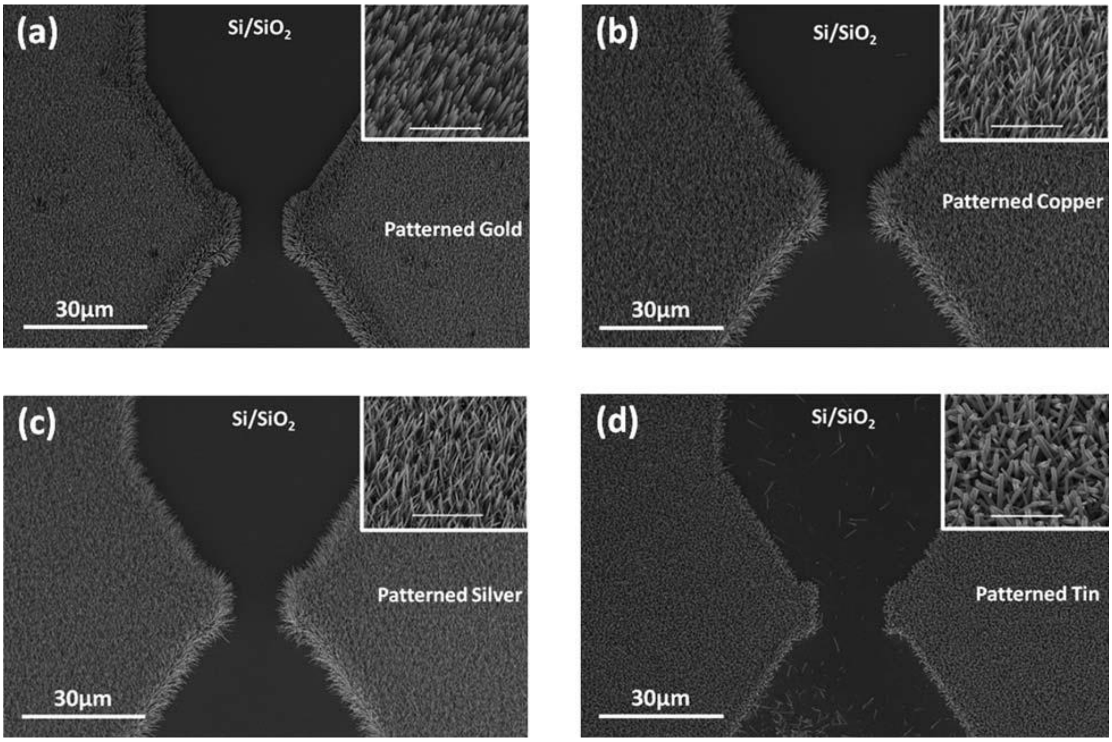

Figure 5: SEM images of the as-grown NWs on patterned metal electrodes. The scale bars for the four figures are 30 µm. The scale bars for the four insets are 6 µm. (a) NWs grown on gold electrodes. (b) NWs grown on copper electrodes. (c) NWs grown on silver electrodes. (d) NWs grown on tin electrodes. Insets are the magnified images of the NWs for each case.

In summary, a method to grow dense and aligned ZnO NW arrays on various patterned metal layers without pre-depositing a seed layer is demonstrated. The effects of ammonia concentration (a/n volume ratio) and solution/container volume ratio (s/c volume ratio) on the NW growth have been investigated in detail and the proposed growth mechanism has been discussed. The strong nucleation for preferential NW growth has been demonstrated by using substrates with patterned layers of various metals. This novel hydrothermal synthesis approach provides the capability to seedlessly grow ZnO NWs on various substrates, enabling the potential applications of ZnO NW arrays for sensing, electromechanical actuation and energy harvesting, etc.

3.3 Synthesis of ZnO thin films

Technologies of thin film synthesis are much more mature than those for NWs. Common methods include physical vapor deposition [59], hydrothermal deposition [60], radio frequency (RF) sputtering [61], molecular beam epitaxy [62] and metalorganic chemical vapor deposition [63]. As we can see, some of the methods can also be used for NW synthesis. The difference is that NW synthesis requires special substrates and strict parameter control. Failure to comply with the requirements will just lead to the formation of thin films. MBE and MOCVD deliver very high quality monocrystalline thin films, which differs them from the rest of the thin film growth techniques. Both are used in the semiconductor industry for the fabrication of electronic and optoelectronic components. The downsides of these technologies, however, are the high facility and maintenance cost and the health hazards they pose to the people who operate them. The growth conditions are very harsh, involving high temperatures, high vacuum and corrosive chemicals. It is thus very challenging to use these two techniques for certain novel applications such as flexible electronics. The regular physical vapor deposition does not involve as complex chemistry and also does not involve hazardous materials. Its mechanism is simply vaporization, transport and deposition. Hence the equipment is relatively simple-structured. Commonly seen PVD systems are the tube furnace, thermal evaporator and electron beam evaporator. This method is much more accessible than MBE or MOCVD but it could only produce polycrystalline or amorphous thin films since the deposition of atoms is random. Hydrothermal deposition of ZnO thin films [64] is almost identical to the hydrothermal growth of ZnO NWs with the only exception being the former uses a much higher concentration of precursors. Therefore, the as-grown thin films could be viewed as densely packed nanorod arrays. Each rod is monocrystalline with its c-axis parallel with its growth direction. However, the rods have random lattice orientation within their c-plane and the physical connections among the rods are weak, making the film fragile to in-plane straining. RF sputtering is a deposition method that materials are ejected from a source target due to the physical bombardment by energetic particles. There are several advantages of this method. Firstly, this process in theory can be used to deposit almost any materials. Secondly, since no vaporization is involved, the substrate temperature is much lower than physical vapor deposition and thus polymer substrates could be used. Thirdly, although the deposition seems random, the bombardment will introduce charges and for materials such as binary non-metals, the static charges will effectively influence the kinetics of the film formation and lead to the tendency of ordered stacking of each layer of atoms. A representing example is the RF sputtering of ZnO thin films where c-axis orientation can be observed [65, 66]. This character is similar to the oriented growth of hydrothermal approach, but the as-grown film is much more uniform and cleaner.

From the above analysis, we can say that for traditional silicon based or III-V based semiconductor technologies, MBE and MOCVD are the better options since they deliver high quality monocrystalline thin films with precisely controlled doping concentrations. For novel applications such as piezotronics, RF sputtering is a good option since the growth of ZnO thin film is oriented and is performed at low temperatures.

4. Piezotronic devices

Since the initialization of piezotronics studies in 2006, a lot of progress has been made to experimentally verify the physics model as well as demonstrating its potential applications. By the time I started working on piezotronics at around 2010~2011, one noticeable character of previous works in the field was that all the piezotronic devices reported were based on individual NWs [16, 67-71]. The fabrication of these devices relied on the manual handling of each single NW which was time consuming, non-scalable and unsuitable for scaled manufacturing. With the concern that single NW devices may severely limit the application potentials of piezotronics, I carried out research projects in two directions in order to address the above issue. The first direction is to scale up the device from a manually fabricated single NW device into a bottom-up auto-assembled NWs array device. Doing so not only leads to manufacturing scalability, but also provides the ability to two-dimensionally map the distribution of strain or applied pressure by measuring localized force applied onto selected NWs from the array. The second direction is to replace the NW materials with more conventional thin film materials as the building blocks. With the precondition that the thin film ZnO does exhibit adequate piezoelectricity, piezotronics could be realized with mature and scalable thin film technology. Under the context that NW technology is not yet ready for the industry, this option offers a promising prospect of a faster commercial application of piezotronics in the near future.

4.1 Taxel-addressable matrix of vertical-nanowire piezotronic transistors for

active and adaptive tactile imaging [72]

Progress in the field of tactile imaging technologies have been made by implementing flexible pressure sensors based on arrays of tactile pixels (taxels) for mimicking the tactile sensing capabilities of human skin. In these sensors, electronic components such as traditional planar FETs act as readout elements for detecting pressure-induced property changes in the pressure-sensitive media [73-77]. Their continued improvement depends on minimizing the effect of substrate strain on the performance of the electronic components while increasing the flexibility of the substrate [78]. This scheme of pressure sensing not only requires complicated system integration of heterogeneous components but also lacks direct and active interfacing between electronics and mechanical actuations. Moreover, the sizes of as-fabricated taxels are hundreds of micrometers to tens of millimeters, severely limiting device density and spatial resolution. Although architectures such as 3D integrated circuits and wrap-gate vertical transistors present attractive approaches to achieving high-density assembly of functional nanodevices [79-82], it is cumbersome to fabricate the gate electrode and manage the interconnect layout so as to effectively control an individual device within a high-density matrix. A schematic of a representative wrap-gate NW FET is shown in Figure 6 (a).

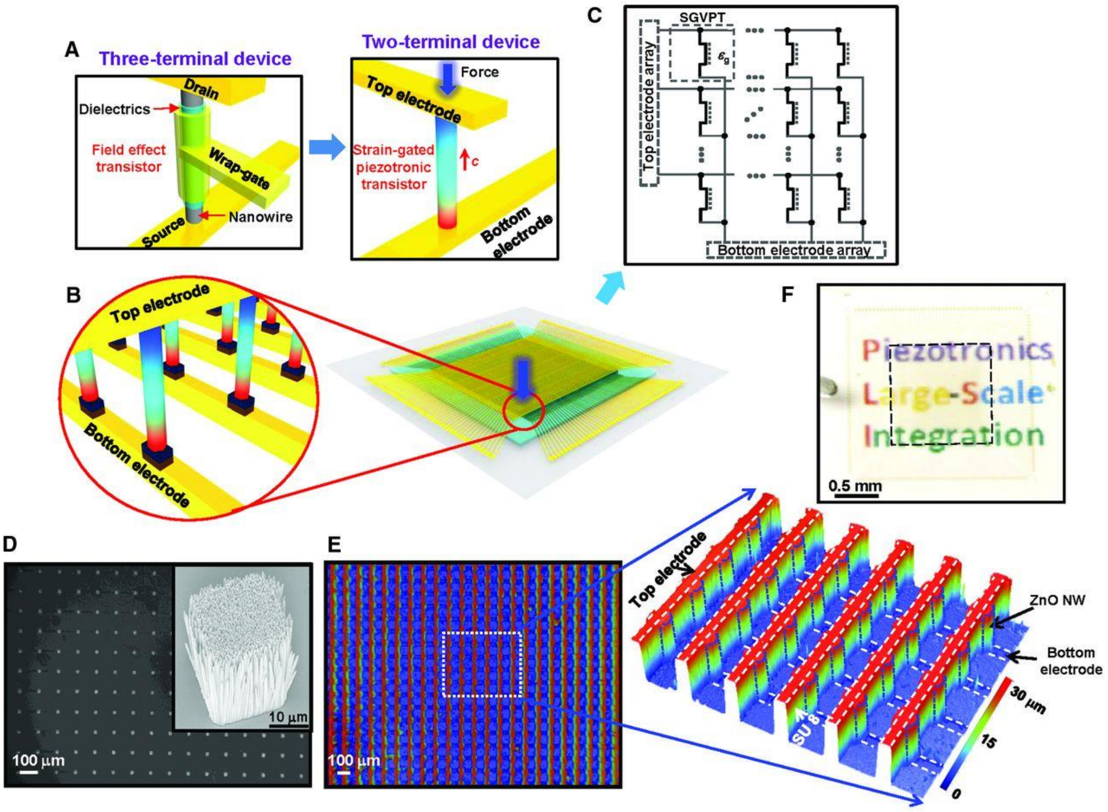

Figure 6: Schematic illustration, optical and electron microscopic images, and topological profile image of 3D SGVPT array assembly. (A) Comparison between three-terminal voltage-gated NW FET (left) and two-terminal strain-gated vertical piezotronic transistor (right). (B) Schematic illustration of a 3D SGVPT array with taxel density of 92 × 92 and scheme for spatial profile imaging of local stress by the array. (C) Equivalent circuit diagram of the 3D SGVPT array. (D) Scanning electron micrograph of SGVPT array taken after etching back the SU 8 layer and exposing top portions (~20 µm) of the ZnO NWs. Inset shows 30 °-tilt view of the exposed ZnO NWs for a single taxel. (E) Topological profile image of the SGVPT array (top view). At right, a 3D perspective view of the topological profile image reveals the vertical hierarchy of the SGVPT assembly; the color gradient represents different heights. (F) Optical image of the transparent 3D SGVPT array on a flexible substrate. The peripherals are the pads of the device, and the central region highlighted by black dashed lines is the active array of 3D SGVPTs.

This work aims at scaling from single NW piezotronic devices to NWs array piezotronic devices in order to achieve tactile imaging that resolves the limitations in existing technologies. As explained earlier, a piezotronic transistor is a two terminal transistor gated by strain applied on the channel material. In addition to providing a high force/pressure sensitivity, the elimination of wrap gates offers a new approach for 3D structuring. The basic structure of a 3D strain-gated vertical piezotronic transistor

(SGVPT) (Figure 6 (a), right) consists of one or more vertically grown ZnO NWs in contact with bottom and top electrodes. Each ZnO NW experiences axial strain when subjected to external mechanical deformation. By combining the patterned in-place growth of vertically aligned ZnO NWs with state-of-the-art microfabrication techniques, large-scale integration of a SGVPT array can be obtained. Figure 6 (b) illustrates a 1 cm^2 SGVPT array with a taxel density of 92 × 92 (234 taxels per inch). The equivalent circuit diagram of the SGVPT (Figure 6 (c)) shows the operation scheme of the SGVPT device circuitry. The taxel area density of the SGVPT array is 8464 cm^{-2}, which is higher than the number of tactile sensors in recent reports (~6 to 27 cm^{-2}) and mechanoreceptors embedded in human fingertip skin (~240 cm^{-2}) [83]. A detailed description of the device fabrication process is shown in Figure 7 and 8.

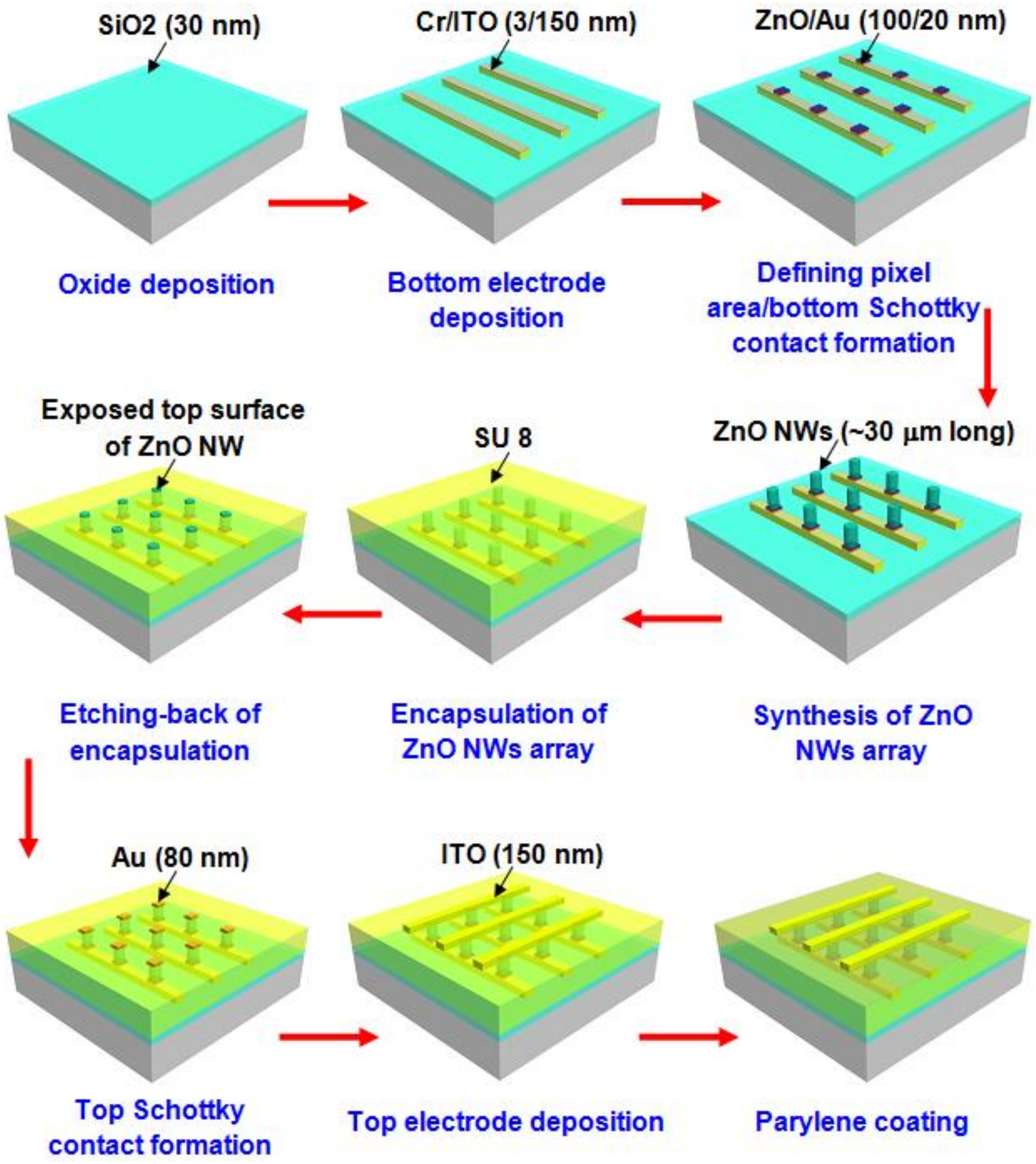

Figure 7: Schematic illustration of processing steps for fabricating 3D vertical piezotronic transistors array on a PET substrate. The steps are: 1. Deposit a thin layer of SiO2 (30 nm) to the PET substrate via electron-beam evaporation; 2. Use UV lithography, RF sputtering and ebeam evaporation to fabricate bottom ITO/Cr electrodes; 3. Use UV lithography and ebeam evaporation to fabricate Au/ZnO seed layer; 4. Hydrothermally synthesize ZnO NWs array; 5. Spin coat and cure SU-8 to serve as an encapsulation layer; 6. Use reactive ion etching to remove part of the SU-8 so that tips of ZnO NWs are exposed; 7, Use UV lithography and ebeam evaporation to fabricate top Au contact electrodes; 8, Use UV lithography and RF sputtering to fabricate top ITO electrodes; 9, Use thermal evaporation to deposit parylene as a packaging layer.

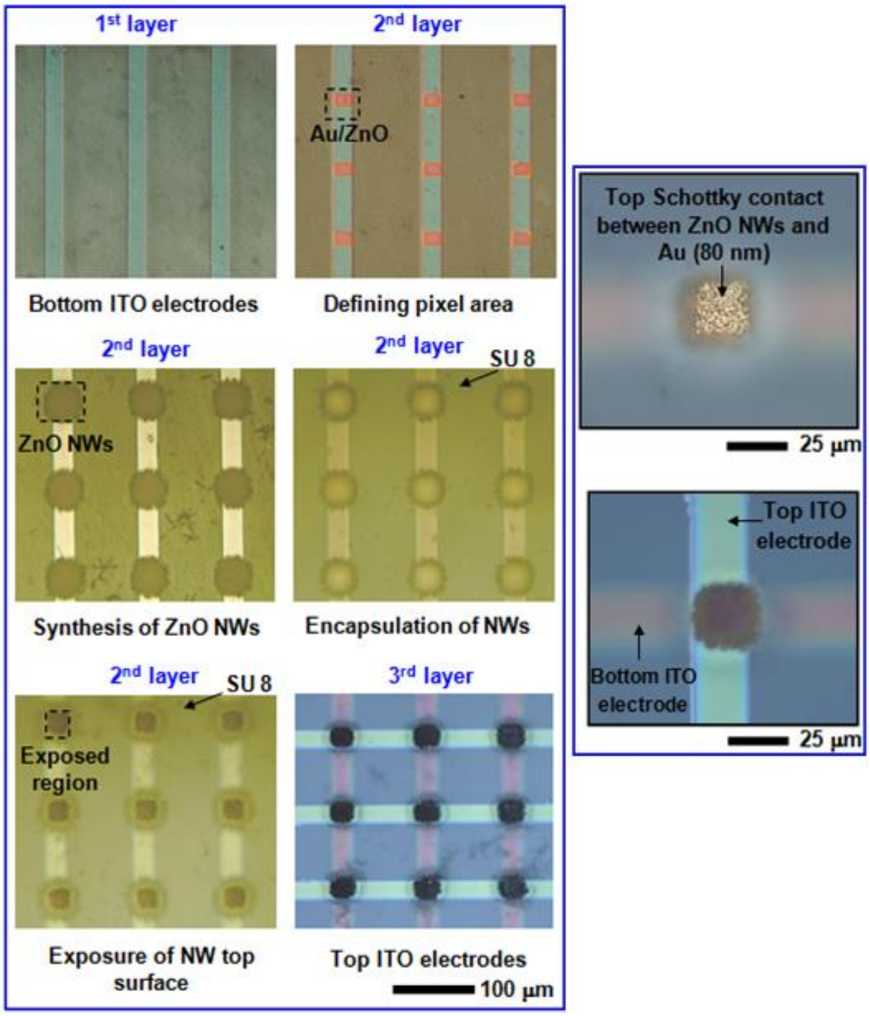

Figure 8: Left: Optical micrographs illustrating 3D vertical piezotronic transistors array on a PET substrate at each major step of fabrication process. Right: Magnified images of top Schottky contacts and single taxel after fabrication of 3rd layer electrode.

Briefly, the active array of SGVPTs is sandwiched between the top and bottom ITO electrodes, which are aligned in orthogonal cross-bar configurations. A thin layer of Au is deposited between the top and bottom surfaces of ZnO NWs and the top and bottom ITO electrodes, respectively, forming Schottky contacts with ZnO NWs. A thin layer of Parylene C is conformably coated on the SGVPT device as the moisture and corrosion barrier. Well-aligned ZnO NWs, synthesized by a low-temperature hydrothermal method (22), function as the active channel material of the SGVPT and help reduce the stochastic taxel-to-taxel variation to ensure uniform device performance. Figure 6 (d) and Figure 9 show the as-grown ZnO NWs array. The as-synthesized ZnO NWs show single crystallinity.

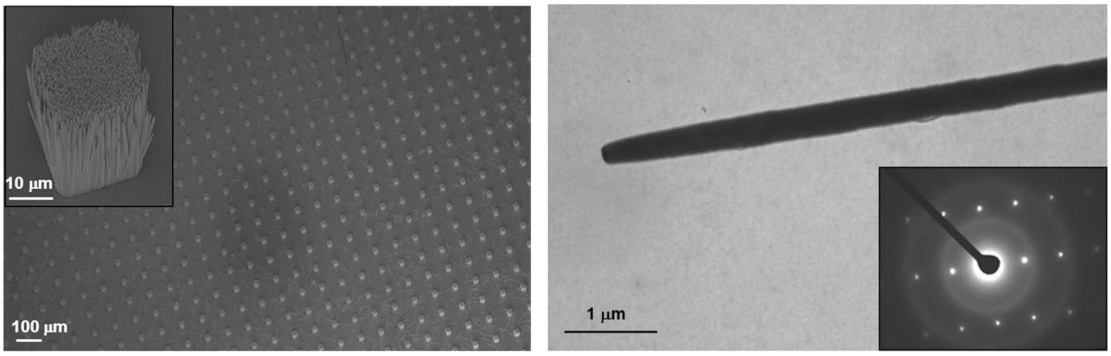

Figure 9: Left: 30° tilted SEM image of 3D SGVPT array with top portions (~ 20 µm) of ZnO NWs (total length ~ 30 µm) exposed, showing the bunched growth of nanowires. Right: A TEM image and selective area electron diffraction pattern from the nanowire, confirming its single-crystalline nature of the as-synthesized ZnO NWs from SGVPT array.

The 3D nature and vertical hierarchy of the SGVPT assembly is revealed by topological profile imaging (Figure 6 (e)) using an optical noncontact profilometer (Wyko Profilometer NT3300), which measures the phase change of light reflected from various heights in the structure by interferometry. The high degree of alignment and uniformity of the SGVPT array in three dimensions (~30 µm in height, 20 µm × 20 µm in taxel size) is enabled by process control in both the bottom-up synthesis of NWs and the top-down fabrication of circuitry. The use of a two-terminal configuration based on the piezotronic effect simplifies the layout design and circuitry fabrication while maintaining effective control over individual devices. The transparency and flexibility of SGVPT array devices are shown in Figure 6 (f) and Figure 10.

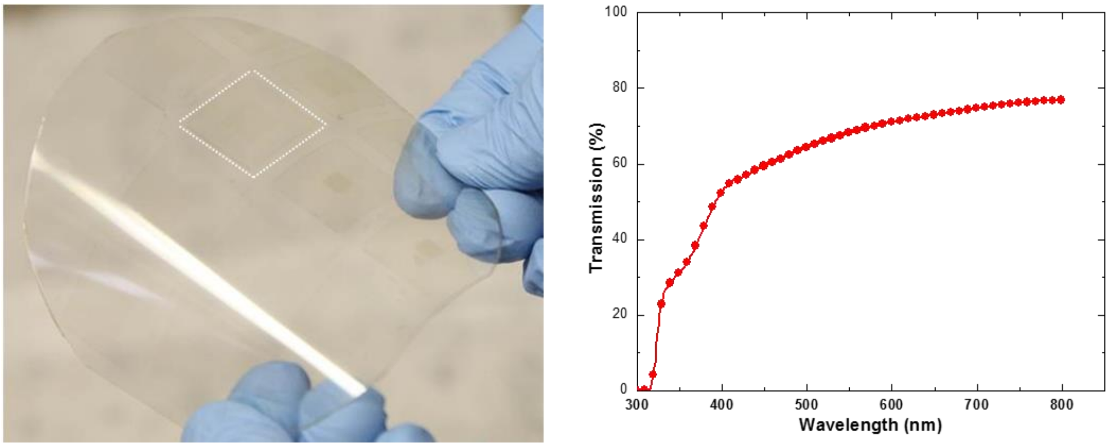

Figure 10: Left: Image of 3D vertical piezotronic transistors arrays on a 4-inch PET substrate. Four configurations of array with different taxel densities and spacing are fabricated here using the processing steps described in Figure 7. The region outlined by white dashed lines represents the device with taxel density of 92 x 92 in 1 cm^2. Right: Measured normal incidence transmission (T) spectra of 3D vertical piezotronic transistors array (ITO/Cr/Au/ZnO NWs/Au/ITO: 150 nm/3 nm/20 nm/30 µm/80 nm/150 nm) on a PET substrate (~ 500 µm thick).

By selecting one top electrode, the 92 taxels between this top electrode and the corresponding bottom electrodes can be addressed and characterized individually. Representative data from 23 taxels in a typical single-channel line scan (1 × 92) measurement for a SGVPT array device are shown in Figure 11. The corresponding topological profile images (top view) of the selected taxels are displayed at the top of Figure 11 (a). The current response from each taxel under 1 V bias, with and without external pressure (20 kPa) applied to a localized region (around taxels 45 and 46), is recorded and plotted, with colors representing the ratio of the response amplitude for each taxel in an 80 s window. It can be seen that for this single-channel array of SGVPTs, pressure variations can be distinguished with both high sensitivity and spatial resolution (taxel periodicity, ~100 µm). The dominant mechanism for the transport property of SGVPT is the piezotronic effect rather than the piezoresistance effect, as experimentally confirmed and elaborated (Figure 12). Data from single-channel conductance measurements in the temporal domain are compiled and shown in Figure 11 (b) and Figure 12 to further illustrate the dynamic response of SGVPT devices. Distinctive changes in conductance can be observed for taxels 45 and 46 before and after applying the localized pressure. Although the measured response time (rise time) of ~0.15 s for a SGVPT taxel (Figure 12) is larger than that of human fingertips (~30 to 50 ms), it is comparable to previously reported values of 0.1s [73]. These results indicate that a SGVPT array can respond to static as well as dynamic stimuli. The response time can be further improved in future designs by integrating local on-site signal processing circuits with a SGVPT array [84].

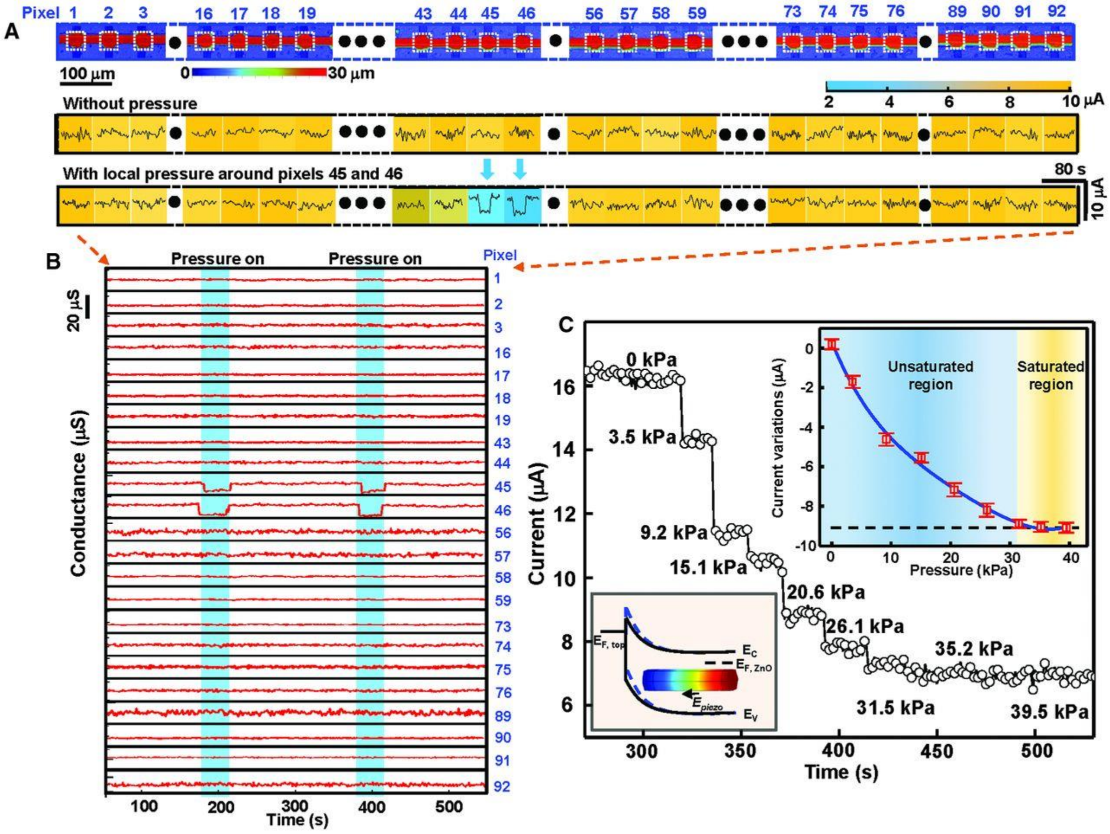

Figure 11: (A) Topological profile images (top view) of 23 selected taxels in a 1 × 92 SGVPT array and their corresponding current responses under 1 V bias without and with external stress (20 kPa) applied to a localized region around taxels 45 and 46. (B) Single-channel conductance measurement in the

temporal domain, illustrating the dynamic response of the 23 selected SGVPT devices in this channel, without and with pressure applied. (C) Current responses for taxel 46 under different pressures, showing the gate modulation effect of applied pressure on the electrical characteristics of the SGVPT. Top right inset: Current variations (red squares) are plotted versus the applied pressures. Bottom left inset: Schematic band diagram illustrating the change in SBH of the reverse-biased top contact due to the modulation effect of strain-induced piezopotential. The original band edges at the reverse-biased Schottky contact for the SGVPT device without stress applied are shown as black solid lines. The band edges bending at the reverse-biased Schottky contact for the SGVPT device with stress applied are shown as blue dashed lines.

The pressure sensitivity of a single SGVPT is shown in Figure 11 for taxel 46. We applied increasing pressure at a fixed location on the SGVPT and measured the variations in current response. The SGVPT device demonstrated high sensitivity for detecting pressure change, particularly in low-pressure regions (<10 kPa). A plot of current variation versus pressure change (Figure 11 (c), top right inset) shows the modulation effect of applied pressure. It can be seen that the maximum pressure at which a SGVPT taxel can still distinguish without “saturation” is around 30 kPa, above which the current saturates. The observed sensing range of a few kPa to ~30 kPa for a SGVPT array is well matched to the range of pressure that a human finger applies to sense texture and shape, 10 to 40 kPa [85]. The sensitivity of a SGVPT, defined as $S = dG_{SGVPT}/dP$ (where G is the measured conductance for SGVPT), is around 2.1 $\mu S\ kPa^{-1}$; this value arises from the change in carrier transport of the SGVPT by applied pressure due to the corresponding modulation of barrier height at the reverse-biased Schottky contact by strain-induced piezopotential.

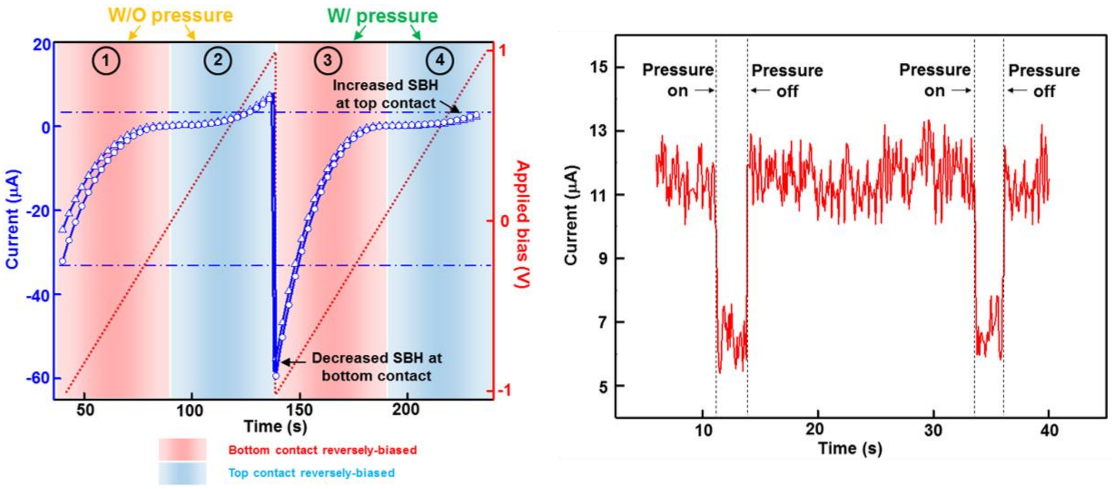

Figure 12: Left: Experimental verification of piezotronic effect in operation of SGVPT devices, showing asymmetric tuning of the current under positive and negative voltages. Right: The measured response (rise) time for SGVPT taxel is around 0.15 s. The applied pressure is ~ 15 kPa.

The conductance of a SGVPT device is dictated by the reverse-biased Schottky contact, which is formed between ZnO NWs and top electrodes in this case. Upon applying the normal stress, accumulation of piezoelectric charges at both Schottky contacts induces the distribution of piezopotential. Because of the orientation of the polar c-axis in the as-synthesized ZnO NWs (red arrow in Figure 6 (a), right panel), negative piezopotential is induced at the reverse-biased top Schottky contact, which raises the barrier height at that contact and hence decreases the transport conductance of the SGVPT taxel, as depicted by the schematic band diagrams in Figure 11 (c) (bottom left inset). The operation of the SGVPT device is therefore based on barrier-interface modulation that enables enhanced sensitivity and efficiency relative to the channel modulation operation in conventional FETs. The quality of the Schottky contacts has been characterized, as shown in Figure 13.

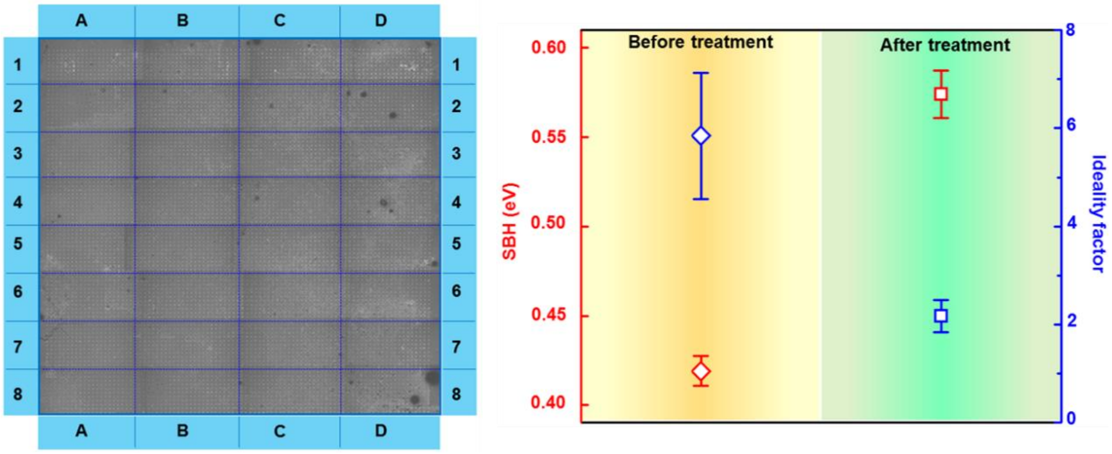

Figure 13: Left: Top view of the entire 92 x 92 SGVPT array, which has been divided into 32 regions. Right: Experimentally obtained Schottky barrier heights (SBHs) and ideality factors for 32 randomly selected taxels from the above 32 regions with (green region) and without (yellow region) oxygen plasma treatment, showing the significant improvement of Schottky contact quality in SGVPT taxels after the treatment.

The SBHs and ideality factors of the formed contacts for devices without extra oxygen plasma treatment before depositing the top electrode are 0.419 ±0.011 eV and 5.84 ± 1.29 respectively, whereas the SBHs and ideality factors of the formed contacts for devices with extra oxygen plasma treatment before depositing the top electrode are found to be 0.575 ±0.013 eV and 2.17 ±0.33, respectively. These results indicate that the qualities of as-fabricated Schottky contacts have been improved by the oxygen plasma treatment [69].

The feasibility and scalability of the proposed integration scheme are demonstrated by the successful fabrication of the 92 ×92-taxel SGVPT array, enabling a factor of 15 to 25 increase in number of taxels and a factor of 300 to 1000 increase in taxel area density relative to recent reports [73-75, 77]. The output current of each individual SGVPT taxel is measured and averaged within a short duration window of 10 ms. By monitoring the output current of each independently functioning SGVPT in the matrix, a spatial profile of applied pressure can be readily imaged by multiplexed addressing of all the taxels. A 2D current contour plot was thus obtained by registering the measured current to the corresponding taxel coordinates along the x (bottom electrode) and y (top electrode) axes. Metrology mapping was then performed on the fully integrated SGVPT array without applying pressure (Figure 14 (a), inset), demonstrating that all of the 8464 SGVPTs within the array are functional. Subsequent statistical investigation revealed good uniformity in electrical characteristics among all taxels, with 95% of the SGVPTs possessing current values in the narrow range of 13.7 ± 2.73 μA under 1 V bias (Figure 14 (a)). The uniformity in the current distribution of SGVPTs can be further improved by optimizing the fabrication process, such as achieving a uniform number of ZnO NWs within each taxel and obtaining even profiles in the etch-back step of the SU 8 layer. To demonstrate the tactile sensing capability of the integrated SGVPT array, we applied a normal stress of ~25 kPa to the device by pressing a hexagonal mold. As shown in Figure 14 (b), which presents for each taxel the difference between current values before and after applying the normal stress, the profile of applied stress can be spatially imaged.

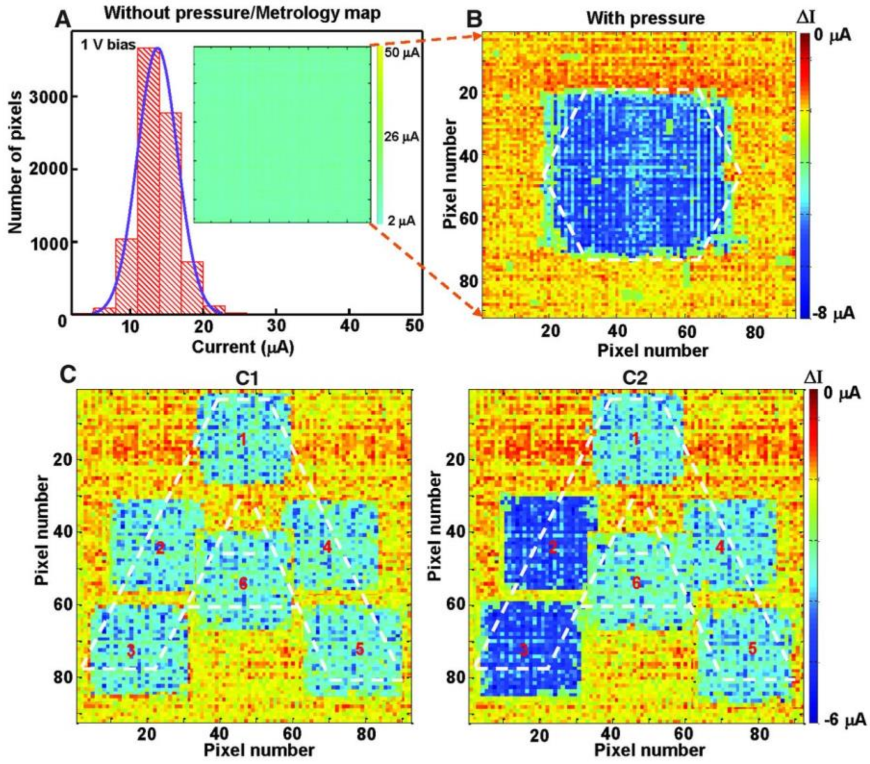

Figure 14: Tactile imaging and multidimensional sensing by the fully integrated 92 × 92 SGVPT array. (A) Metrology mapping (inset) and statistical investigation of the fully integrated SGVPT array without applying stress. (B) Current response contour plot illustrating the capability of SGVPT array for imaging the spatial profile of applied stress. Color scale represents the current differences for each taxel before and after applying the normal stress. The physical shape of the applied stress is highlighted by the white dashed lines. (C) Multidimensional sensing by an SGVPT array exhibits the potential of realizing applications such as personal signature recognition with maximum security and unique identity. The shape of a "written" letter A is highlighted by the white dashed lines.

The SGVPT devices remained operational and capable of imaging the spatial profile of applied pressure after 24 hours of immersion in 23 ℃ deionized water and 37 ℃ 0.9% saline solution, as well as after 6 hours of immersion in 65 ℃ deionized water and 65 ℃ 0.9% saline solution (Figure 15), indicating good stability and feasibility of SGVPT array operation for future applications such as in vivo physiological sensing in complex environments. Deteriorated adhesion between the encapsulation SU 8 layer in the SGVPT array and the substrate was observed for devices after prolonged immersion (12 hours) in both solutions at 65 ℃. Note that even in such cases, the top electrodes and taxels remained in good shape; only rupture of the bottom electrodes can be seen.

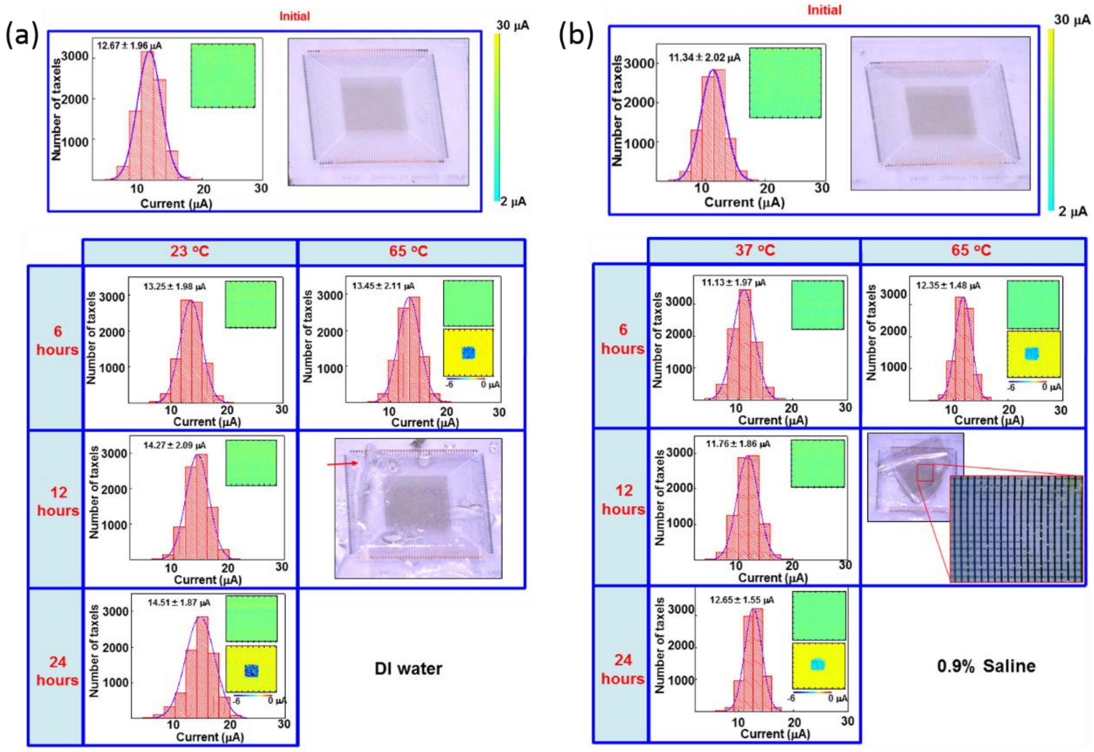

Figure 15: (a) Aging effect of humidity on SGVPT array performance. The pressure applied for device after 24 hours immersion in 23 °C DI water and 6 hours in 65 °C DI water is ~ 15 kPa. (b) Aging effect of physiological environment on SGVPT array performance. The pressure applied for device after 24 hours in 37 °C 0.9% saline solution and 6 hours in 65 °C 0.9% saline solution is ~ 15 kPa.

To investigate whether a single device array could resolve the stress profile spatially while also registering the stress variations to the mapped geometrical pattern (as enabled by the uniform sensitive response of taxels across the whole array and the high spatial taxel density), we used a SGVPT device (Figure 14 (c)) fabricated on a solid silicon substrate. A three-axis stage and force gauge was used to apply normal stresses with well-determined values and spatial locations to the device. The first group of six normal local stresses, each around 8.1 kPa, were applied to the array at preprogrammed locations in a sequence indexed from 1 to 6, with the corresponding contours imaged and organized (Figure 14 (c), panel c1) to emulate the process of writing the letter A. This process was achieved by varying the x and y coordinates while keeping the z coordinate constant in the control interface of the three-axis stage. It can be seen from Figure 14 (c) (panel c1) that spatial profiles of all six applied stresses can be distinguished and mapped electronically. The second group of six normal stresses with the same locations were then applied to the array in the same sequence, except that the stresses applied at sites 2 and 3 were increased to ~20 kPa; stresses at the other four sites were unchanged. The corresponding mapped contours were again recorded and organized (Figure 14 (c), panel c2). These results demonstrate the potential of using an SGVPT array for future applications such as multidimensional signature recording, which not only records the calligraphy or signature patterns when people write, but also registers the corresponding pressure or force applied at each location (dictated by the resolution of the taxel array) by the writer. This augmented capability enables personal signature recognition with unique identity and enhanced security.

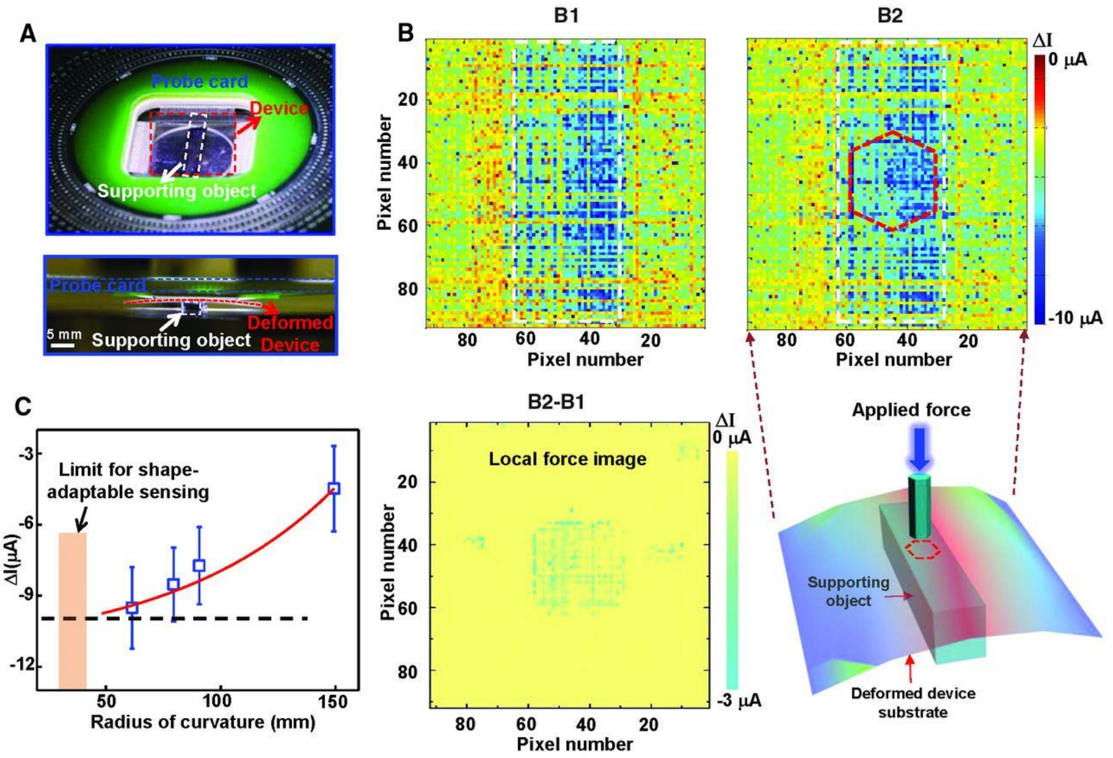

Figure 16: Shape-adaptive sensing by the flexible 92 × 92 SGVPT array. (A) Photographs of the experimental setup for investigating the feasibility of a SGVPT array for shape-adaptive sensing. Upper image, top view; lower image, side view with the device deformed. (B) Shape-adaptive sensing of the SGVPT array. (B1) The measured difference in taxel currents for the SGVPT array with and without a supporting object beneath. The detected shape change of the SGVPT array is illustrated by the dark blue regions; the physical shape of the supporting object beneath the SGVPT device is outlined by the white dashed lines. (B2) The measured variations in taxel current values between bent the SGVPT array with extra stress and the unstrained SGVPT array. The location of the extra stress is outlined by the red dashed lines. (B2–B1) A clearer demonstration of the data is obtained by numerically subtracting B1 from B2, giving rise to spatial imaging of the additionally applied stress when the shape of the SGVPT device is changed. The 3D schematic drawing at the lower right illustrates the process for shape-adaptive sensing. (C) Experimental results show the limit for shape-adaptable sensing by a SGVPT array with the present design.

The real-time detection of shape changes caused by stretching or twisting is a desirable feature for sensors embedded in an artificial tissue or prosthetic device. Figure 16 (a) shows the experimental setup for investigating the feasibility of a SGVPT array for shape-adaptive sensing. A rectangular supporting object is affixed to the platen of probe station, directly beneath the central region of the SGVPT array. After the probe pins are in contact with the pads at the periphery of the SGVPT device, the platen is further raised up so that the device is bent by the supporting object beneath (Figure 16 (a), bottom) with a radius of curvature of ~79.63 mm. The plot of measured difference in taxel currents with and without the supporting object (Figure 16 (b), panel b1) illustrates a good agreement between the detected shape change of the SGVPT array and the physical shape of the supporting object beneath. The shape-adaptive sensing capability was further examined by applying an additional localized stress to the bent SGVPT array, using the same setup in Figure 14 (b) and (c), as depicted by the 3D schematic drawing in Figure 16 (b) (bottom right). The measured variation in taxel current values between the bent SGVPT array with extra stress and the unstrained SGVPT array is shown in Figure 16 (b) (panel b2). A clearer demonstration of the data can be obtained by numerical subtraction (Figure 16 (b), panel b2–b1), which gives rise to spatial imaging of the additionally applied stress when the shape of the SGVPT device changes. Such shape-adaptive sensing has also been investigated for other radii of curvature (Figure 17). Because of the relatively large thickness of the SGVPT device (mainly contributed by the polyethylene terephthalate substrate, which is 500 μm thick), the saturation of SGVPT response under high pressure, and the constraints of the measurement setup (e.g., limited vertical movement of probes), the SGVPT array is unable to sense the change in device shape and further distinguish the applied pressure when the radius of curvature is smaller than 30 to 35 mm (Figure 16 (c)). The detectable range of shape deformation (and of the corresponding shape-adaptive sensing) can be improved by engineering the device into more compliant form to reduce the strain induced in the SGVPT as a result of changes in device shape.

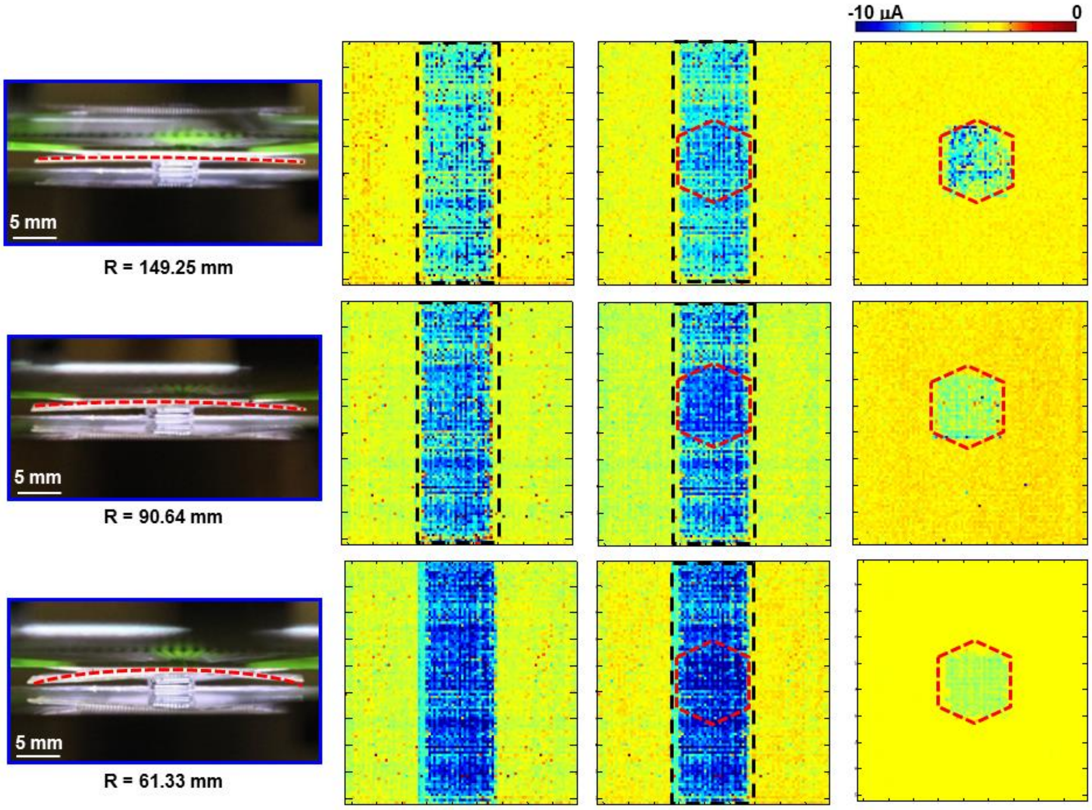

Figure 17: Shape-adaptive sensing for different bending radii of 149.25 mm, 90.64 mm and 61.33 mm. Internal strain detection and external strain sensing upon bending are shown respectively.

A SGVPT array was repeatedly bent to a very small radius of curvature (15 mm, as shown in Figure 18) at a frequency of 2 Hz to simulate accelerated aging. Metrology mapping was then performed on the array and plotted for comparison with that of the device before the cyclic bending. No obvious degradation in SGVPT array operation could be observed even after 1000 cycles of bending, suggesting good reliability and stability in device operation.

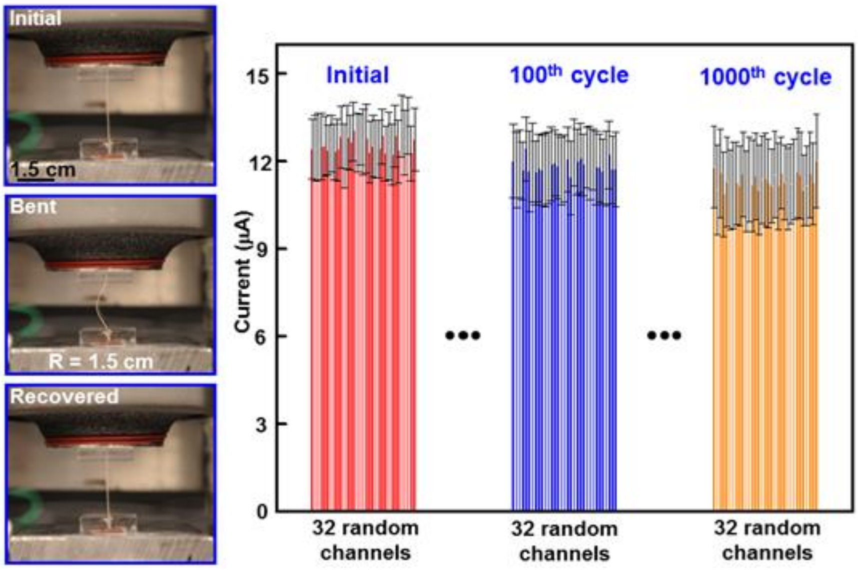

Figure 18: Cyclic test investigating the reliability and stability of SGVPT array operations. Taxel current with 1 V bias for 32 random channels (each with 92 taxels) was monitored and statistically investigated as well as plotted here.

4.2 Piezotronic effect in flexible thin-film based devices [86]

The success of semiconductor technology, which has led to advancement of modern electronics and optoelectronics over the past few decades [87, 88] is enabled by thin-film processing that provides engineering control over material properties as well as scalable integrated fabrication processes. Considering the technological compatibility, piezoelectric semiconductor thin films could be the excellent alternative to 1D counterpart for realizing piezotronic applications. For applications like electromechancial sensing and human-machine interfacing, flexible polymer substrates and hence compatible low-temperature growth of active materials are required. On the other hand, the presence of piezoelectricity does not necessarily rely on single-crystallinity, but rather requires the alignment of polar axis of the grains, which is also achievable in polycrystalline films deposited by non-epitaxial techniques due to selftexturing phenomena and lack of center of symmetry in the as-deposited textured structures[89, 90]. Taking into account of factors such as growth uniformity, reproducibility, process compatibility and scalability, RF sputtering is the technique of choice for our investigations on thin film based piezotronic effect and related potential applications.

This work is the first study of piezotronic effect in RF-sputtered semiconductor thin films. The structural properties of engineered ZnO thin film in this work are characterized before further integrating it into functional piezotronic devices. Modulation of charge carrier transport via piezotronic effect is successfully demonstrated in these thin film based devices, and the underlying mechanism is also discussed. Moreover, the tuning effect of strain-induced piezopotential on the UV sensing capability of thin-film piezotronic device has been investigated. This study shows the possibility of building thin film based piezotronic devices for technological applications.

First, ZnO thin film with controllable property was grown via RF sputtering on flexible PET substrates for structure analysis. Parameters such as chamber pressure, sputtering power, mixing ratio of gases as well as sputtering temperature are manipulated systematically to achieve optimized piezoelectric characteristics and charge carrier density of the sputtered ZnO thin film. Specifically, the chamber pressure and sputtering power were set at 12 mTorr and 125 W respectively to achieve a reasonable growth rate.

The sample holder was heated up to 100 ℃ during the growth process to improve crystallinity of the as-sputtered film. Finally, the as-grown ZnO thin film was treated with oxygen plasma before electrode fabrication for improved electrical contacts. The dominant diffraction peak in the X-ray diffraction (XRD) (Figure 19 (a)) for the as-grown film centers around 2θ = 34.3°, which corresponds to the (0002) plane of Wurtzite ZnO. The other observable diffraction peak within the range of (25°, 40°) is the peak arising from non-equilibrium growth. This result indicates that <0001>, corresponding to the c-axis of Wurtzite ZnO, is the preferred growth direction and suggests that the as-grown film consists of multiple mesoscopic columnar grains. As is schematically shown in the inset of Figure 19 (a), alignment of the c-axes within these columnar grains gives rise to macroscopic piezoelectricity of the ZnO polycrystalline thin film. To obtain further in-depth structural analysis, the ZnO thin film sputtered on flexible substrates (PET in our case) was examined using TEM. The incompatibility of flexible substrates for cross-section TEM sample preparation was overcome by introducing a transfer technique as described in Figure 19 (b). A sacrificial layer of photoresist (NR9-1500PY) was spin-coated onto the PET substrate before the subsequent growth of ZnO thin film, with the sputtering parameters specified above. A silicon substrate was attached to the as-grown ZnO film with epoxy gel and the sample was then baked at 85 C ° for an hour to improve epoxy's resistance to solvents. Lastly, the sample was put into acetone to dissolve the sacrificial layer and the ZnO thin film was successfully transferred from PET substrate to silicon substrate, which is compatible with TEM sample preparation. The TEM characterization results are shown in Figure 19 (c). Bright field and dark field cross-sectional TEM images of the transferred ZnO thin film are shown in Figure 19 (c1), confirming the columnar-grain structure of as-sputtered film. Electron diffraction pattern is shown in Figure 19 (c2) and the arc-shaped diffraction spot of (0002) further proves the alignment of c-axes among the columnar grains of the as-grown ZnO thin film. The 24 °spread angle of the spot relative to the center of the pattern indicates that most grains have their c-axes lie within the range of -12 °~12 °relative to the normal direction of the substrate. Figure 19 (c3) and Figure 19 (c4) present high resolution TEM (HRTEM) images at two different locations along the boundary, clearly showing that the c-planes are generally parallel to the boundary for both grains. In addition, from the diffraction pattern in the two insets, it can be seen that while their c-axes are aligned along the same direction, there is a 30 ° in-plane rotation relative to each other. This implies that the as-sputtered film has no preferred crystal orientation in directions perpendicular to the overall effective c-axis, which leads to the cancellation of the overall piezoelectric effects perpendicular to the c-axis. These results discussed above fully support the conclusion that the as-sputtered ZnO thin film on PET substrates has columnar grains with preferred c-axis orientation and thus is piezoelectric.

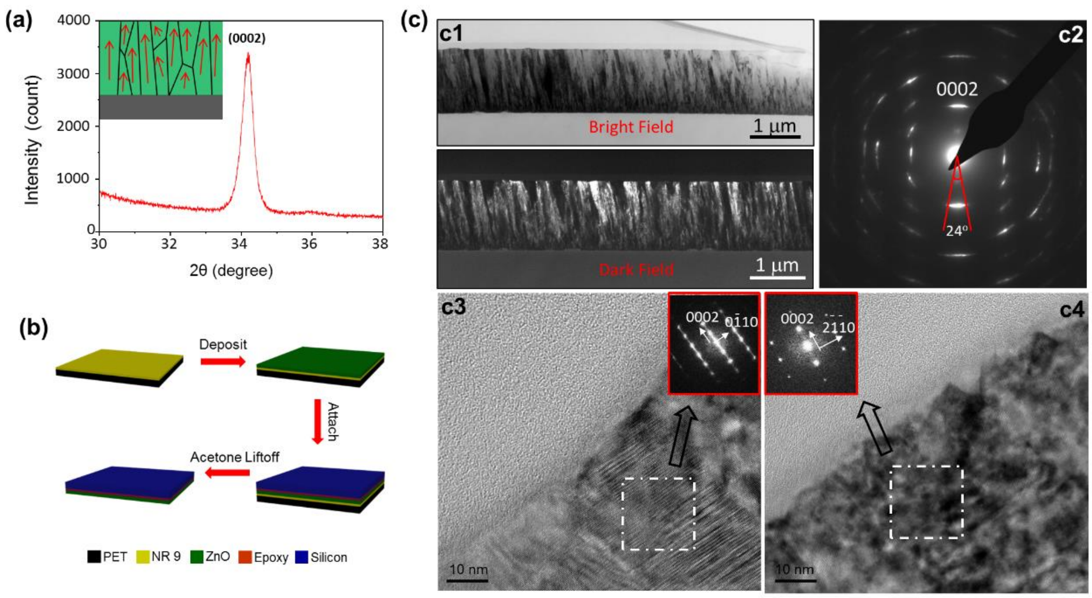

Figure 19: Structure characterization of the polycrystalline ZnO thin film grown by RF sputtering onto PET substrates. (a) XRD diffraction spectrum of the ZnO thin film. (b) Schematics on how to transfer the as-sputtered ZnO thin film from PET to silicon for TEM sample preparation. (c) TEM characterization results. (c1) shows the bright field and dark field cross-sectional TEM image of the thin film. (c2) shows the diffraction pattern of the thin film. (c3) shows the HRTEM images of two different locations along the boundary. The corresponding diffraction patterns are shown in the insets.

In order to conclude the polarity of the corresponding electric field, the polarity of the film needs to be determined. Here, piezoelectric tests were performed for this purpose, by investigating the strain-induced electrical outputs of as-assembled device, which has the metal-ZnO thin film-metal structure. A layer of 5 nm chromium (Cr) was deposited onto PET first by electron-beam evaporation to serve as the bottom electrode and adhesion layer. Then part of the Cr layer was masked and ZnO thin film was subsequently grown on selectively-exposed region of the Cr layer by RF sputtering. Finally, a layer of 5 nm Cr top electrode was deposited on ZnO thin film. The device was then connected to a voltage pre-amplifier, firstly with the top side of the device connected to the positive pole, as sketched in Figure 20 (a). The linear actuator was programmed to apply mechanical strains by periodically pushing, holding and releasing the device while corresponding electrical outputs from device were acquired. As can be seen from the typical voltage signals generated by the device upon straining (Figure 20 (a)), when the device was pushed by the actuator, ZnO thin film was subject to compressive strain and a negative electric pulse was recorded. After holding the sample for 1 s, the pressing force was released and a positive electric pulse can be observed. Since positive piezopotential occurs at the positive side of c-axis when ZnO is under tensile strain and negative piezopotential occurs at positive side of c-axis when ZnO is under compressive strain, the above observed results indicate that c-axis of the as-sputtered ZnO thin film grown on PET substrate is pointing up and away from the PET/ZnO interface (Figure 20 (a)). To verify this, connection to the two poles of voltage-preamplifier was switched and it can be seen from Figure 20 (b) that a positive pulse was generated upon pushing and a negative pulse was observed upon releasing the sample, which is consistent with the above conclusion. A control test was also performed by replacing the PET substrate with titanium foil while maintaining all other parameters unchanged. By comparing the results obtained from control group in Figure 20 (c) with those in Figure 20 (b), it can be concluded that as-sputtered ZnO thin film grown on titanium foil possesses the opposite c-axis polarity to that grown on PET substrate, with its c-axis pointing down towards the Ti/ZnO interface. This set of results implies that properties of the substrates are crucial in dictating the piezoelectric polarity of the RF-sputtered ZnO thin film, which can be explained from two aspects: heat is generated and transferred to the substrate during the sputtering process; positive charges are transferred from positive argon ions in the chamber atmosphere to the substrate through collision. Previous studies also suggested that thermal conductivity and electric conductivity of the underneath substrate material can affect the piezoelectric polarity of the as-grown film effectively. For the case of PET substrates, although a grounding electrode is used, it cannot dissipate heat and transfer electric charges efficiently due to the fact that the grounding electrode is only 5 nm thick and is isolated both thermally and electrically from the metal sample holder by the underneath 500-μm-thick PET substrate. Consequently, during the initial stage of ZnO film growth, heat and positive charges will accumulate on the substrate surface, both making adsorption of oxygen atoms more energetically favorable than that of zinc atoms. This initial stacking sequence dictates that c-axis of the as-grown film is pointing up from the interface. For the case of titanium foils, on the other hand, conductivities for heat and electricity are both much higher and the zinc atom layer with higher surface energy will hence tend to be adsorbed first while the oxygen atom layer with lower surface energy will tend to terminate the growth, leading to the reverse polarity orientation in which c-axis points down towards the interface. However, polarity control of the as-sputtered piezoelectric film is complex and non-trivial in the sense that it's not only influenced by substrate properties but also sputtering conditions and many other factors, which needs more in-depth investigations.

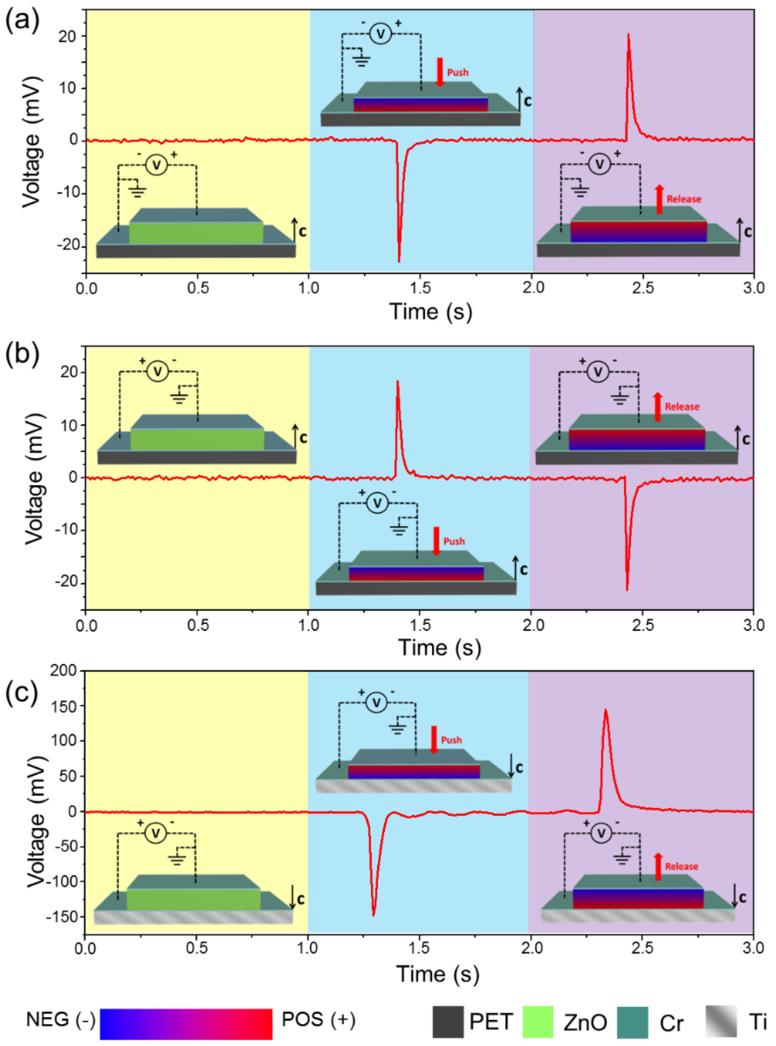

Figure 20: Piezoelectric tests were performed to determine the c-axis orientation of the ZnO piezoelectric thin film. The color gradient at the bottom represents the distribution of piezopotential. (a), (b) Test was performed on PET based samples with top electrode each connected to the positive pole of voltage pre-amplifier in (a) and negative pole of voltage pre-amplifier in (b). The sequence of electric pulses indicates that c-axis of the as-grown film is pointing up and away from the PET/ZnO interface. (c) Control test was performed by replacing the PET substrate with titanium foil and top electrode connected to the negative pole of voltage pre-amplifier. The sequence of electric pulses indicates that c-axis of the as-grown film is pointing down towards the Ti/ZnO interface, opposite to that grown on PET substrates.

Based on the above characterization results, the feasibility of as-grown ZnO film for piezotronic applications has also been investigated. ZnO piezoelectric thin film was directly grown onto PET substrates with identical process parameters. A pair of top electrodes was made subsequently by electron-beam evaporation, each with size of

$1 mm^2$ in the shape of square and separated from each other by 500 μm. In addition to the piezotronic effect, several other well-known mechanisms may also contribute to the observed conductivity change of the device. One is the geometrical effect which can be quantitatively expressed as $R = \rho l/A$, and change in material dimensions will lead to resistance change. The other is the piezoresistive effect that arises from change of inter-atomic spacing due to external strain, leading to change in bandgaps. It is worth noting that these two effects are both 'volume' effects and only depend on bulk properties of the semiconductor material while piezotronic effect modulates the material conductivity by affecting characteristics of metal-semiconductor interface.

In order to determine which mechanism dominates in the as-fabricated ZnO thin film device, a pair of Ti/Au (5 nm/25 nm) electrodes was deposited sequentially onto the first group of ZnO thin films in order to form Ohmic contacts with ZnO. Due to the high carrier density near junction interface associated with Ohmic contact, the effect of piezopotential can be significantly mitigated [20], while the contributions in conductivity change due to geometrical and piezoresistive effects should remain unaffected. I-V characteristics were subsequently obtained when the device was subject to different strains and the results shown in Figure 21 (a) indicate that for strain up to ±0.48%, both geometrical and piezoresistive effects have little influence on the device conductivity. The stress states introduced here in the film is different from the one used in the piezoelectric test, but both stress states will lead to strains in the overall effective polar direction of the ZnO thin film, which is perpendicular to the substrate. Strain values are estimated according to analytical solutions for elastic bending provided by previous studies [91], with tensile strain defined as positive and compressive strain defined as negative. The strain values used here are for longitudinal strains induced parallel to the substrate plane, which is for calibration purpose. The transverse strains in the films, which are along the overall effective polar direction of the ZnO thin film, can be estimated accordingly (using properties of film such as Poisson's ratio).

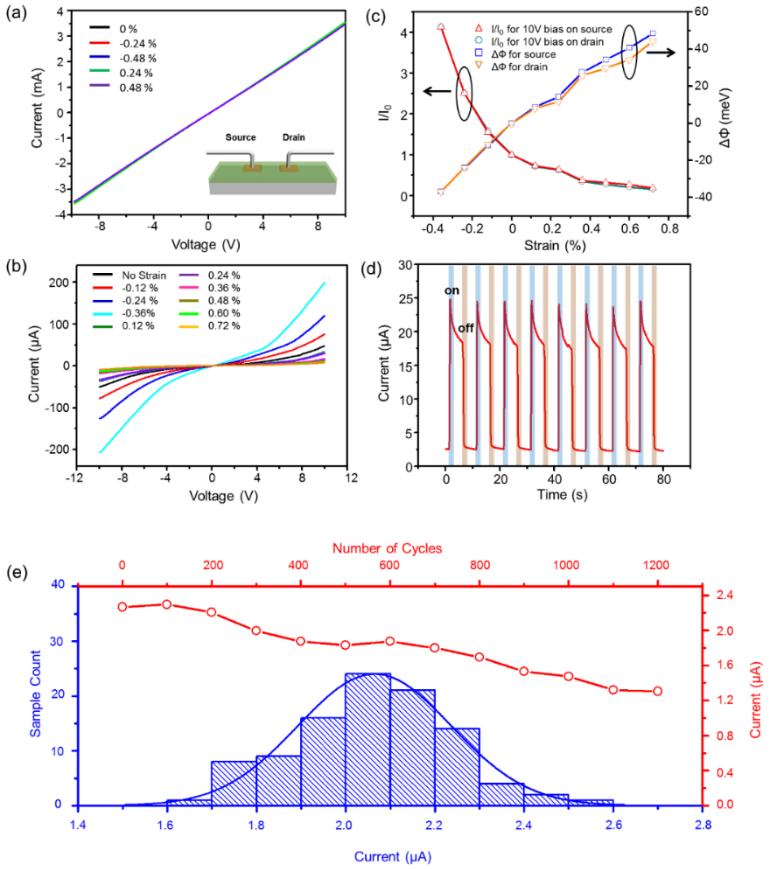

Figure 21: (a) I-V curves under different strain values were obtained from a device with Ohmic contact electrodes, indicating that both geometrical and piezoresistive effects have little influence on the device resistance for strains up to ±0.48%. The inset is a schematic of the device. (b) I-V curves under different strains were obtained from a device with Schottky contact electrodes, demonstrating modulation of charge carrier transport via piezotronic effect. (c) Calculated changes in current and SBHs explicitly demonstrate the “gating” effect of external strain on charge carrier transport in ZnO thin film piezotronic device. (d) Temporal-domain current response to applied periodic strains presents the feasibility for

electromechanical sensing applications with decent reliability. (e) Uniformity is demonstrated by collecting current values of 100 devices, shown in the blue histogram; fatigue behavior is investigated with cyclic bending test, shown in the red curve.

In the second group of devices, 30 nm Au was used instead as the electrodes (namely source and drain electrodes) to form Schottky contacts with ZnO, which was confirmed by the I-V curves shown in Figure 21 (b). When a compressive strain was applied, current flowing through the device increased; when a tensile strain was applied, current flowing through the device decreased. To explicitly demonstrate the “gating” effect of external strain on modulating the charge carrier transport in ZnO thin film piezotronic device, current values (I) in device under various strains were monitored at fixed bias. I_0 was the current flowing through the device when no strain was applied. As can be seen from the I/I_0-strain curve in Figure 21 (c), the currents in the device corresponding to each strain applied were similar when either the source or drain electrode was reversely biased (red triangles for 10 V bias on source and green circles for 10 V bias on drain). The slight difference observed might be caused by unintentionally introduced variations in the Schottky contacts at source and drain electrodes during fabrication.

The strain-induced change of Schottky barrier height (SBH) is also calculated and plotted in Figure 21 (c) by utilizing the thermionic emission-diffusion theory, presenting a change of 60 meV in SBH at both contacts when the change of applied strain was 1%. The temporal-domain current response to applied periodic strains is then shown in Figure 21 (d), demonstrating the feasibility of utilizing ZnO thin film piezotronic devices as electromechanical sensors with decent reliability. To further characterize uniformity and reliability of our devices' operation, 100 of such devices are fabricated and their current values at 2 V bias and zero strain are collected. As summarized in Figure 21 (e) (histogram in blue), 85% of the devices have current values within the range of 2 ± 0.2 μA, with the mean value of 2.065 μA and standard deviation of 0.172 μA. It is worth noting that under 2 V bias, the current flowing through our device is increased by ~14 μA under a compressive strain of -0.36% and decreased by ~1.8 μA under a tensile strain of 0.72%, both significantly larger than the standard deviation observed. This suggests the good uniformity and reliable operation of our thin-film based piezotronic devices. Cyclic bending test is also performed to investigate the fatigue behavior of our devices. A relatively large compressive strain of -2.5% (corresponding to a bending radius of 1.5 cm) is periodically applied onto the device to accelerate the aging process and the current values under 2 V are recorded per 100 bending cycles. From the results shown in Figure 21 (e) (red curve), it can be seen that the initial current value is 2.26 μA and then gradually drops to 1.31 μA after 1200 bending cycles. This level of current decrease from fatigue is also much smaller than the variations induced by piezotronic effect, indicating stability and reliability in operation of our devices even under cyclic bending with large magnitude of induced strain.

The band diagrams of ZnO thin film piezotronic devices are illustrated in Figure 22 to better demonstrate the underlying working mechanism. Figure 22 (a) shows the Schottky barriers formed at both contacts with similar barrier heights. When the device is connected to an external power source, the quasi-Fermi level of one electrode is raised (source side here), giving rise to the band diagram shown in Figure 22 (b), which, however, does not affect the barrier heights from the metal sides on both electrodes. When a tensile strain is applied to the device, negative piezoelectric polarization charges are induced at the top surface of ZnO film. These immobile ionic charges deplete free electrons near the metal-semiconductor interface and therefore increase the SBHs at both contacts, as shown in Figure 22 (c). When a compressive strain is applied to the device, on the other hand, positive piezoelectric polarization charges are induced near the top surface of the ZnO film, attracting free electrons towards the metal-semiconductor interface and therefore decreasing the SBHs at both contacts, as shown in Figure 22 (d). The conductivity of the entire thin film device is dictated by the reversely biased contact and the effective conductivity of the device is sensitive to the change in SBH at that specific contact. Different from piezotronic devices based on 1D nanomaterials in which metal-semiconductor contacts are formed at the two opposite polar surfaces, both source and drain electrodes in the ZnO thin film piezotronic devices are in contact with the same surface of as-deposited ZnO film, and hence piezoelectric polarization charges with same polarity will be induced at both Schottky contacts when external strain is applied. This leads to the observed I-V curves (Figure 21 (b)) in which same tuning trend of applied strain can be observed when either source or drain side is reversely biased. As pointed out earlier, this helps circumvent the difficult and elusive predetermination of c-axis orientation for 1D nanostructures and brings significant simplification and convenience for further construction of integrated devices / systems.

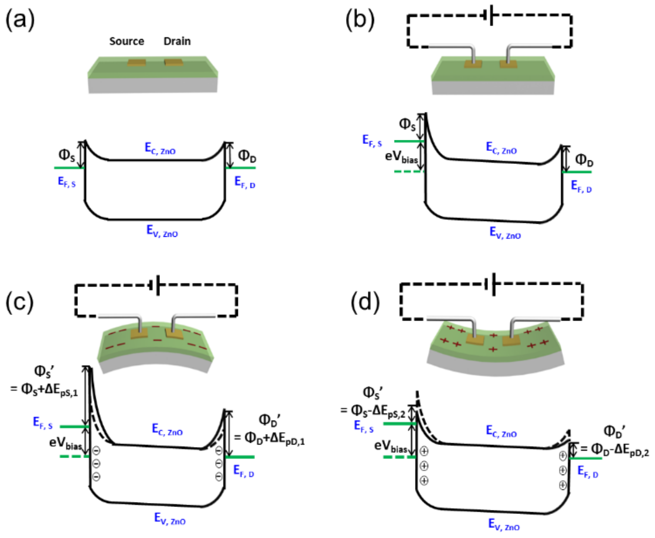

Figure 22: Band diagrams of ZnO thin film piezotronic devices, illustrating the underlying working mechanism. (a) Schottky barriers form at both contacts with similar barrier heights. (b) The quasi-Fermi level of one electrode is raised (source side here) when the device is connected to an external power source. (c) When tensile strain is applied to the device, negative piezoelectric polarization charges are induced at the top surface of ZnO film, depleting free electrons near the metal-semiconductor interface and increasing the SBHs at both contacts. (d) When compressive strain is applied to the device, positive piezoelectric polarization charges are induced at the top surface of ZnO film, attracting free electrons towards the metal-semiconductor interface and decreasing the SBHs at both contacts.

In conclusion, flexible piezotronic device based on RF-sputtered piezoelectric semiconductor thin films has been investigated for the first time. The dominating role of piezotronic effect over geometrical and piezoresistive effect in the as-fabricated devices has been confirmed and the modulation effect of piezopotential on charge carrier transport under different strains is subsequently studied. It is prospected that piezoelectric semiconductor thin films can be an excellent alternative to their 1D counterpart for realizing piezotronic applications due to the technological compatibility with state-of-art microfabrication technology. Results demonstrated here broaden the scope of piezotronics and extend its potential applications in the fields of sensors, flexible electronics, flexible optoelectronics, smart MEMS/NEMS and human-machine interfacing.

4.3 Summary

In summary, the motivation of my PhD research is to further develop the field of piezotronics beyond single NW based devices. The above works discussed in this chapter have made meaningful steps towards achieving this goal. Specifically, the first work addressed the problem by utilizing pixel addressable ZnO NWs array and achieved a large scale integration of tactile sensors at a very high resolution. The second work addressed the problem by utilizing RF sputtered ZnO thin film and demonstrated the piezotronic effect based on a widely used thin film deposition technology in the industry. It is expected that by going down these two routes, we can multi-functionalize piezotronic devices as well as expedite the progress of commercialization of this young technology.

5. Piezophototronic effect

Coupling of different conventional fields is a typical pattern of how science and technology is progressed based on existing understandings of physical laws and processes. The field of piezotronics is a representative example of innovation on strain sensing mechanisms by coupling the field of piezoelectricity and electronics. An even more convincing example is the field of optoelectronics, namely the coupling between optics and electronics, which has brought dramatic change to areas of lighting, energy harvesting, sensing etc. The idea of linking piezoelectricity, electronics and optics all together is exciting and might even be revolutionary. This three way coupling has been named as the piezophototronic effect by pioneers of this field and many significant progress has been achieved [21, 92-96]. However, one problem that remained in this research area was the same as that of piezotronics mentioned in the previous chapter. Most of the works were done based on single NW architectures. Under this context, I also tried to address this issue in my PhD research by scaling up the architecture from single NW based devices to NWs array as well as thin film based devices to overcome the limitations and contribute to elevating the research area from the device level to the system level. In the following, works studying the performance improvement of photodetectors and solar cells by the piezophototronic effect based on ZnO NWs array and thin film materials will be elaborated.

5.1 Enhanced UV detection sensitivity of ZnO thin film photodetectors by the piezophototronic effect[86]

A ZnO thin film / gold system can be used for UV detection thanks to both the strong UV absorption of the ZnO material as well as the electron-hole pair separation mechanism enabled by the Schottky junction at the ZnO / Au interface. The device fabrication is exactly the same as discussed in “4.2 Piezotronic Effect in Flexible Thin-film Based Devices”. A 365-nm UV lamp was used as the light source. During the experiments, the UV light was turned on for 1 s and then switched off, while the temporal response of current from the device was monitored under the bias of 5 V. In Figure 23 (a), the black curve was recorded when no strain was applied to the device, showing a sensitivity (defined as the percentage increase of current values) of 25% and a reset time of ~880 s. When 0.24% tensile strain was applied, an apparent enhancement of sensitivity was observed, from 25% to 89.25% with a shorter reset time of 582 s, as shown by the blue curve. When the applied tensile strain was increased to 0.48% (the red curve), the UV sensitivity further increased to as high as 112.5% with an even shorter reset time of 337 s. The cases for device under compressive strains are also obtained and plotted in Figure 23 (b) for comparison. When -0.24% compressive strain was applied, the device sensitivity decreased from 25% to 13.21% (green line). As the applied compressive strain was increased to -0.48%, as shown by the orange curve, the sensitivity further decreased to 12.9%. The corresponding reset time increased to over half an hour for both cases. The tuning effect of strain on device's UV sensitivity is summarized in Figure 23 (c) and a significant enhancement of sensitivity by applying tensile strain can be observed.

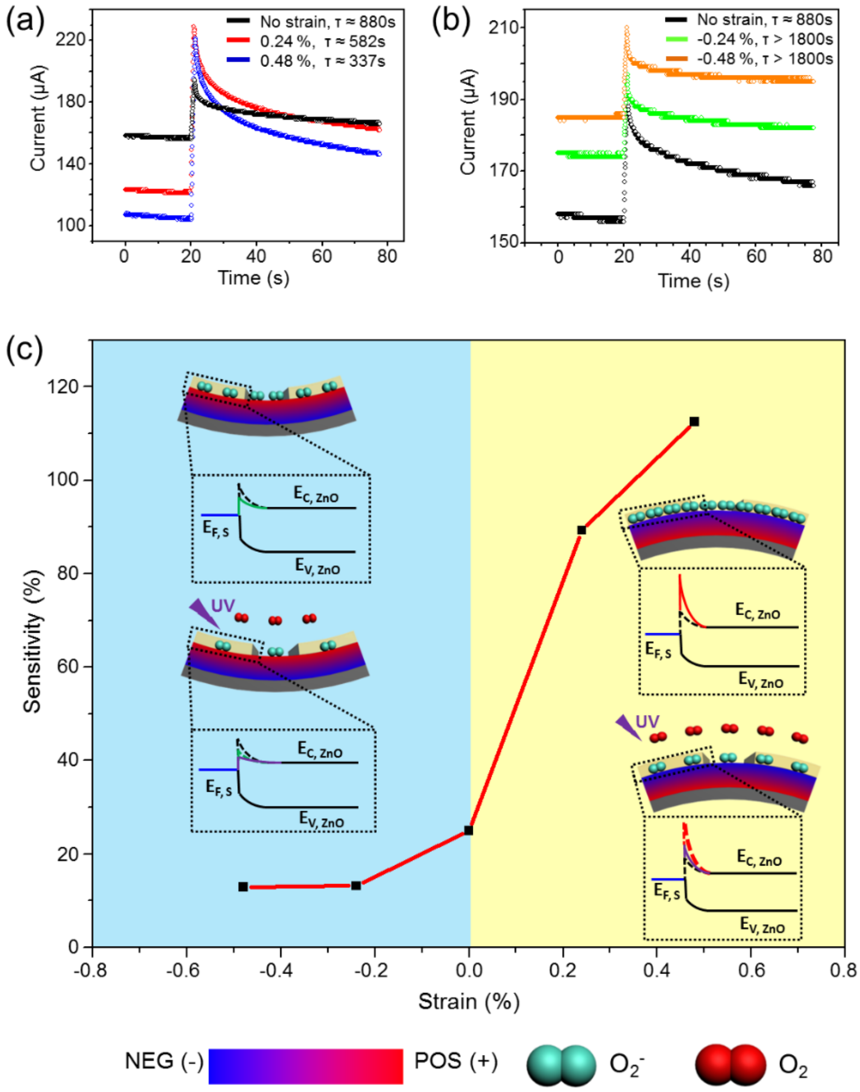

Figure 23: ZnO piezotronic thin film based UV sensor with tunable sensing capability. The color gradient at the bottom represents the strain induced piezopotential. (a) Tensile strains are applied to the device which increases the UV sensitivity and decreases the reset time. (b) Compressive strains are applied to the device which decreases the UV sensitivity and increases the reset time. (c) Sensitivity of the UV sensor under different strain values. The insets explain the underlying mechanism of the strain tuning effect.

In addition to the direct contribution from photon-generated excess carriers, ZnO has another important mechanism [97, 98] that contributes to its UV sensing capability. In dark environment, oxygen can be adsorbed onto ZnO surface through the reaction [O^2 + e^- --> O^{2-}]. Since free electrons are consumed by this adsorption, a depletion layer is consequently created that decreases the conductivity near the film surface. Upon UV illumination, excess electron-hole pairs will be generated and the generated holes can discharge the adsorbed oxygen ions, leading to the increase of surface conductivity. Meanwhile, with the accumulation of excess electrons, oxygen will be re-adsorbed and finally a new equilibrium is reached. When the illumination is turned off, electrons and holes will start to recombine with each other. This recombination process can, however, be very slow due to the hole trapping effects at the surface, mitigating the re-adsorption of oxygen, which explains the long reset time normally observed in ZnO based UV sensors [97]. The above mechanism applies to the situation where bare ZnO is exposed to UV light. For our device, in addition to the above processes, the Schottky barriers formed between Au electrodes and ZnO also come into play by introducing a strong local electric field across the interface. Immediately after electron-hole pairs are generated upon UV illumination, they will be effectively separated by this local electric field, which reduces the recombination rate and increases the carrier lifetime and density. As a result, oxygen can be discharged and desorbed at a faster rate. Meanwhile, the SBH is decreased due to illumination so that more charge carriers can transport through the barrier region. These factors all lead to the enhanced sensitivity observed for Schottky-contact based ZnO UV sensors. When UV illumination is turned off, this local electric field can quickly restore the carrier distribution to its original status, overcoming the trapping effect, and hence lead to a shorter reset time.

When strain is introduced into the system, the induced piezoelectric polarization charges can also effectively modulate the above processes, as shown by the schematics and band diagrams in Figure 23 (c). When tensile strain is applied (region in light yellow), negative polarization charges are induced at the top surface, promoting the oxygen adsorption/re-adsorption process, which contributes to the observed increased UV sensitivity and decreased reset time. Moreover, the induced negative piezopotential will raise the SBHs on both electrodes, resulting in further improvement to the UV sensing performance. On the other hand, when compressive strain is applied (region in light blue), the induced positive polarization charges at the surface will partially deplete the free electrons in the surface region, mitigating the oxygen adsorption/re-adsorption process, and hence decrease the UV sensitivity and increase the reset time. The positive ionic polarization charges at the semiconductor-metal interface can also lower the SBHs and further degrade the UV sensing performance.

In short, the above work demonstrates the piezophototronic effect based on ZnO thin film materials which can effectively tune the performance of a Schottky junction photo detector.

5.2 Performance optimization of silicon-based p–n junction photodetectors by the piezophototronic effect [99]

This work also studies the modulation of PD performance by the piezophototronic effect. There are, however, several distinct differences when compared with the above. Firstly, ZnO NWs array are used as the n-type layer, instead of thin films; secondly, the PD is p-n junction (p-Si / n-ZnO) based instead of Schottky junction based; thirdly, the detection of visible light is studied here instead of UV light, which means that the ZnO material acts as a window layer and an antireflection layer and the excitation of electron-hole pairs happen on the silicon side.

The structure of an as-fabricated p–n junction PD is schematically illustrated in Figure 24 (a). A piece of boron doped p-type silicon with resistivity 1-30 Ωcm is used as the substrate as well as the p-type semiconductor. Surface modification was performed by etching the silicon in KOH solution to produce micro-pyramid structures with an average size of 2–4 μm (Figure 24 (b)). A 100nm ZnO seed layer was subsequently sputtered to cover the micro-pyramid structure and ZnO NWs array was synthesized on top to form the p-Si / n-ZnO heterostructures, as shown in Figure 24 (c). Ag nanowires were dispersed on the ZnO NWs array as shown in Figure 24 (d), in order to increase the conductivity of the top electrode. Finally, the ITO layer and copper were respectively sputtered on the ZnO NW array and the p-type Si to serve as the top and bottom electrode.

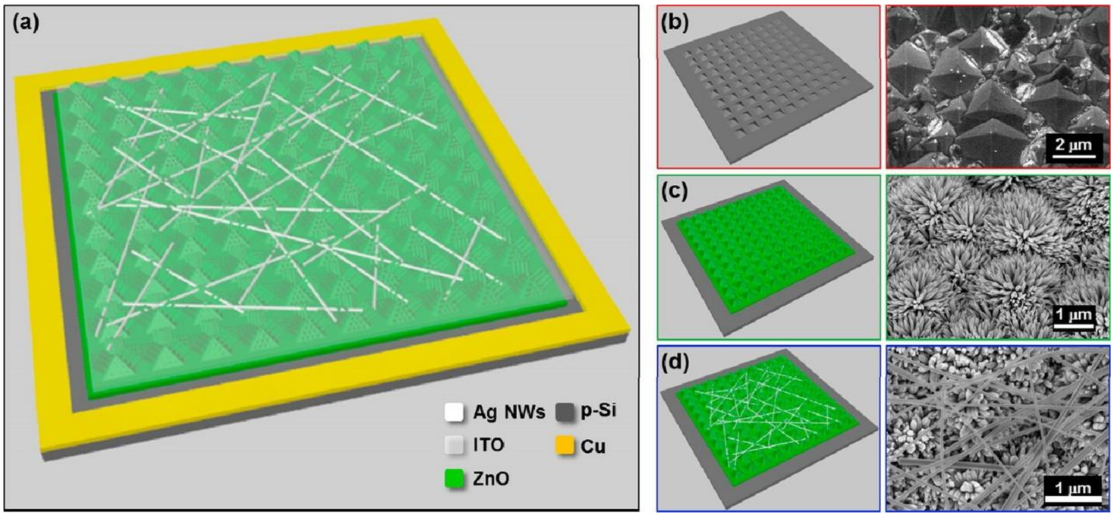

Figure 24: Device fabrication. (a) Schematic structure of a p-Si/n-ZnO NW hybridized PD. (b–d) Schematic structure (left panel) and SEM images (right panel) of (b) etched Si wafer and p-Si/n-ZnO heterojunctions (c) before and (d) after spin coating Ag NWs.

The I-V-strain characteristics of the PDs were firstly measured in dark environment. Strain was applied onto the PD from the ITO/ZnO side by using a linear stage. A Kapton/PDMS cushion was used so that the displacement from the linear stage is large enough to be accurately read. By using the Young's modulus value of the PDMS and the ZnO, strain applied on the ZnO NWs array could be estimated. Accordingly, the result of the I-V-strain characteristics was plotted in Figure 25 (a) with tensile strain being defined as positive and compressive strains as negative. As we can see, the forward bias current obviously increases with higher strain applied. The inset of Figure 25 (a) plots the output current of the cell against the applied strain under a bias voltage of 2 V. This indicates that the rectification of the p-Si/n-ZnO heterojunction can be enhanced by applying compressive strain.

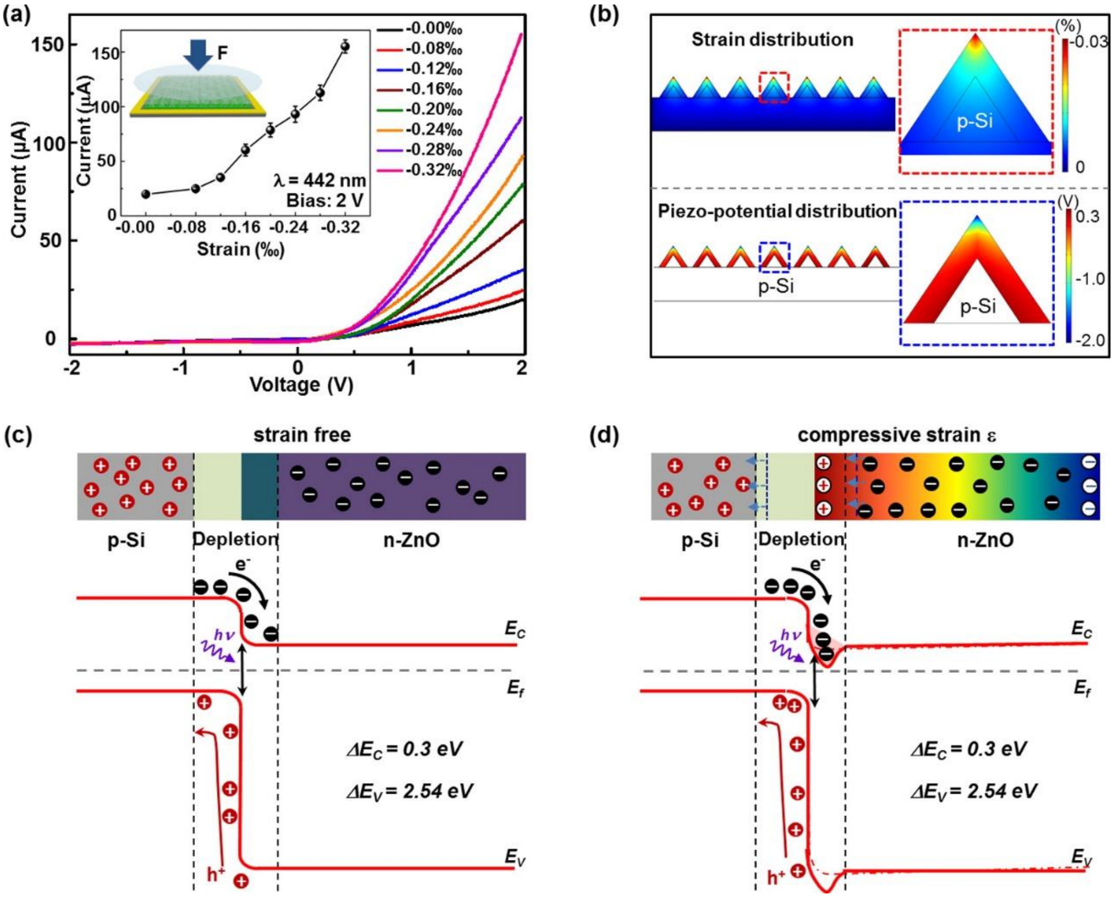

Figure 25: Working mechanism. (a) I–V characteristics of the device under different strain conditions without laser illumination. The inset shows the current changes with the external strains when a 2 V bias is applied. (b) Simulation results of strain distribution (top panel) and piezoelectric potential distribution (bottom panel) in the ZnO nanowire array by FEA. (c, d) Schematic band diagrams of a p-Si/n-ZnO heterojunction (c) without and (d) with compressive strain applied to illustrate the working mechanism of piezo-phototronic effect optimized p–n junction PDs.

A finite element analysis based on the 2D physical model was conducted to simulate the strain/piezoelectric potential distributions in ZnO NW arrays, as shown in Figure 25 (b). A pressing force of 10 N was used and the simulation results indicate that the compressive strain concentrates in the ZnO NWs located around the tips of the micro-pyramids (top panel in Figure 25 (b)). The corresponding piezo-potential distributions were also illustrated in Figure 25 (b) (bottom panel), by setting the c-axis of the NWs array as pointing upward. (11) The influence of the compressive strain induced positive potential on the photo detection process at the p-Si/n-ZnO interface can be explained by the expansion of the depletion width on the p-Si side[100] and the modification of the band diagram[101] (Figure 25 (c), (d)). The band gap and electron affinity values for Si and ZnO are $E_{g,Si}$ = 1.12 eV, χ_{Si} = 4.05 eV and $E_{g,ZnO}$ = 3.36 eV, χ_{ZnO} = 4.35 eV respectively. Accordingly, a conductive band offset of ΔE_c = 0.3 eV and a valence band offset of ΔE_v = 2.54 eV [102] will be present when the heterogeneous junction is formed, as shown in Figure 25 (c). Upon visible light illumination, photons with a uniform wavelength of 442 nm pass through the n-ZnO window layer and are mostly absorbed by the p-Si, leading to the generation of electron–hole pairs and thus increasing the current level. When compressive strain is applied, the positive piezo-polarization charges induced at the junction interface shifts the depletion region towards the p-Si side. Since electron-hole pairs are mostly generated in the Si, the effective expansion of the depletion region on p-type side increases the photon absorption volume and thus more free carriers can be generated. Nevertheless, the positive piezo-charges may also act as electron traps that hinder the transport of photogenerated electrons towards the n-ZnO side. On the band diagram, this effect can be understood as creating a dip in the band profile, as shown in Figure 25 (d). Two effects from the positive piezo-charges at the interface compete with each other and for a broad range of strain applied onto the piezoelectric ZnO, we may expect to see an optimal strain level at which the performance of the PD is the best. The above is the qualitative understanding of the piezophototronic effect that we introduce to the PD system.

The strain-free performance of the PDs was firstly investigated and the results are summarized in Figure 26. To study the transmittance of the ZnO NWs array and the silver NWs, the opaque silicon substrate was replaced by a transparent glass substrate while the synthesis and fabrication methods were maintained. The transmission spectra of the ZnO NWs is shown in Figure 26 (b), indicated by the black solid line and the transmission spectra of the ZnO NWs plus silver NWs is shown in Figure 26 (b), indicated by the purple dashed line. We can see that the transmittance for both cases are larger than 90% at the wavelength of 442 nm, which indicates that the photogeneration process majorly happens on the p-Si side. Figure 26 (c) shows the response of the PD under 442 laser illumination with nine different power densities ranging from 0 to 1.3×10^{-4} W/cm^2, when a 2 V voltage was applied as the bias. The output current increased from 20.5 μA (dark current) to up to 81.5 μA (1.3×10^{-4} W/cm^2). The inset plots the output current vs power density which clearly shows a near linear dependency. The I-V characteristics of the PD under these nine different illumination power were also measured, as shown in Figure 26 (d) together with a photograph of the real device shown in the inset.

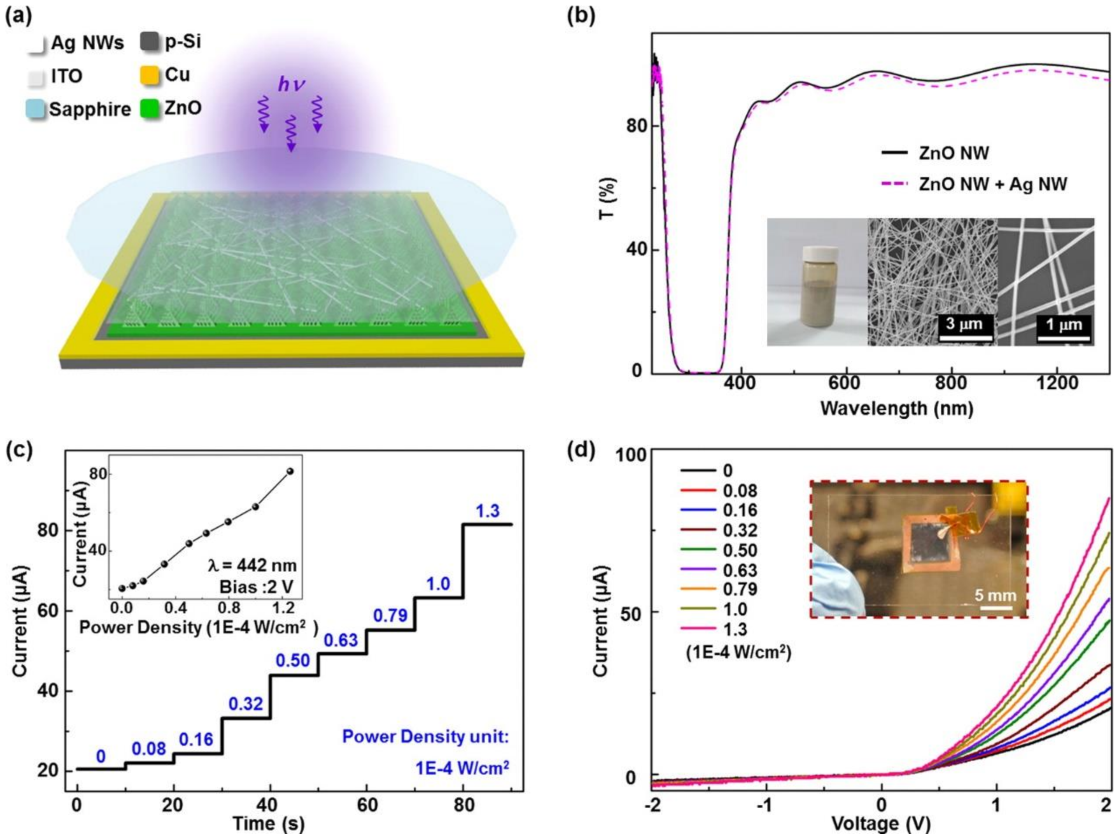

Figure 26: General photoresponse of p-Si/n-ZnO NWs hybridized PDs. (a) Schematic illustration of the experimental setup. (b) Transmission spectra of a ZnO NWs array on the glass (black solid line) and the ZnO NWs coated with Ag NWs (purple dashed line). The insets are a photograph and SEM images of Ag NWs. (c) *I*–*t* response of the device under different illumination power densities at 2 V bias voltage. The inset shows the current change with the power density. (d) *I*–*V* characteristics of the device under different illumination power densities when a triangle wave is applied. The inset shows a photograph of the real device.

Strain is then introduced into the system to study the piezophototronic effect on the PD's performances. Firstly, under the same setup that was used to obtain Figure 26 (c), 11 different strains ranging from -0.00 ‰ to -0.40 ‰ were further applied and the results are summarized in Figure 27 (a). Under each power density (from 3.2×10^{-5} to 1.3×10^{-4} W/cm^2), 11 different strains ranging from −0.00‰ to −0.40‰ were applied onto the PD while its optoelectronic behavior was measured, indicating an obvious increase in output currents as a result of either increasing the illumination intensity or applying compressive strain or both. The photocurrent $\Delta I = I - I_{dark,s}$ ($I_{dark,s}$ represents the dark current under certain strains) is further shown in Figure 27 (b) to illustrate the effect of applied strain and illumination intensity on the performance of the PD. From this figure, we can see that a local maximum of the photocurrent ΔI is obtained at −0.10‰ compressive strain under these different illumination intensities. Relative sensitivity $\Delta I/I_{dark,s}$ is calculated and shown in Figure 27 (c). Due to the fact that compressive strain also increases dark current, the highest photocurrent percentage change is obtained at −0.10‰ for the power densities ranging from 0.08 to 0.5 ($\times 10^{-4}$ W/cm^2) but for the power densities from 0.63 to 1.3 ($\times 10^{-4}$ W/cm^2), the highest photocurrent percentage change is achieved at the strain-free state. To fairly compare the performance of the photodetector under different illumination power densities, the photoresponsivity R was also calculated based on:

$$\mathrm{R} = \frac{I_{light,s} - I_{dark,s}}{P_{ill}} = \frac{\eta_{ext} q}{h\nu} \Gamma_G$$

, where $P_{ill} = I_{ill} \times S$ is the illumination power on the PD; $I_{light,s}$ and $I_{dark,s}$ represent the photon and dark current under the corresponding external strain, respectively; Γ_G is the internal gain; η_{ext} is the external quantum efficiency (EQE); q is the electronic charge; h is Planck's constant; v is the frequency of the light; I_{ill} is the excitation power density; S is the effective area of the PD. From the results shown in Figure 27 (c), we can see that the R for these different illumination intensities are all optimized at the strain of -0.1‰, with the highest value of 7.1 A/W at a power density of 3.2×10^{-5} W/cm^2, corresponding to a relative enhancement of 177%. The R value achieved here is much larger than that of a typical commercial Si photodiode PD (in the range 0.1–0.2 A/W at 442 nm) [103].

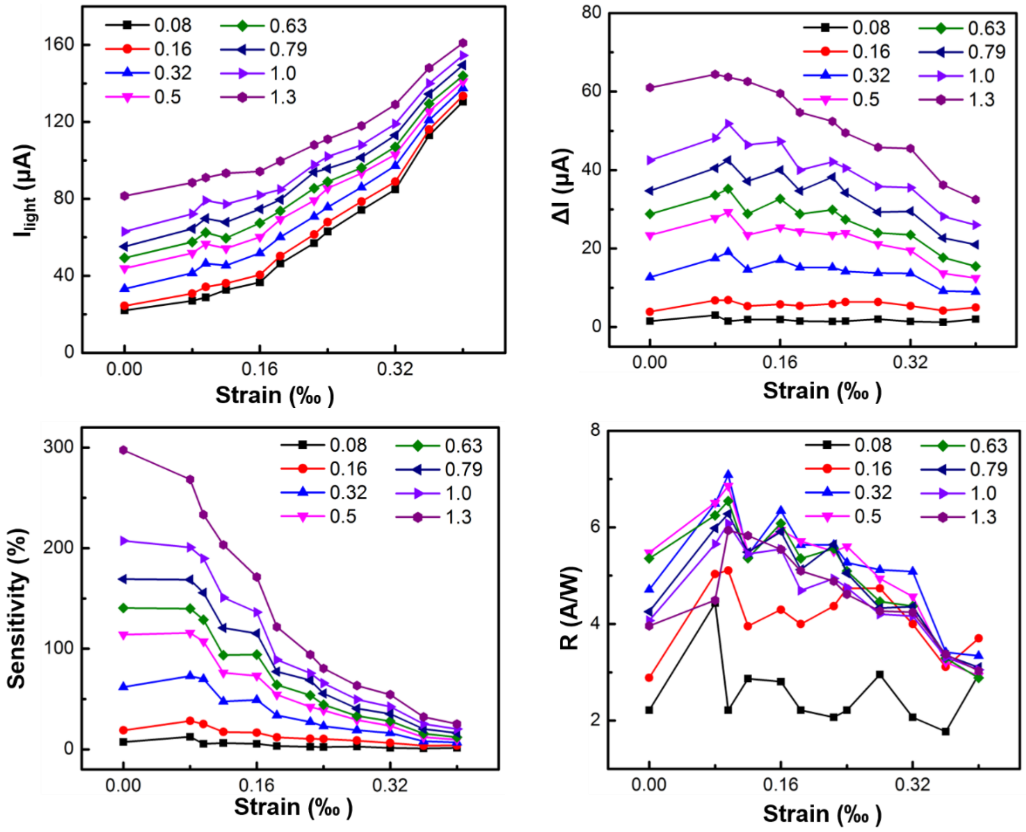

Figure 27: Piezo-phototronic effect. (a) Output current of the PDs under different strain and illumination conditions at 2 V bias voltage. The inset shows a schematic illustration of the experimental setup. (b) Photocurrent, (c) relative sensitivity of the device under different strain and illumination conditions, biased at 2 V.

The photodetection repeatability of the p-Si/n-ZnO NW PDs under a bias of 2 V and zero strain is presented in Figure 28 (a) by switching the 442 nm laser source on and off for six cycles with the illumination density at 8.0×10^{-6}, 3.2×10^{-5}, and 6.3×10^{-5} W/cm^2 respectively. Rise and fall response time of the PD under different illumination intensities was further analyzed, as shown in Figure 28 (b) where the weight-averaged response time was calculated by fitting the experimental curve with double-exponential functions [97, 104]. A fall time of the PD approximated at 57 ms and a rise time ranging from 110 to 229 ms were obtained. A similar measurement is carried out by fixing the illumination power at 6.3 $\times 10^{-5}$ W/cm^2 and applying different strains to the device. Figure 28 (c) demonstrates the repeatability of the photodetection while Figure 28 (d) shows the rise and fall time of the PD. Weight-averaged rise time and fall time were calculated and are shown in Figure 28 (d) under different external strains. No significant changes for the fall time could be observed under different straining levels but a minimum value of 101 ms was observed for the rise time at an external strain of −0.10‰, corresponding to a relative change of 87%.

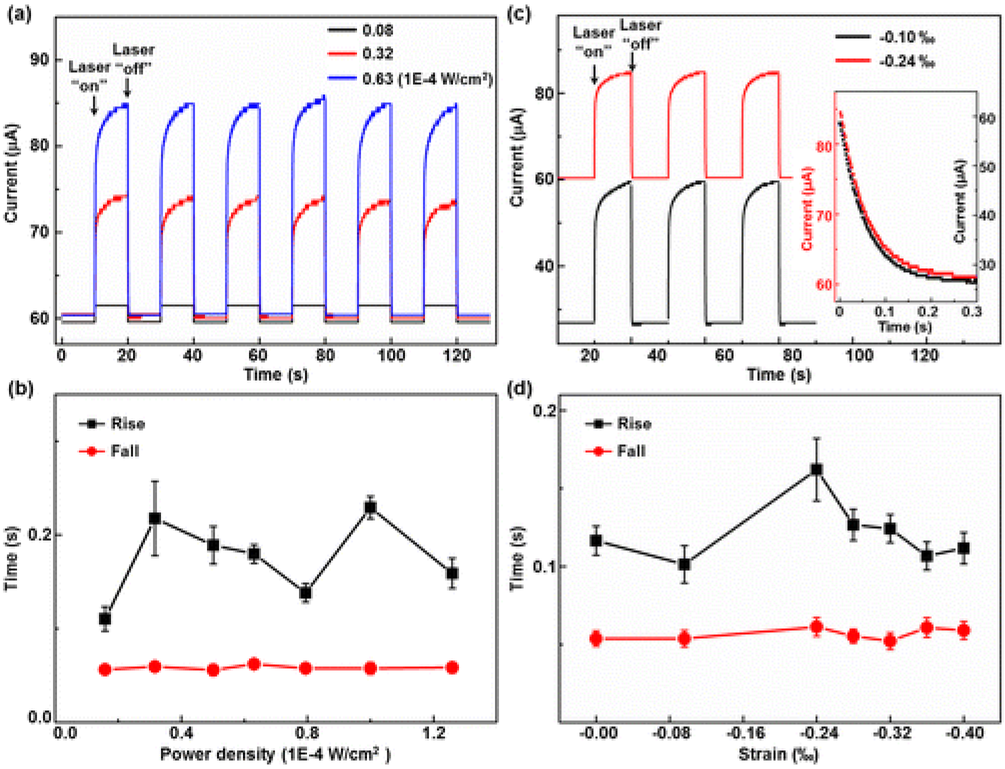

Figure 28: Repeatability and time response of the PDs. (a) Repeatability and time response and (b) the corresponding rise and fall time of the device under different illumination power densities, under −0.24‰ external strains. (c) Repeatability and time response and (d) the corresponding rise and fall time of the device under different compressive strains, under a power density of 6.3 $\times 10^{-5}$ W/cm^2.

In summary, the effect of piezophototronics on the p-Si/n-ZnO heterojunction photodetection system was studied. Visible light of 442 nm was used as the light source and the photodetection performance of the PD was successfully modulated and optimized by the piezophototronic effect. A maximum photoresponsivity *R* of 7.1 A/W and a shortest rising time of 101 ms were obtained from these PDs when a compressive strain of −0.10‰ was applied onto the ZnO NWs array of the PD, corresponding to a relative enhancement of 177% in *R* and shortening of 87% in response time, respectively. This work provides a potential approach to enhance / optimize the performances of silicon-based optoelectronic devices by the piezo-phototronic effect.

5.3 Effective piezophototronic enhancement of solar cell performance by tuning material properties [105]

The above works have studied the performance enhancement and optimization of Schottky junction and heterogeneous p-n junction photodetectors by the piezophototronic effect, based on both ZnO NWs array and thin film materials. Here, we further study the case of P3HT / ZnO based thin film solar cells and demonstrate the benefits brought by the piezophototronic effect towards the field of solar energy harvesting.

The structure of the solar cell is shown in Figure 29 (a). 100 nm of ITO is firstly deposited onto transparent and flexible PET substrate as the top electrode. 600 nm of ZnO is subsequently deposited by RF sputterring, leaving out the margins for later electric connection. The sputtering parameters vary for different groups of samples according to the needs of our study but the common parameters are an RF power of 120

W and a total pressure of 6 mTorr during the deposition. Electronic grade P3HT was purchased from Sigma-Aldrich and dissolved into chlorobenzene at a concentration of 10 mg/ml without further purification. Then the solution is spin-coated onto the ZnO layer at a speed of 700 rpm for 30 s to form the p-type layer. Drying is subsequently performed at 120 ℃ for 5 min under nitrogen environment to improve the electrical and contact properties. Lastly, a 100 nm gold layer is deposited onto P3HT as the bottom electrode.

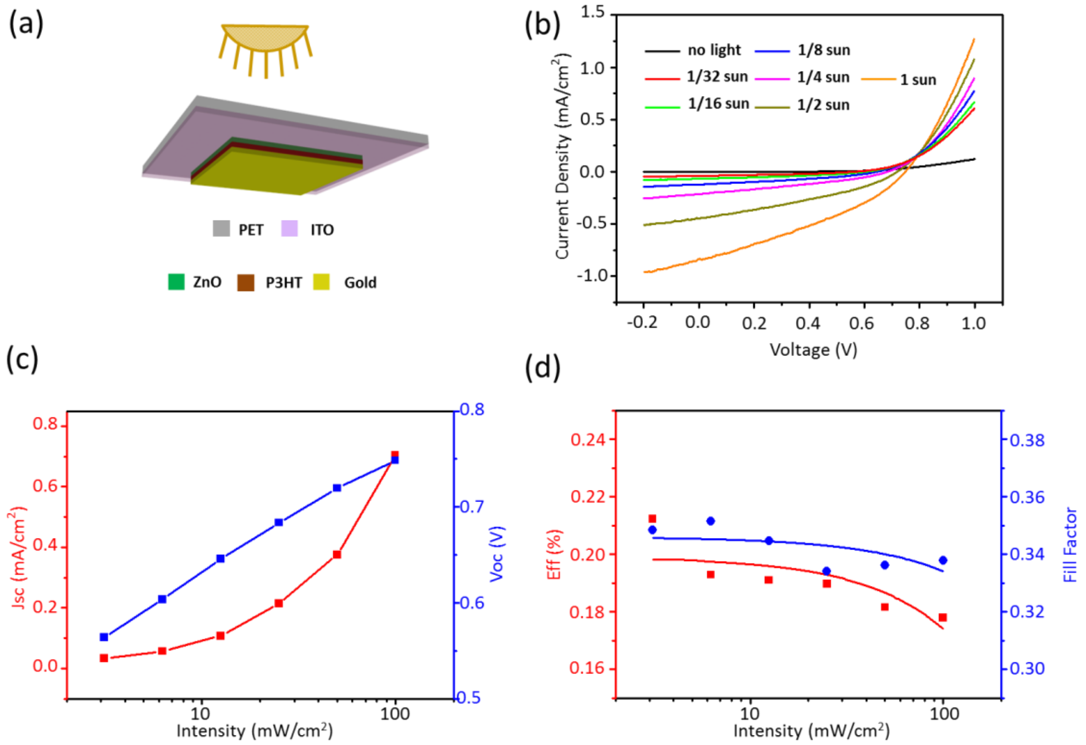

Figure 29: General performance of strain-free ZnO / P3HT solar cell (Group 1) is shown in this figure. (a) Schematic of the solar cell structure. (b) *J*–*V* characteristics of the solar cell under different illumination intensities, from one full sun (100 mW/cm^2) to as low as 1/32 sun (3.125 mW/cm^2). (c) J_{SC} and V_{OC} of the solar cell under different illumination intensities. X-axis values are expressed in log 10 scale. (d) Efficiency and fill factor under different illumination intensities. Data points are linearly fitted. X-axis values are expressed in log 10 scale.

A solar simulator (Model 91160, Newport, 300 W, AM 1.5) is used to provide illumination to the solar cells with its output power adjusted to 100 mW/cm^2, which is considered the intensity of one sun under normal conditions. A set of sunlight attenuators is used to achieve different levels of illumination intensity. The first solar cell sample under test is labeled as Group 1, of which the ZnO layer is sputtered at room temperature (without purposefully heating the substrate during sputtering) with Ar flow rate at 30 sccm and O_2 flow rate at 10 sccm. As-measured J–V characteristics of the solar cell under 6 different illumination intensities are shown in Figure 29 (b). At 100 mW/cm^2, the solar cell yields an open-circuit voltage (V_{OC}) of 0.7487 V, a short-circuit current density (J_{SC}) of 0.7036 mA/cm^2, a fill factor of 0.3378 and an efficiency of 0.178%. When the illumination intensity is decreased to 3.125 mW/cm^2, the solar cell yields a V_{OC} of 0.5641 V, a J_{SC} of 0.0336 mA/cm^2, a fill factor of 0.3484 and an efficiency of 0.212%. The values of V_{OC} and J_{SC} under different intensities are summarized in Figure 29 (c) and the values of efficiency and fill factor under different intensities are summarized in Figure 29 (d), indicating that the efficiency of the solar cell increases with lowering illumination intensities. This phenomenon could be explained by its limited charge separation ability meaning that under a higher generation rate, the proportion of electron–hole pairs that can be separated by the junction region is lower. In the following, the method to improve this ability will be demonstrated and discussed.

The performance of Group 1 solar cell under strains at the illumination intensity of 25 mW/cm^2 (the rest of the measurements will all be done at this intensity) is subsequently tested. Before strain is loaded, the solar cell yields a J_{SC} of 0.2150 mA/cm^2, a V_{OC} of 0.6823 V and an efficiency of 0.188%. After strain is applied (method shown in the inset of Figure 30 (a)), we observe increases in J_{SC} under tensile strain and decreases in J_{SC} under compressive strain (tensile strain is defined as positive and compressive strain is defined as negative) but the V_{OC} almost remains unaffected, as is shown in the J–V characteristics in Figure 30 (a). Specifically, the J_{SC} experiences a 2.568% increase to 0.2205 mA/cm^2 under 0.32% tensile strain and a 4.940% decrease to 0.2042 mA/cm^2 under 0.32% compressive strain. Accordingly, the efficiency is increased by 3.456% to 0.194% under 0.32% tensile strain and is decreased by 2.432% to 0.183% under 0.32% compressive strain (relevant data will be summarized in Figure 33). Since RF-sputtered ZnO film is self-textured [86, 106, 107], the asymmetry of performance change by loading opposite signs of strain clearly suggests that piezoelectricity plays a role in the process. A model is presented in Figure 30 (b) to explain the performance change. The band structure for the strain free condition is shown in Figure 30 (b1). The basic processes for a solar cell to work are the generation of electron–hole pairs, separation of electron–hole pairs and recombination of those carriers in external circuits. The step of critical importance here is the electron–hole pair separation. For J_{SC}, its value is directly related to the carrier collection probability. Qualitatively, a stronger built-in field in the junction region means a higher collection probability for the carriers and vice versa. When external strain is applied to the ZnO thin film, creating negative polarization charges at the ZnO / P3HT interface, both the conduction and valence bands in the junction region will be lifted up, weakening the strength of the built-in field. This could also be interpreted as the contraction of the depletion region on the P3HT side where most of the photogeneration happens. This leads to the decrease of J_{SC}. On the contrary, positive polarization charges created at the interface will lower the conduction and valence bands in the junction region, strengthening the built-in field. Similarly, we can understand this as an expansion of the depletion region on the P3HT, which leads to the increase of J_{SC}. As for the V_{OC}, its value is determined by the difference between quasi-Fermi levels of the p-type and n-type semiconductor, which is largely decided by the illumination intensity. Quantitatively, $V_{OC} \approx (nkT/q)ln(J_{SC}/J_0)$ (n is the ideality factor, kT/q is the thermal voltage and J_0 is the dark reverse saturated current), which means the change in J_{SC} does affect the value of V_{OC}. However, since $d(V_{OC}) \approx (nkTJ_O/q)(d(J_{SC})/J_{SC})$, (the value of nkT/q is on the order of 30 mV and the value of J_{SC}/J_0 is ~250 according to Figure 29 (b)), 1 mA/cm^2 change in J_{SC} only leads to approximately 1.2×10^{-4} V variation in V_{OC} and can thus be considered negligible. This explains why on the J–V characteristic of Figure 30(a), the voltage stays mostly unaffected by the strains.

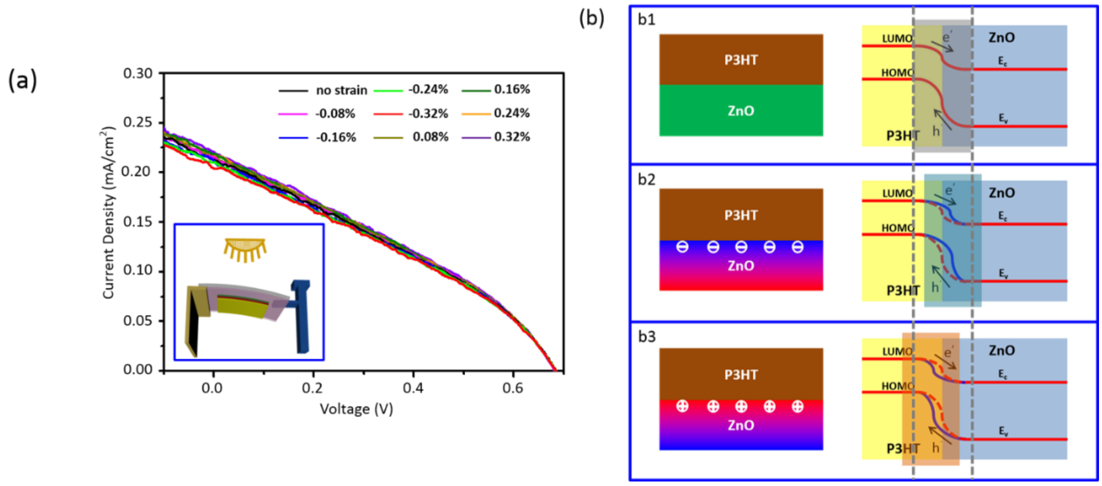

Figure 30: Group 1 solar cell performance under strains and the mechanism for piezo-phototronic effect. (a) *J–V* characteristics of Group 1 solar cell under strains at the illumination intensity of 25 mW/cm^2. The inset shows the method to apply strain to the solar cell. (b) Schematics explaining the mechanism how piezo-phototronic effect tunes the solar cell performance. Red line represents the band structure without strain. Blue line represents the tuned band structure with strain. Grey shade area represents the depletion region without strain. Blue and orange shade represent the depletion region when negative and positive polarization charges were induced at the interface respectively.

Although the piezophototronic effect demonstrated for Group 1 sample can indeed improve or degrade the solar cell performance, the amount of change is relatively small and we need to look for methods to further improve this effect. As is shown by many studies [106-109], the piezoelectricity in sputtered ZnO film arises from the c-axis self-aligning among grains and one way to increase its piezoelectric coefficient is to improve the crystallinity by thermal processing. Thus in Group 2 sample, the ZnO is deposited when the sample substrate is heated at 120 ℃ during the whole sputtering process while all other parameters are kept the same as for Group 1. X-ray Diffraction (XRD) technique is used to analyze the as-sputtered ZnO and determine the level of alignment. As indicated in Figure 31(a), both samples have a diffraction peak at $2\theta \approx 34°$, corresponding to the (0002) plane of Wurtzite ZnO (the plane that is responsible for the piezoelectric property). It is clearly shown that the Group 2 sample, represented by the red curve, has a higher level of alignment and thus a higher piezoelectric coefficient compared to Group 1 sample, represented by the blue curve. Group 2 solar cell is subsequently tested under different strain levels and the *J–V* characteristics are plotted in Figure 31 (b). Under zero strain, the J_{SC} is 0.217 mA/cm^2, the V_{OC} is 0.683 V and the efficiency is 0.18%. Inevitably, the electrical properties of Group 2 ZnO will be different from Group 1 due to slight difference in factors like grain size but in general, the thermal processing can be considered to have little influence on the performance of strain free solar cells. When strain is applied to the Group 2 device, we observe a much higher level of change on the solar cell performance. Specifically, J_{SC} is increased by 9.96% to 0.239 mA/cm^2 under 0.32% tensile strain and is decreased by 6.292% to 0.204 mA/cm^2 under 0.32% compressive strain. Accordingly, the efficiency is increased by 12.1% to 0.203% under 0.32% tensile strain and is decreased by 6.84% to 0.169% under 0.32% compressive strain (relevant data will be summarized in Figure 33). Thus, by comparing the measurement results from Group 1 and Group 2, it can be concluded that thermal processing, which improves the crystallinity and piezoelectric strength of ZnO film, is an effective method to enhance the piezo-phototronics effect without degrading the original performance of strain-free solar cells.

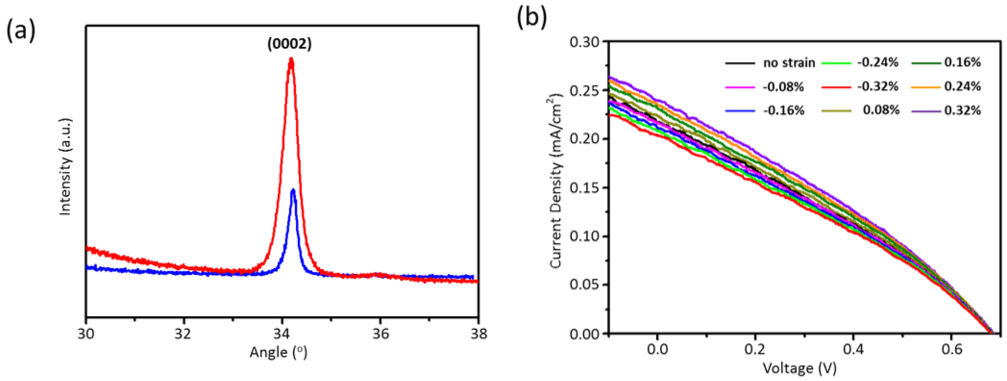

Figure 31: Effect of thermal processing on the strength of piezo-phototronic effect and the solar cell performance. (a) XRD spectrum for Group 1 sample, in blue, and Group 2 sample, in red. (b) *J–V* characteristics of Group 2 solar cell under strains at the illumination intensity of 25 mW/cm^2.

Different from conventional piezoelectric materials such as PZT, BaTiO3 which are insulators, free charge carriers in piezoelectric semiconductors can always partially screen the piezopotential, thus weakening the piezoelectric output. Therefore, in addition to improving crystallinity of ZnO, reducing the doping concentration will also improve piezophototronic effect. However, compared to crystallinity which has little impact on semiconducting properties if well controlled, adjustment of doping level almost certainly affects solar cell performance. It is sophisticated to tell whether the doping level change lowers the solar cell performance, and if it does, whether the loss could be compensated by the performance enhancement from piezo-phototronics effect. To answer the above question, several groups of samples will be studied below.

As many studies suggest [110-112], the doping level of ZnO is closely related to the atmosphere during sputtering and a lower partial pressure of oxygen will give rise to a higher level of oxygen vacancies and therefore a higher doping level. ZnO layer of the first sample under test in this section is sputtered with pure Ar at a flow rate of 40 sccm under 120 ℃ substrate heating, labeled as Group 3. The as-measured *J–V* characteristics are shown in Figure 32 (a). In strain free condition, the solar cell yields a J_{SC} of 0.1176 mA/cm^2, a V_{OC} of 0.374 V and an efficiency of 0.05%. When strain is applied, we see a similar trend of performance tuning. Specifically, J_{SC} is increased by 8.58% to 0.1277 mA/cm^2 under 0.32% tensile strain and is decreased by 9.50% to 0.1065 mA/cm^2 under 0.32% compressive strain. Accordingly, the efficiency is increased by 9.3% to 0.056% under 0.32% tensile strain and is decreased by 8.53% to 0.047% under 0.32% compressive strain. For comparison purpose, the *J–V* characteristics of Group 2 sample (30 sccm Ar, 10 sccm O_2, substrate heated at 120 ℃), which was discussed above, is also shown in Figure 32 (b). Then to further increase the oxygen partial pressure, ZnO of Group 4 is sputtered under 20 sccm of Ar and 20 sccm of O_2, heated at 120 ℃. Shown by the *J–V* characteristics in Figure 32 (c), at zero strain, the solar cell yields a J_{SC} of 0.2153 mA/cm^2, a V_{OC} of 0.683 V and an efficiency of 0.17%. When 0.32% tensile strain is applied, J_{SC} is increased by 19.97% to 0.258 mA/cm^2 and efficiency is increased by 17.1% to 0.2%. When 0.32% compressive strain is applied, J_{SC} is decreased by 11.2% to 0.191 mA/cm^2 and efficiency is decreased by 9.16% to 0.155%. ZnO layer of the last group is sputtered under 10 sccm of Ar and 30 sccm of O_2, heated at 120 ℃ and the solar cell *J–V* characteristics are shown in Figure 32 (d). At zero strain, the solar cell yields a J_{SC} of 0.2095 mA/cm^2, a V_{OC} of 0.61 V and an efficiency of 0.14%. When 0.32% tensile strain is applied, J_{SC} is increased by 15.45% to 0.24 mA/cm^2 and efficiency is increased by 17.46% to 0.167%. When 0.32% compressive strain is applied, J_{SC} is decreased by 12.52% to 0.1833 mA/cm^2 and efficiency is decreased by 12.11% to 0.1248%. From the above results, we can see that oxygen partial pressure during ZnO sputtering is positively related to the strength of the piezophototronic effect. However, its impact on solar cell performance is rather complex.

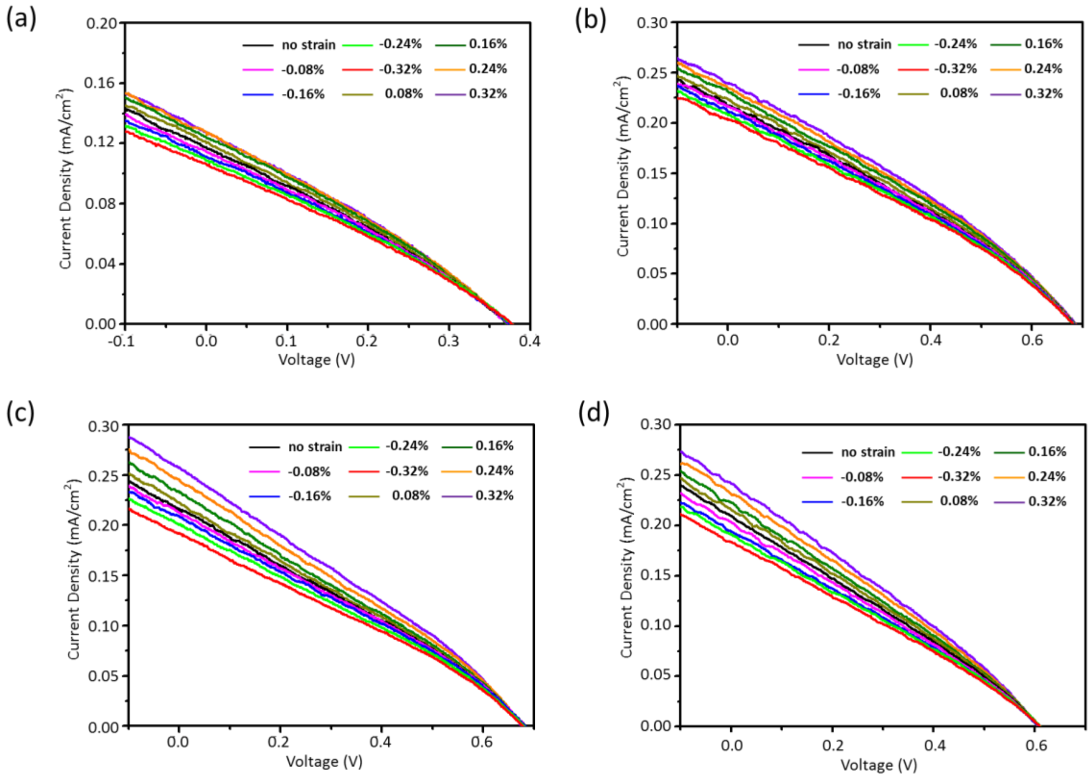

Figure 32: Effect of sputtering atmosphere on the strength of piezo-phototronic effect and the solar cell performance. (a) *J–V* characteristics of Group 3 solar cell under strains at the illumination intensity of 25 mW/cm^2. (b) *J–V* characteristics of Group 2 solar cell under strains at the illumination intensity of 25 mW/cm^2. (c) *J–V* characteristics of Group 4 solar cell under strains at the illumination intensity of 25 mW/cm^2. (d) *J–V* characteristics of Group 5 solar cell under strains at the illumination intensity of 25 mW/cm^2.

To fully analyze and better understand the above data, J_{SC}, V_{OC}, efficiency and fill factor of all five groups of samples under 9 different strain states are summarized in Figure 33 (a)–(d) respectively. At zero strain, Group 3 has the lowest J_{SC}, V_{OC} and efficiency of all. This indicates that when ZnO is deposited under pure Ar, the doping level may be excessively high and there is significant damage to the crystal, leading to a shorter diffusion length, a higher recombination rate and a lower collection probability [113]. Group 1, 2 and 4 in the zero strain case have almost the same J_{SC} and V_{OC}. However, Group 1 enjoys the highest fill factor while Group 4 suffers the lowest fill factor, making

Group 1 the most efficient solar cell under zero strain. The lowering of fill factor could be explained by the increase of series resistance [113] due to the heating of the sample and a higher oxygen partial pressure during the sputtering process. However, the level of series resistance has not yet affected the value of $\mathrm{J_{SC}}$ in these samples. ZnO of Group 5 is deposited under the highest oxygen partial pressure of 75%, leading to two effects. The first one is a further increase in series resistance which is possibly responsible for a lower J_{SC} compared to Group 1, 2 and 4. The second one is a decrease in shunt resistance that is reflected in its lower V_{OC}. This could be attributed to the phenomenon that when an excessively high oxygen partial pressure is in presence during ZnO sputtering, surface smoothness is drastically degraded[114, 115], which leads to more contact defects between ZnO and the spin-coated P3HT. When strain is gradually applied, J_{SC} and efficiency gradually increases under tensile strain and gradually decreases under compressive strain for all cases as a result of piezophototronic effect. On the other hand, the values of V_{OC} for all five groups stay relatively constant under different strains, reason of which has been explained above. Furthermore, the fill factor is also stable over different strains, meaning the straining process does not impact the series and shunt resistance to an observable extent. The highest J_{SC} is achieved by Group 3 under 0.32% tensile strain thanks to the strong piezo-phototronic effect for this sample. The highest efficiency, however, is achieved by Group 2 under 0.32% since it has a higher fill factor as discussed above. To have a more direct sense of the strength of piezophototronic effect, J_{SC} data in Figure 33 (a) and efficiency data in Figure 33 (c) are linearly fitted for each group. Slope values for the fitted curves in Figure33 (a) are

2.20, 5.63, 3.47, 9.61 and 8.84 in the unit of mA/cm^2/%strain for Group 1–5, respectively, and slope values for fitted curves in Figure 33(c) are 1.63, 5.24, 1.47, 6.48 and 6.32 in the unit of %eff/%strain for Group 1–5, respectively. These values are compiled in Figure 33 (e). As expected, under the same atmosphere, Group 2 has a larger slope for both J_{SC} and efficiency than Group 1 due to a better c-axis alignment. Under the same sputtering temperature the slopes of fitted curves increase with the increase of oxygen partial pressure but is saturated somewhere between 50% and 75% of oxygen partial pressure. It is worth noting that the crystallinity is not completely independent of the sputtering atmosphere and an excessively high oxygen partial pressure may lead to poorer grain alignment [114, 116], consistent with our data showing that the curve for Group 5 has slightly smaller slopes than that of Group 4. Consequently, without taking into account of the strain-free solar cell performance, the largest amount of performance improvement is achieved by the Group 4 sample.

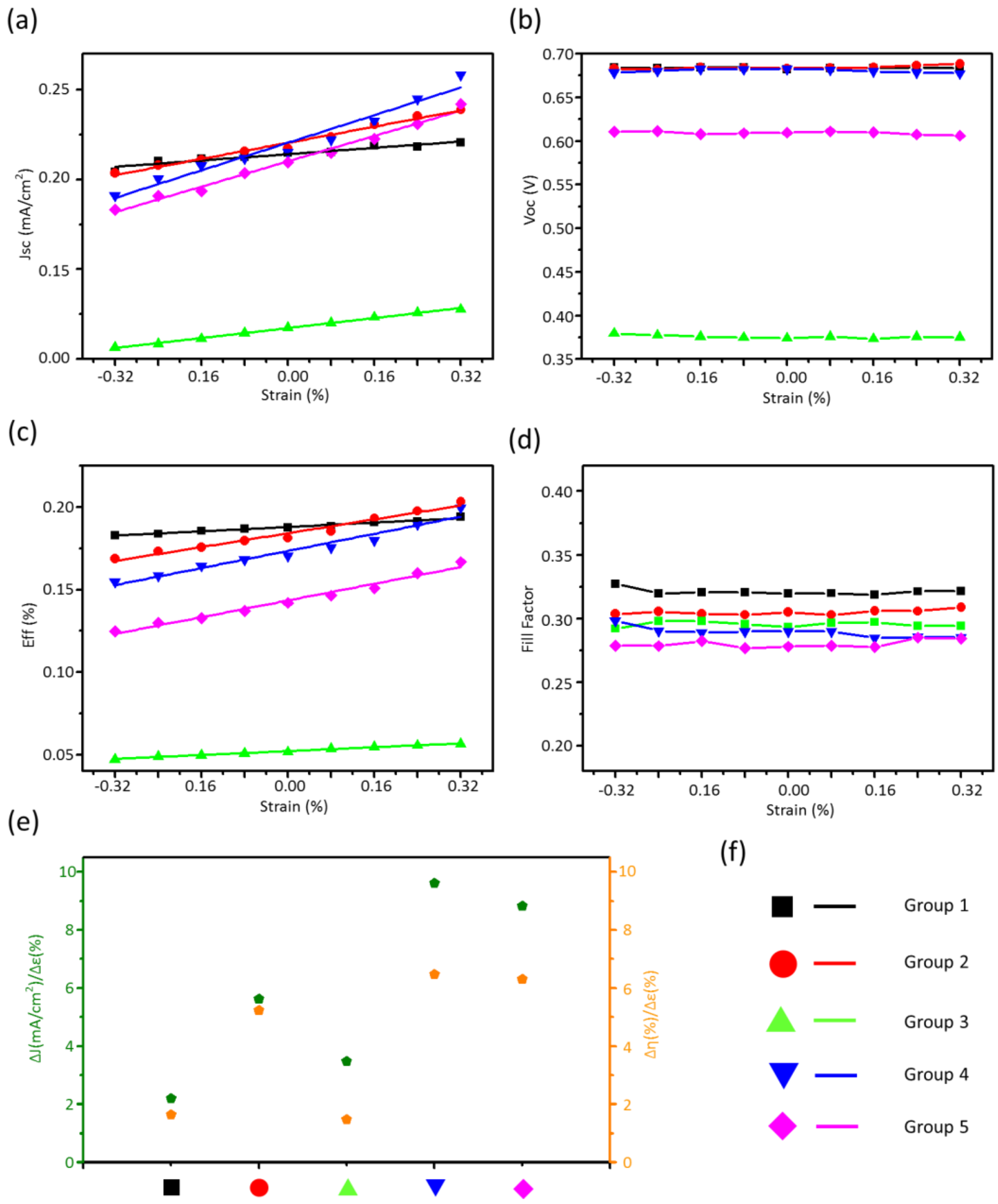

Figure 33: Summarization of important solar cell parameters for the five groups of samples. (a) Strain – *Jsc* scattergram. Linear fitting is performed for each group. (b) Strain – V_{OC} scattergram. (c) Strain – efficiency scattergram. Linear fitting is performed for each group. (d) Strain – fill factor scattergram. (e) Scattergram for the slopes of fitted curves in (a) and (c). ε represent strain and η represent efficiency in this figure. (f) Specific symbols and colors are assigned to represent each group.

In summary, the piezophototronic effect is demonstrated in the ZnO / P3HT solar cell system, and we have detailedly studied the influence of crystallization and doping level of ZnO on the strength of piezophototronic effect as well as the overall solar cell performance by testing and comparing five different groups of samples. Within our range of study, the highest efficiency is achieved by Group 2 solar cell (ZnO is sputtered at 120 W, 6 mTorr, 30 sccm Ar, 10 sccm O2 and substrate heated to 120 ℃) under 0.32% tensile strain. Further increasing the piezophototronic effect by using a higher oxygen partial pressure will lead to poorer strain-free solar cell performance which could not be effectively compensated by the current range of strain-induced enhancement. (However, more enhancement could be achieved by introducing a larger strain.) The general principles and regularities provided in this study are universal and applicable to all solar cell systems involving piezoelectric semiconductor materials and could provide meaningful guidance on further increasing performances of commercial solar cells based on CdTe, GaAs etc. and also spur the development of flexible solar cells for smart applications in various situations.

6. Conclusions

Innovation on human-machine interfacing technologies is becoming increasingly important for the realization of efficient, smart and multifunctional electronic/optoelectronic systems. The piezotronic effect which is based on piezoelectric semiconductors materials and utilizes the piezoelectric polarization field / charges to regulate electron/hole transport is a novel field of study for the interfacing between electronics / optoelectronics and mechanical stimulations. Initiated in the year of 2006, exciting progress on demonstrating this effect for various applications based on individual NWs have been reported. Due to the limitations of single NW device architectures, the focus of my five years' PhD research in Dr. Zhong Lin Wang's group has been on studying piezotronic effect and devices based on ordered NWs array and thin film materials for better fabrications capability and broader, more sophisticated applications. Three major aspects have been covered in my research:

1. Material synthesis: this part of the research is the basis for extending piezotronics from single NW devices to NWs array and thin film devices. Ammonium hydroxide as a precursor has been studied for the hydrothermal growth of ZnO NWs array which is shown to provide benefits such as strong seedless ZnO nucleation and one more freedom of engineering the growth process. ZnO thin films synthesized by RF sputtering have also been analyzed in detail and the suitability of this type of material for piezotronic applications has also been demonstrated.

2. Piezotronics beyond single NW devices: with the knowledge of how to appropriately

synthesize ZnO NWs array and ZnO thin films, piezotronic devices based on these materials have been successfully demonstrated. Integration of piezotronic strain sensing units in a highly ordered manner has led to the realization of ultra-high density tactile imaging devices, offering competitive advantages over traditional technologies based on piezoresistive and field-effect strain sensing. Simple structured thin film piezotronic devices in complete compatibility with existing industrial production capabilities have also been presented, showing the possibility of the commercialization of this young field in the near future.

3. Performance modulation of optoelectronic devices by the piezophototronic effect: this part of the research is also motivated by extending the demonstration of the piezophototronic effect on individual NW based devices toward that on NWs array and thin film based devices. Photodetectors made of [p-Si / n-ZnO NWs array] heterogeneous p-n junction and the ones made of [Au / n-ZnO thin film] Schottky junction have both been studied and the performance optimizations by the piezophototronic effect were demonstrated. Moreover, thin film solar cells constructed by p-P3HT and n-ZnO were also studied and optimized energy harvesting efficiency was achieved by modulating material properties.

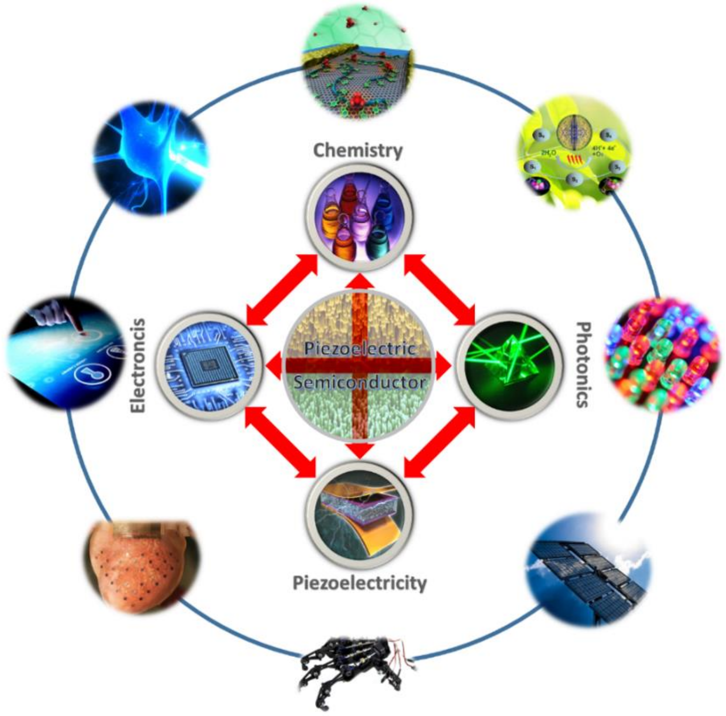

Figure 34: Schematics showing that with piezoelectric semiconductors as the material foundation, the field of piezoelectricity, electronics, photonics and chemistry can be actively linked together, which then can give rise to a large number of significant applications.

In summary, this dissertation presents systematic study of the synthesis of ZnO NWs array and thin films as well as the implementation of the piezotronic and piezophototronic effects based on these materials for scalable device/system fabrication and novel applications. The smart coupling of piezoelectricity and the electron/hole transport process gives rise to a brand new mechanism of mechanical interfacing with electrons, holes, photons and so on. The author's PhD research makes meaningful progress toward extending this field of research from single NW devices to NWs array and thin film devices. By going down this route, there is every reason to believe that the effect of piezotronics will eventually succeed as a revolutionary interfacing mechanism, as described in Figure 34, which contributes to the future generations of electronic, optoelectronic and other multifunctional systems.

References:

[1] D.H. Kim, Science, 333 (2011) 1703-1703.

[2] Y.G. Sun, J.A. Rogers, Adv Mater, 19 (2007) 1897-1916.

[3] J.H. Ahn, J.H. Je, J Phys D Appl Phys, 45 (2012).

[4] F. Carpi, D. De Rossi, Ieee T Inf Technol B, 9 (2005) 574-574.

[5] B.Z. Tian, J. Liu, T. Dvir, L.H. Jin, J.H. Tsui, Q. Qing, Z.G. Suo, R. Langer, D.S. Kohane, C.M. Lieber, Nat Mater, 11 (2012) 986-994.

[6] P.S. Waggoner, H.G. Craighead, Lab Chip, 7 (2007) 1238-1255.

[7] W.P. Eaton, J.H. Smith, Smart Mater Struct, 6 (1997) 530-539.

[8] A.A. Barlian, W.T. Park, J.R. Mallon, A.J. Rastegar, B.L. Pruitt, P Ieee, 97 (2009) 513-552.

[9] Z.L. Wang, J Phys-Condens Mat, 16 (2004) R829-R858.

[10] S.P. Beeby, M.J. Tudor, N.M. White, Meas Sci Technol, 17 (2006) R175-R195.

[11] A. Janshoff, H.J. Galla, C. Steinem, Angew Chem Int Edit, 39 (2000) 4004-4032.

[12] Z.L. Wang, Mat Sci Eng R, 64 (2009) 33-71.

[13] J. Zhou, Y.D. Gu, P. Fei, W.J. Mai, Y.F. Gao, R.S. Yang, G. Bao, Z.L. Wang, Nano Lett, 8 (2008) 3035-3040.

[14] Z.L. Wang, J Phys Chem Lett, 1 (2010) 1388-1393.

[15] X.D. Wang, J. Zhou, J.H. Song, J. Liu, N.S. Xu, Z.L. Wang, Nano Lett, 6 (2006) 2768-2772.

[16] J.H. He, C.L. Hsin, J. Liu, L.J. Chen, Z.L. Wang, Adv Mater, 19 (2007) 781-+.

[17] Z.L. Wang, Adv Mater, 19 (2007) 889-892.

[18] Y. Zhang, Y. Liu, Z.L. Wang, Adv Mater, 23 (2011) 3004-3013.

[19] Z.Y. Gao, J. Zhou, Y.D. Gu, P. Fei, Y. Hao, G. Bao, Z.L. Wang, J Appl Phys, 106 (2009).

[20] Y. Gao, Z.L. Wang, Nano Lett, 9 (2009) 1103-1110.

[21] Y. Liu, Q. Yang, Y. Zhang, Z.Y. Yang, Z.L. Wang, Adv Mater, 24 (2012) 1410-1417.

[22] Z.L. Wang, Adv Mater, 24 (2012) 4630-4631.

[23] C.R. Crowell, S.M. Sze, Solid State Electron, 9 (1966) 1035-&.

[24] J. Shi, M.B. Starr, X.D. Wang, Adv Mater, 24 (2012) 4683-4691.

[25] J. Shi, M.B. Starr, H. Xiang, Y. Hara, M.A. Anderson, J.H. Seo, Z.Q. Ma, X.D. Wang, Nano Lett, 11 (2011) 5587-5593.

[26] R.S. Muller, T.I. Kamins, M. Chan, Device electronics for integrated circuits, 3rd ed., John Wiley & Sons, New York, NY, 2003.

[27] Y. Zhang, Z.L. Wang, Adv Mater, 24 (2012) 4712-4718.

[28] M.H. Huang, S. Mao, H. Feick, H.Q. Yan, Y.Y. Wu, H. Kind, E. Weber, R. Russo, P.D. Yang, Science, 292 (2001) 1897-1899.

[29] X.D. Wang, J.H. Song, P. Li, J.H. Ryou, R.D. Dupuis, C.J. Summers, Z.L. Wang, J Am Chem Soc, 127 (2005) 7920-7923.

[30] J.H. Song, X.D. Wang, E. Riedo, Z.L. Wang, J Phys Chem B, 109 (2005) 9869-9872.

[31] Y. Liu, C.R. Gorla, S. Liang, N. Emanetoglu, Y. Lu, H. Shen, M. Wraback, J Electron Mater, 29 (2000) 69-74.

[32] M. Willander, O. Nur, Q.X. Zhao, L.L. Yang, M. Lorenz, B.Q. Cao, J.Z. Perez, C. Czekalla, G. Zimmermann, M. Grundmann, A. Bakin, A. Behrends, M. Al-Suleiman, A. El-Shaer, A.C. Mofor, B. Postels, A. Waag, N. Boukos, A. Travlos, H.S. Kwack, J. Guinard, D.L. Dang, Nanotechnology, 20 (2009).

[33] E.M. Wong, P.C. Searson, Appl Phys Lett, 74 (1999) 2939-2941.

[34] C.S. Rout, S.H. Krishna, S.R.C. Vivekchand, A. Govindaraj, C.N.R. Rao, Chem Phys Lett, 418 (2006) 586-590.

[35] X.W. Sun, H.S. Kwok, J Appl Phys, 86 (1999) 408-411.

[36] H.S. Kang, J.S. Kang, J.W. Kim, S.Y. Lee, J Appl Phys, 95 (2004) 1246-1250.

[37] P.F. Carcia, R.S. McLean, M.H. Reilly, G. Nunes, Appl Phys Lett, 82 (2003) 1117-1119.

[38] E.M.C. Fortunato, P.M.C. Barquinha, A.C.M.B.G. Pimentel, A.M.F. Goncalves, A.J.S. Marques, L.M.N. Pereira, R.F.P. Martins, Adv Mater, 17 (2005) 590-+.

[39] B.B. Lakshmi, C.J. Patrissi, C.R. Martin, Chem Mater, 9 (1997) 2544-2550.

[40] M.N. Kamalasanan, S. Chandra, Thin Solid Films, 288 (1996) 112-115.

[41] X.N. Wen, W.Z. Wu, Y. Ding, Z.L. Wang, J Mater Chem, 22 (2012) 9469-9476.

[42] J.X. Wang, X.W. Sun, Y. Yang, H. Huang, Y.C. Lee, O.K. Tan, L. Vayssieres, Nanotechnology, 17 (2006) 4995-4998.

[43] B. Sun, H. Sirringhaus, Nano Lett, 5 (2005) 2408-2413.

[44] S. Xu, Y. Wei, M. Kirkham, J. Liu, W. Mai, D. Davidovic, R.L. Snyder, Z.L. Wang, J Am Chem Soc, 130 (2008) 14958-+.

[45] R.S.W.a.W.C. Ellis, TRANSACTIONS OF THE METALLURGICAL SOCIETY OF AIME, 233 (1965) 1053-1064.

[46] R. Guo, J. Nishimura, M. Matsumoto, M. Higashihata, D. Nakamura, T. Okada, Jpn J Appl Phys, 47 (2008) 741-745.

[47] X.D. Wang, C.J. Summers, Z.L. Wang, Nano Lett, 4 (2004) 423-426.

[48] J.H. Zeng, Y.L. Yu, Y.F. Wang, T.J. Lou, Acta Mater, 57 (2009) 1813-1820.

[49] S. Xu, Z.L. Wang, Nano Res, 4 (2011) 1013-1098.

[50] Y.G. Wei, W.Z. Wu, R. Guo, D.J. Yuan, S.M. Das, Z.L. Wang, Nano Lett, 10 (2010) 3414-3419.

[51] Q.C. Li, V. Kumar, Y. Li, H.T. Zhang, T.J. Marks, R.P.H. Chang, Chem Mater, 17 (2005) 1001-1006.

[52] K. Govender, D.S. Boyle, P.B. Kenway, P. O'Brien, J Mater Chem, 14 (2004) 2575-2591.

[53] A. Sugunan, H.C. Warad, M. Boman, J. Dutta, J Sol-Gel Sci Techn, 39 (2006) 49-56.

[54] S. Xu, C. Lao, B. Weintraub, Z.L. Wang, J Mater Res, 23 (2008) 2072-2077.

[55] G.W. Smith, H.W. Jacobson, J Phys Chem-Us, 60 (1956) 1008-1012.

[56] Z. Wang, X.F. Qian, J. Yin, Z.K. Zhu, Langmuir, 20 (2004) 3441-3448.

[57] M.M. Santore, N. Kozlova, Langmuir, 23 (2007) 4782-4791.

[58] C.K. Xu, P. Shin, L.L. Cao, D. Gao, J Phys Chem C, 114 (2010) 125-129.

[59] J. McMurran, J. Kouvetakis, D.J. Smith, Appl Phys Lett, 74 (1999) 883-885.

[60] S. Ilican, Y. Caglar, M. Caglar, J Optoelectron Adv M, 10 (2008) 2578-2583.

[61] K. Tominaga, N. Umezu, I. Mori, T. Ushiro, T. Moriga, I. Nakabayashi, Thin Solid Films, 334 (1998) 35-39.

[62] Y.F. Chen, D.M. Bagnall, Z.Q. Zhu, T. Sekiuchi, K.T. Park, K. Hiraga, T. Yao, S. Koyama, M.Y. Shen, T. Goto, J Cryst Growth, 181 (1997) 165-169.

[63] N.W. Emanetoglu, C. Gorla, Y. Liu, S. Liang, Y. Lu, Mat Sci Semicon Proc, 2 (1999) 247-252.

[64] Y.F. Hu, L. Lin, Y. Zhang, Z.L. Wang, Adv Mater, 24 (2012) 110-+.

[65] C. Kim, S. Kim, C. Lee, Japanese Journal of Applied Physics Part 1-Regular Papers Brief

Communications & Review Papers, 44 (2005) 8501-8503.

[66] C. Lee, C. Kim, S. Kim, Y. Park, High-Performance Ceramics IV, Pts 1-3, 336-338 (2007) 581-584.

[67] J. Zhou, P. Fei, Y.D. Gu, W.J. Mai, Y.F. Gao, R. Yang, G. Bao, Z.L. Wang, Nano Lett, 8 (2008) 3973-3977.

[68] W.Z. Wu, Y.G. Wei, Z.L. Wang, Adv Mater, 22 (2010) 4711-+.

[69] W.Z. Wu, Z.L. Wang, Nano Lett, 11 (2011) 2779-2785.

[70] Y.S. Zhou, R. Hinchet, Y. Yang, G. Ardila, R. Songmuang, F. Zhang, Y. Zhang, W.H. Han, K. Pradel, L. Montes, M. Mouis, Z.L. Wang, Adv Mater, 25 (2013) 883-888.

[71] R.M. Yu, W.Z. Wu, Y. Ding, Z.L. Wang, Acs Nano, 7 (2013) 6403-6409.

[72] W.Z. Wu, X.N. Wen, Z.L. Wang, Science, 340 (2013) 952-957.

[73] K. Takei, T. Takahashi, J.C. Ho, H. Ko, A.G. Gillies, P.W. Leu, R.S. Fearing, A. Javey, Nat Mater, 9 (2010) 821-826.

[74] S.C.B. Mannsfeld, B.C.K. Tee, R.M. Stoltenberg, C.V.H.H. Chen, S. Barman, B.V.O. Muir, A.N. Sokolov, C. Reese, Z.N. Bao, Nat Mater, 9 (2010) 859-864.

[75] T. Someya, T. Sekitani, S. Iba, Y. Kato, H. Kawaguchi, T. Sakurai, P Natl Acad Sci USA, 101 (2004) 9966-9970.

[76] D.J. Lipomi, M. Vosgueritchian, B.C.K. Tee, S.L. Hellstrom, J.A. Lee, C.H. Fox, Z.N. Bao, Nat Nanotechnol, 6 (2011) 788-792.

[77] T. Sekitani, T. Yokota, U. Zschieschang, H. Klauk, S. Bauer, K. Takeuchi, M. Takamiya, T. Sakurai, T. Someya, Science, 326 (2009) 1516-1519.

[78] D.H. Kim, J.H. Ahn, W.M. Choi, H.S. Kim, T.H. Kim, J.Z. Song, Y.G.Y. Huang, Z.J. Liu, C. Lu, J.A. Rogers, Science, 320 (2008) 507-511.

[79] A. Javey, S. Nam, R.S. Friedman, H. Yan, C.M. Lieber, Nano Lett, 7 (2007) 773-777.

[80] J.H. Ahn, H.S. Kim, K.J. Lee, S. Jeon, S.J. Kang, Y.G. Sun, R.G. Nuzzo, J.A. Rogers, Science, 314 (2006) 1754-1757.

[81] S. Nam, X.C. Jiang, Q.H. Xiong, D. Ham, C.M. Lieber, P Natl Acad Sci USA, 106 (2009) 21035-21038.

[82] T. Bryllert, L.E. Wernersson, L.E. Froberg, L. Samuelson, Ieee Electr Device L, 27 (2006) 323-325.

[83] R.S. Johansson, A.B. Vallbo, J Physiol-London, 286 (1979) 283-300.

[84] B. Nemeth, M.D. Symes, A.G. Boulay, C. Busche, G.J.T. Cooper, D.R.S. Cumming, L. Cronin, Adv Mater, 24 (2012) 1238-1242.

[85] S.A. Mascaro, H.H. Asada, Ieee T Robotic Autom, 17 (2001) 698-708.

[86] X.N. Wen, W.Z. Wu, Y. Ding, Z.L. Wang, Adv Mater, 25 (2013) 3371-3379.

[87] R.S. Muller, T.I. Kamins, M. Chan, Device electronics for integrated circuits, Third ed., John Wiley & Sons Inc, New York, NY, 2002.

[88] J. Singh, Semiconductor optoelectronics : physics and technology, McGraw-Hill International. ed., McGraw-Hill, New York, 1995.

[89] S.S. Lin, J.L. Huang, Surf Coat Tech, 185 (2004) 222-227.

[90] E. Mirica, G. Kowach, P. Evans, H. Du, Cryst Growth Des, 4 (2004) 147-156.

[91] R.W. Soutas-Little, Dover Publications2012, pp. 1 online resource ().

[92] Q. Yang, X. Guo, W.H. Wang, Y. Zhang, S. Xu, D.H. Lien, Z.L. Wang, Acs Nano, 4 (2010) 6285-6291.

[93] Q. Yang, W.H. Wang, S. Xu, Z.L. Wang, Nano Lett, 11 (2011) 4012-4017.

[94] L. Dong, S.M. Niu, C.F. Pan, R.M. Yu, Y. Zhang, Z.L. Wang, Adv Mater, 24 (2012) 5470-5475.

[95] C.F. Pan, S.M. Niu, Y. Ding, L. Dong, R.M. Yu, Y. Liu, G. Zhu, Z.L. Wang, Nano Lett, 12 (2012) 3302-3307.

[96] F. Zhang, Y. Ding, Y. Zhang, X.L. Zhang, Z.L. Wang, Acs Nano, 6 (2012) 9229-9236.

[97] C. Soci, A. Zhang, B. Xiang, S.A. Dayeh, D.P.R. Aplin, J. Park, X.Y. Bao, Y.H. Lo, D. Wang, Nano Lett, 7 (2007) 1003-1009.

[98] K. Keem, H. Kim, G.T. Kim, J.S. Lee, B. Min, K. Cho, M.Y. Sung, S. Kim, Appl Phys Lett, 84 (2004) 4376-4378.

[99] Z.N. Wang, R.M. Yu, X.N. Wen, Y. Liu, C.F. Pan, W.Z. Wu, Z.L. Wang, Acs Nano, 8 (2014) 12866-12873.

[100] Y. Liu, S.M. Niu, Q. Yang, B.D.B. Klein, Y.S. Zhou, Z.L. Wang, Adv Mater, 26 (2014) 7209-7216.

[101] S.M. Sze, Physics of semiconductor devices, 2. ed., John Wiley, New York, 1981.

[102] M. Dutta, D. Basak, Appl Phys Lett, 92 (2008).

[103] S.O. Kasap, R.K. Sinha, Optoelectronics and photonics : principles and practices, 2nd ed., Pearson Education, Harlow, Essex, 2013.

[104] P.N. Ni, C.X. Shan, S.P. Wang, X.Y. Liu, D.Z. Shen, J Mater Chem C, 1 (2013) 4445-4449.

[105] X.N. Wen, W.Z. Wu, Z.L. Wang, Nano Energy, 2 (2013) 1093-1100.

[106] N. Fujimura, T. Nishihara, S. Goto, J.F. Xu, T. Ito, J Cryst Growth, 130 (1993) 269-279.

[107] G.J. Exarhos, S.K. Sharma, Thin Solid Films, 270 (1995) 27-32.

[108] M.K. Puchert, P.Y. Timbrell, R.N. Lamb, J Vac Sci Technol A, 14 (1996) 2220-2230.

[109] D. Raoufi, T. Raoufi, Appl Surf Sci, 255 (2009) 5812-5817.

[110] S. Kim, W.I. Lee, E.H. Lee, S.K. Hwang, C. Lee, J Mater Sci, 42 (2007) 4845-4849.

[111] K. Ellmer, J Phys D Appl Phys, 33 (2000) R17-R32.

[112] T. Tsuji, M. Hirohashi, Appl Surf Sci, 157 (2000) 47-51.

[113] J. Nelson, The physics of solar cells, Imperial College Press, London, 2003.

[114] Y.E. Lee, J.B. Lee, Y.J. Kim, H.K. Yang, J.C. Park, H.J. Kim, J Vac Sci Technol A, 14 (1996) 1943-1948.

[115] J.J. Chen, Y. Gao, F. Zeng, D.M. Li, F. Pan, Appl Surf Sci, 223 (2004) 318-329.

[116] R.J. Hong, H.J. Qi, J.B. Huang, G.B. He, Z.X. Fan, J.A. Shao, Thin Solid Films, 473 (2005) 58-62.